Title

Epitaxial Oxide Spintronics: a Road-map to Multiferroic Magnonic Memory

Author

Harris, Isaac Appel

Publication Date

2024

Peer reviewed|Thesis/dissertation

Epitaxial Oxide Spintronics: a Road-map to Multiferroic Magnonic Memory

By

Isaac Appel Harris

A dissertation submitted in partial satisfaction of the

requirements for the degree of

Doctor of Philosophy

in

Physics

in the

Graduate Division

of the

University of California, Berkeley

Committee in charge:

Professor Ramamoorthy Ramesh, Chair
Professor Lane Martin
Professor Zi Qiu

Summer 2024

Abstract

Epitaxial Oxide Spintronics: a Road-map to Multiferroic Magnonic Memory

by

Isaac Appel Harris

Doctor of Philosophy in Physics

University of California, Berkeley

Professor Ramamoorthy Ramesh, Chair

The wider application of spintronic devices requires the development of several new material platforms that can address the following challenges: 1) efficient conversion between spin and charge currents, 2) storage of magnetic information that can be easily manipulated, and 3) transmission of spin information that can be easily detected. With respect to the first challenge, Bismuthate-based superconductors are systems that are generally thought to offer weak spin-orbit coupling, despite the heavy elements that make up such compounds. Here we use spin-torque ferromagnetic resonance to measure a large spin-orbit torque efficiency driven by spin polarization generated in heterostructures based on $BaPb_{1-x}Bi_xO_3$ in a non-superconducting state. We suggest that the unexpectedly large current-induced torques could stem from an orbital Rashba effect associated with local inversion symmetry breaking in $BaPb_{1-x}Bi_xO_3$.

In response to the second challenge, Bismuth Ferrite has garnered considerable attention as a promising candidate for magnetoelectric spin-orbit coupled logic-in memory. While this model system offers a magnetic texture controllable by electric fields, epitaxial $BiFeO_3$ films have typically been deposited at temperatures higher than allowed for direction integration with silicon-CMOS platforms. Here, we solve this engineering problem by growing La-doped $BiFeO_3$ at temperatures reasonably compatible with silicon-CMOS integration on $BaPb_{1-x}Bi_xO_3$ electrodes. Despite the large lattice mismatch between the two materials, all layers are well-ordered with a [001] texture, and the La-doped $BiFeO_3$ exhibits desirable ferroelectric properties. These results provide a possible route for realizing epitaxial multiferroics on complex-oxide buffer layers at low temperatures and opens the door for potential silicon-CMOS integration. Furthermore, the incorporation of a material with efficient conversion between spin and charge with a multiferroic will drive innovation and application of new spintronic devices, such as all-oxide multiferroic magnonic memory architectures.

In response to the second and third challenges, spin waves in magnetic materials, or magnons, are promising information carriers due to their ultra-low energy dissipation and long coherence length. Antiferromagnets are strong candidate materials for magnetic information storage due in part to their stability to external fields and larger group velocities. Multiferroic antiferromagnets such as $BiFeO_3$ have an additional degree of freedom stemming from

magnetoelectric coupling, allowing for control of the magnetic structure, and thus magnons, with an electric field. Unfortunately, spin-wave propagation in $BiFeO_3$ is not well-understood due to the complexity of the magnetic structure. In this work, we discover an anisotropy in spin transport within the spin cycloid magnetic structure of $BiFeO_3$. We also show that through Lanthanum substitution, a single ferroelectric domain can be engineered with a stable, single-variant spin cycloid controllable by electric field. The strong anisotropy discussed is an important development in the understanding of magnon-spin currents in the spin cycloid magnetic texture.

Finally, understanding the anisotropies and other characteristics of magnon-spin currents in a multiferroic requires an understanding of the symmetries inherent to the magnetic and polar orders of the multiferroic. In this work, we present a phenomenological model to elucidate the existence of magnon spin currents in generalized multiferroics. This model takes inspiration from the symmetries of multiferroics such as $BiFeO_3$, and is grounded in experimental data obtained from $BiFeO_3$ and its derivatives. By introducing this model, we address the issue of symmetry-allowed, switchable magnon spin transport in multiferroics, thereby establishing a critical framework for comprehending magnon transport within complex magnetic textures.

Our responses to the three challenges posed above all point to a magnon-based multiferroic memory founded in epitaxial oxide heterostructures. In researching a path towards this application, we make new discoveries of the physics of spin-charge interconversion, heterostructure growth, and magnon dynamics in complicated magnetic textures. We hope that the following research will prove applicable not only towards the specific goal of multiferroic magnonic memory, but also to the wider field of epitaxial oxide spintronics.

Contents

Acknowledgements

First and foremost I would like to thank and acknowledge my parents, Deborah Harris and Robert Harris, for their love, support, and scientific advice throughout my degree and life. I also thank my grandparents Jefferey and Marjorie Appel, and my sister Sonia Harris for their love and support. I would also like to thank Sajant Anand for his friendship as a roommate throughout my degree, as well as my friends in the Berkeley Physics cohort and surrounding Berkeley communities for their friendship and support during this time.

I give thanks to Sajid Husain for his scientific partnership throughout the latter half of my degree. I thank all the lab members of the Lane Martin and Ramamoorthy Ramesh groups during my time at Berkeley for their help and mentorship. Finally, I thank my advisor Ramamoorthy Ramesh for his undying passion for scientific research, and for the opportunity to conduct this research in his lab and earn my degree.

Here I will take a moment to explicitly acknowledge the help from my coauthors from across the country and around the world in executing this research as well as in preparing these results for publication in journals. Chapter 3 includes results previously published in *Nature Electronics* under the title "Large spin-orbit torque in bismuthate-based heterostructures" with coauthors Anthony L. Edgeton, Neil G. Campbell, Yahong Chai, Marcel M. Mazur, Gautam Gurung, Xiaoxi Huang, Sandhya Susarla, Evgeny Y. Tsymbal, Daniel C. Ralph, Tianxiang Nan, Mark S. Rzchowski, Ramamoorthy Ramesh, and Chang-Beom Eom. Chapter 4 includes results previously published in *Nature Communications* under the title "Low-temperature grapho-epitaxial La-substituted $BiFeO_3$ on metallic perovskite," with coauthors Sajid Husain, Guanhui Gao, Xinyan Li, Peter Meisenheimer, Chuqiao Shi, Pravin Kavle, Chi Hun Choi, Tae Yeon Kim, Deokyoung Kang, Piush Behera, Didier Perrodin, Hua Guo, James M. Tour, Yimo Han, Lane W. Martin, Zhi Yao, and Ramamoorthy Ramesh. Chapter 5 includes results previously published in *Advanced Materials* under the title "Designed spin-texture-lattice to control anisotropic magnon transport in antiferromagnets" with coauthors Peter Meisenheimer, Maya Ramesh, Sajid Husain, Hyeon Woo Park, Shiyu Zhou, Hossein Taghinejad, Hongrui Zhang, Lane W. Martin, James Analytis, Paul Stevenson, Jorge Íñiguez-González, Se Kwon Kim, Darrell G. Schlom, Lucas Caretta, Zhi Yao, and Ramamoorthy Ramesh. Chapter 6 includes results previously published in *Nature Communications* under the title "Non-volatile magnon transport in a single domain multiferroic" with coauthors Sajid Husain, Peter Meisenheimer, Sukriti Mantri, Xinyan Li, Maya Ramesh, Piush Behera, Hossein Taghinejad, Jaegyu Kim, Pravin Kavle, Shiyu Zhou, Tae Yeon Kim, Hongrui Zhang, Paul Stephenson, James G. Analytis, Darrell Schlom, Sayeef Salahuddin, Jorge Íñiguez-González, Bin Xu, Lane W. Martin, Lucas Caretta, Yimo Han, Laurent Bellaiche, Zhi Yao, and Ramamoorthy Ramesh. And finally, Chapter 7 includes results previously submitted to *Physical Review Letters* under the title "Symmetry-based phenomenological model for magnon transport in a multiferroic" with coauthors Sajid Husain, Peter Meisenheimer, Maya Ramesh, Hyeon Woo Park, Lucas Caretta, Darrell Schlom, Zhi Yao, Lane W. Martin, Jorge Íñiguez-González, Se Kwon Kim, and Ramamoorthy Ramesh.

Part I
Introduction

The title of this document, *Epitaxial Oxide Spintronics: a Road-map to Multiferroic Magnonic Memory*, encapsulates the fundamental research objectives of my time at the University of California, Berkeley. The primary materials studied were all epitaxial oxide crystals, grown using pulsed laser deposition. The first material, $BaPb_{1-x}Bi_xO_3$, was measured for spin-to-charge conversion, and for its potential within the field of spintronics. The second material, $BiFeO_3$ (and it's Lanthanum-doped cousin $Bi_{1-x}La_xFeO_3$), is a multiferroic that was studied for its ability to host magnons, and transfer information via spin. The multiferroic nature of $BiFeO_3$ enables electric field control of magnons, a relatively new topic in the field of spintronics, and this control, paired with spin-to-charge conversion and careful symmetry considerations, paves the way for magnon-based memory applications. The compatibility of these two materials, each with its own special power, was confirmed at a deposition temperature compatible with current CMOS technologies. Hence within this dissertation, several important milestones on the road to multiferroic magnonic memory are achieved, using new physics enabled by epitaxial oxide materials.

I will start with background for the field of spintronics, and discuss some of its fundamental principles and motivations. Then, I will talk about the advantages of using epitaxial oxide heterostructures, particularly those grown by pulsed laser deposition. After these introductions, I will talk about the progress we have made in these areas. First, we measured the spin Hall effect in $BaPb_{1-x}Bi_xO_3$ to be $\theta_{SH} = 1.7$, which is very high compared to typical values for heavy metals. Second, we demonstrated low-temperature epitaxial growth of $BaPb_{1-x}Bi_xO_3/Bi_{1-y}La_yFeO_3/BaPb_{1-x}Bi_xO_3$ tri-layers at 450°C, which is the limit for integration into CMOS devices. Third, we developed a setup for electric-field controlled magnon transport experiments which allowed us to measure the anisotropy of magnon transport through the spin-cycloid of $BiFeO_3$, as well as electric-field controlled magnon transport in a single ferroelectric domain in La-doped $BiFeO_3$. Finally, we created a phenomenological model of electric-field controlled magnon transport in multiferroics, the first symmetry-based phenomenological model that enables predictions of some of the attributes of electric-field controlled magnon signals. I will conclude with a discussion that consolidates these achievements and enlists what further work will be necessary to enable multiferroic magnonic memory using epitaxial oxide spintronics.

1 Spintronics

In spintronics, devices use the electron spin as well as the electron charge to transmit or store information. A spin current, or the flow of angular momentum, becomes a major component of spintronic device schematics. There are several ways to generate a spin current, and a spin current can take different forms. Two ways to generate a spin current include 1) the spin-Hall effect (SHE), where electrons undergo spin-dependent scattering in a spin-orbit coupled metal or semiconductor [1], and 2) the spin-Seebeck effect (SSE), where a temperature gradient across a magnetic insulator drives a magnon spin current [2]. The spin currents that arise as a result of the SHE and SSE have different excitations as spin carriers. In the spin-Hall effect, the resulting spin current is characterized by an excess of electrons with up spin (without loss of generality) flowing in one direction, accompanied by an excess of electrons with down spin flowing in the opposite direction. This generates a net transfer of spin-angular momentum with electrons as the carriers, but no net charge current. In the SSE, magnons - excitations of the magnetic texture - carry the spin current through an insulator, and there is also no charge current. I will further discuss magnon currents in a later section.

One difficulty inherent to spintronics is spin-current detection. Whereas a charge current can be easily detected by measuring a voltage across a resistor, there is no simple analogy for spin currents. Two ways to measure a spin current include 1) using a spin-current to exert a torque on a magnetic moment, and 2) using the inverse spin-Hall effect (ISHE) to turn a spin current into a charge current, and then measuring a voltage. The mechanism for the ISHE is the same as that for the SHE: where the SHE directly converts charge to spin, the ISHE converts spin to charge. The former mechanism, the exertion of a torque on a magnetization by a spin current, is captured by the Slonczewski additions to the Landau-Lifschitz-Gilbert (LLG) equation to form the Landau-Lifschitz-Gilbert-Slonczewski (LLGS) equation, given below:

$$\dot{\mathbf{m}} = -\gamma \mathbf{m} \times \mathbf{H}_{\text{eff}} + \alpha \mathbf{m} \times \dot{\mathbf{m}} + \boldsymbol{\tau}_{\text{FL}} + \boldsymbol{\tau}_{\text{DL}}. \tag{1.1}$$

As usual in the LLG equation, γ it the gyromagnetic ratio, α is the Gilbert damping, and $\mathbf{H}_{\text{eff}}$ is the effective field. Here $\boldsymbol{\tau}_{\text{FL}}$ is the field-like torque exerted on the magnetization $\mathbf{m}$ and $\boldsymbol{\tau}_{\text{DL}}$ is the damping-like, or anti-damping-like torque exerted on the magnetization. These torques can bring about small changes to the magnetization that can be detected via a magnetoresistance signal, and an example of this signal is discussed further in the context of spin-torque ferromagnetic resonance.

In-processor Magnetic Memory

While small torques from spin-currents on the magnetization of some ferromagnet are useful for measuring the strength of the spin-Hall effect in metals adjacent to that ferromagnet, large torques from spin-currents can go so far as to switch the magnetization of a ferromagnet from one state into another. This enables an in-processor magnetic memory architecture known as magnetic random access memory (MRAM), which uses the state of a nanomagnetic bit to encode binary information. MRAM, in contrast to state-of-the-art CMOS-based processor memory such as SRAM and DRAM, is nonvolatile, which would allow for long-term in-

processor memory. In theory, this application could replace the current hard drive technology, and would reduce the energy losses in transferring information from the processor to the long term storage. To date, some companies have produced commercialized MRAM chips, and others are invested in MRAM research [3].

Spin-orbit torque (SOT) MRAM and related device architectures rely on the use of a metal with a spin-Hall effect to switch a nanomagnetic bit. One of the major challenges in SOT MRAM is that there are very few materials with strong enough spin-Hall effects to efficiently switch nanomagnets. In these materials, especially in heavy metals such as Tungsten, Tantalum, and Platinum which are often used, high current densities are required to switch nanomagnetic bits. This leads to Joule heating, which is damaging to devices, as well as high energy consumption, which makes SOT MRAM less marketable. In order to make SOT MRAM realistically competitive with state-of-the-art semiconductor technologies, materials with stronger charge-to-spin conversion must be found. While this could be achieved with topological insulators and strong spin-Hall effects [4], other effects such as the orbital Hall effect might allow for materials with strong charge to spin conversion [5–7]. In Chapter 3, we present a material with a giant charge-to-spin conversion efficiency, which may be due to more exotic Hall effects such as the orbital Hall effect.

Another method of switching the nanomagnetic bit in a memory device is to use a magnetoelectric material, where an electric field can control the magnetic order of the material. One such material combination is $BiFeO_3$, a multiferroic, exchange-coupled to an adjacent magnet such as CoFe. It has been shown that the application of an electric field can switch the magnetization of CoFe nanomagnets in such a device[8], and device architectures combining this with spin-to-charge conversion have been proposed for simultaneous logic and memory [9]. Realizing such devices would require $BiFeO_3$ - as well as a material with high spin-to-charge conversion - to be compatible with CMOS fabrication processes. In Chapter 4, we demonstrate such a material combination that can be deposited at 450°C, a temperature that is compatible with CMOS-integration.

Magnons

While electrons can carry a spin current in a conductor, magnons can transfer spin in an insulator. A magnon is the quantization of a spin-wave excitation in a magnetic material, and can carry information in a magnon current. One way to generate a magnon spin current is to use a spin current in a conductor, for example, from the spin-Hall effect, to inject spins across an interface from the conductor to a magnetic insulator[10]. Injected spins exert a torque on the magnetization of the insulator, and the resulting precession of magnetic dipoles creates magnons with spin aligned with the polarity of the spin current. These magnons can then diffuse across the insulator, creating a spin current. Another way to generate a magnon spin current is to use a thermal gradient and the spin-Seebeck effect[11]. In the spin-Seebeck effect, magnons diffuse along the direction of the temperature gradient, and if the population or diffusion dynamics of magnons is asymmetric in spin, then a spin current will accompany the diffusion. Just as a magnon current can be created by an accumulation of spin at an interface, an accumulation of magnons at an interface can create an electron-mediated spin current via the absorption of magnons[10]. Finally, if the magnon current is absorbed into a conductor with spin-to-charge conversion, the electronic spin current will be converted into

a charge current which can be measured.

With the above mechanisms, magnons can be used in spintronic devices to read magnetic states and transfer information. One advantage of using magnons as spin-current carriers instead of electrons is that magnons do not have Ohmic losses. Magnons in ferrimagnetic insulators such as Yttrium-iron garnet have been extensively studied[10], and have been shown to carry spin-information over long distances. Furthermore, magnons in colinear and canted antiferromagnets have also been studied[12, 13]. Magnons in more complicated spin textures, however, such as the spin cycloid of $BiFeO_3$, have only recently been measured[14, 15], and many questions remain about magnon dynamics in more complicated magnetic textures. In Chapter 5, we measure the anisotropy of magnons travelling in the spin cycloid of $BiFeO_3$, and in Chapter 6, we measure the electric field control of magnon currents in a single-domain of La-doped $BiFeO_3$.

The physics of magnon-mediated spin transport in $BiFeO_3$ and related compounds is especially interesting considering the potential applications. If the magnon currents can transfer information about the magnetic state of the magnetoelectric $BiFeO_3$, then a non-volatile in-processor magnetic memory device using only $BiFeO_3$ and spin-charge conversion materials; no ferromagnetic bit is needed. This can have many practical advantages such as 1) antiferromagnets can switch faster than ferromagnets, allowing for lower latency devices, 2) antiferromagnets are more robust against stray fields, and 3) removing the necessity of exchange coupling between the multiferroic and a ferromagnet would simplify the fabrication of the device. Such a simplified memory device can only be possible if electric field switching is able to change the spin carried by a magnon current through the device, and as evidenced in Chapter 6, the magnon signal is not always responsive to switching the ferroelectric polarization. We find that this is due to nontrivial symmetries associated with the magnetic texture of the material. In Chapter 7 we address these symmetries with a phenomenological model for magnon transport that is able to predict when these signals vanish. We expect that this model can be used to guide the design of multiferroic magnon devices.

2 Oxide Epitaxy

In exploring the limits of the spintronic principles mentioned above, the space of epitaxial oxide heterostructures is ideal for searching for new materials and material combinations. Spintronic devices require many different types of materials in contact, including magnets, metals with spin-charge interconversion, and insulators, and in oxide heterostructures these materials can be grown one on top of the other. If the crystal structures of two different oxides are compatible, then epitaxy allows for the interface between the two different materials to be an atomically sharp interface, and removes crystalline grain boundaries. Not only does this simplify the physics in each individual crystalline layer, but epitaxy also gives rise to new physics at the interface, where electronic orbitals from the adjacent materials can align and overlap with each other. Such interfaces are especially important in the field of spintronics, where spin is often expected to diffuse across an interface.

Another important advantage of using epitaxial oxide heterostructures to study spintronics is the tunability inherent in oxide crystals. Among the many tunable parameters in these materials are chemical substitution, or doping, and substrate strain. For example, in Chapter 6, we compare magnon transport across $BiFeO_3$ with magnon transport across $Bi_{0.85}La_{0.15}FeO_3$, and show how the La doping changes the properties of the multiferroic and in turn impacts the magnon transport. Additionally, in Chapter 5, substrates with different lattice parameters are used to create $BiFeO_3$ films with different strain states, and the substrate strain greatly impacts the magnetic texture and allows for totally different magnetic textures, and different modes of magnon transport across those textures, to be realized.

Pulsed Laser Deposition

In order to take advantage of the tunability of epitaxial oxide heterostructures, we use pulsed laser deposition (PLD) as the primary tool for materials synthesis. In PLD, a polycrystalline target is created from oxides of the elements to be used in the crystal. This polycrystalline target is mounted inside a vacuum chamber, along with a single-crystal substrate with the desired lattice constant and crystal structure. A laser delivers energy to a spot on the target, and the target material in the area of this spot is ablated into a plume. Species in the plume travel through the atmosphere of the vacuum chamber and land on the substrate. The substrate is heated, and the species in the plume diffuse across the substrate to grow a film with the desired crystal structure and stoichiometry. There are many deposition parameters to vary in PLD, and these parameters allow us to access the full tunability of epitaxial oxide heterostructures. For example, variations in the target composition allow for variations in doping and the choice of substrate allows us to access different strain states of the heterostructures. Finally, we can control parameters such as Oxygen pressure, substrate temperature, and laser energy, to influence the deposition environment and kinetics and in turn the crystalline quality. As evidenced by the X-ray diffraction and transmission electron microscopy in the following chapters, we are able to grow high quality epitaxial oxide heterostructures using PLD.

Part II
$BaPb_{1-x}Bi_xO_3$

As mentioned in Chapter 1, one way to generate a spin current is through the spin-Hall effect (SHE), and common metals used for their intrinsic SHE include Tungsten, Tantalum, and Platinum. In these metals, the strength of the SHE as given by the spin Hall conductivity σ^z_{xy} can be calculated using the Kubo formalism [16]:

$$\begin{aligned} \sigma^z_{xy} &= \frac{e}{\hbar}\sum_{\mathbf{k}}\Omega^z(\mathbf{k}) = \frac{e}{\hbar}\sum_{\mathbf{k}}\sum_{n} f_{\mathbf{k}n}\Omega^z_n(\mathbf{k}), \\ \Omega^z_n(\mathbf{k}) &= \sum_{n'\neq n}\frac{2\mathrm{Im}[\langle \mathbf{k}n|\, j^z_x\,|\mathbf{k}n'\rangle\,\langle \mathbf{k}n'|\, v_y\,|\mathbf{k}n\rangle]}{(\epsilon_{\mathbf{k}n}-\epsilon_{\mathbf{k}n'})^2} \end{aligned} \tag{2.1}$$

where j^z_x is the spin current operator for spin current moving in x and polarized in z, v_y is the y-velocity operator, $f_{\mathbf{k}n}$ is the Fermi distribution function for the nth band at wavevector $\mathbf{k}$, and $\epsilon_{\mathbf{k}n}$ is the energy of the nth band at wavevector $\mathbf{k}$. The strength of the intrinsic SHE in any given material is directly related to $\Omega^z_n(\mathbf{k})$, or the Berry curvature. In the denominator of Eq. 2.1, the energy difference between two nearly degenerate bands is the most important parameter, and when spin-orbit coupling splits the spin degenerate bands around the Fermi level, the Berry curvature becomes large. Calculations using this formalism of the spin-Hall conductivity have been shown to agree with experimental measurements of the spin-Hall conductivity for several metals [16, 17].

In this intrinsic SHE, it is the band structure of the material that drives the SHE. Another origin of spin-Hall effects in materials is the extrinsic SHE [1], where highly spin-orbit coupled defects and impurities drive spin-dependent scattering. These effects are combined to give the total SHE, and the spin-Hall angle of a given material θ_{SH} is the overall spin hall conductivity divided by the conductivity. Without loss of generality, it can be interpreted as a conversion ratio for charge current in the **x**-direction to a **y**-polarized spin current in the **z** direction. For heavy metals, θ_{SH} is in the range of 0.05-0.3 [16–18]. For topological insulators, θ_{SH} can be higher than 1 [19] (although high resistivity typically makes these materials challenging for applications). However, since θ_{SH} is a property of an isolated material, and the measurement or application of spin currents often requires interfaces with magnetic materials, the spin-orbit torque (SOT) efficiency θ_{SOT} has become a more widely used figure of merit in the community; it is in essence θ_{SH} modified by the qualities of the interface. It measures the strength of the SHE in the context of exerting a torque on a magnetization.

When changing the SHE figure of merit from θ_{SH} to θ_{SOT}, the interface becomes a much more important consideration. In this way, as discussed in Chapter 2, the interfaces of epitaxial oxide heterostructures are highly desirable. Prior work on the SHE of $SrIrO_3$ shows a very high spin-Hall effect in $SrIrO_3/La_{1-x}Sr_xMnO_3$ heterostructures, where $La_{1-x}Sr_xMnO_3$ is an oxide ferromagnet [20]. Interestingly, as the thickness of the $SrIrO_3$ is reduced, the SOT efficiency increases, indicating that the generation and transmission of spins near the interface of the $SrIrO_3$ and $La_{1-x}Sr_xMnO_3$ heterostructures is stronger than that in the bulk.

This is achieved through the use of the epitaxial interface, and inspires further exploration into the SHE in other oxide materials.

In order to explore the limits of θ_{SOT} while maintaining the advantages of epitaxial oxide interfaces, we look for oxides with high spin-orbit coupling, which induces spin-dependent band splitting and high Berry curvature. Typically, the heavier elements have a higher degree of spin-orbit coupling, and since $BaPb_{1-x}Bi_xO_3$ (BPBO) contains Ba, Pb, and Bi, all relatively heavy elements, we decided to measure its charge-to-spin conversion efficiency. In the following chapter, we discover a large spin-orbit torque efficiency in BPBO/$La_{1-x}Sr_xMnO_3$ heterostructures. Interestingly, Berry curvature-based calculations of the spin-Hall conductivity underestimate the experimentally measured value, which suggests that there may be new or exotic charge-to-spin conversion mechanisms at play.

The lattice constant of BPBO is bigger than most perovskites, around 4.3Å, leading to a $\sim$10% lattice mismatch. Despite this mismatch, we can still achieve epitaxial growth of BPBO on perovskites, at temperatures as low as 450°C. This inspires us to deposit other functional perovskites such as multiferroic La-doped $BiFeO_3$ (BLFO) – which is typically deposited at high temperatures – on a BPBO template at 450°C, which is reasonably low enough for CMOS-compatible deposition. In Chapter 4, we demonstrate excellent crystallinity and good ferroelectric functionality of the BPBO/BLFO/BPBO heterostructures even at 450°C. At CMOS-compatible temperatures, this powerful combination of a multiferroic and an electrode with strong spin-to-charge conversion and a history of being a high-temperature superconductor [21] makes BPBO an exciting material for the future of new spintronic physics and applications.

3 Spin Hall Effect in $BaPb_{1-x}Bi_xO_3$

Bismuthates – such as $BaPb_{1-x}Bi_xO_3$ (BPBO)[21] and $Ba_{1-x}K_xBiO_3$ (BKBO)[22] – are a class of complex-oxide superconductors first studied nearly 50 years ago. The materials offer a range of electronic and structural properties that are linked to their flexible chemistry. The parent insulating compound, $BaBiO_3$, hosts a commensurate charge density wave order accompanied by an oxygen breathing mode[23]. Upon cation substitution[24] on either the A or B site the charge density wave order is relaxed and gives way to superconductivity through correlation-enhanced electron-phonon coupling[25]. The structure deviates from ideal cubic perovskites through octahedral rotations, which evolve in composition space, and for Pb doping, lead to a tetragonal-orthorhombic polymorph at superconducting compositions[26]. The electronic properties are dictated by Bi 6*s* and O 2*p* orbital hybridization near the Fermi energy mediated through *spσ* nearest-neighbor hopping[27–29]. This promotes dynamic lattice-correlated properties. However, spin-orbit effects are often considered negligible – while spin-orbit band splitting does occur, it does not happen in bands near the Fermi level [30].

Recently, local inversion symmetry breaking has been observed in bulk BKBO using diffuse X-ray scattering[31], a result that has implications for both the superconducting and normal state properties of bismuthates. Systems with global centrosymmetry may be used to derive hidden forms of spin polarization, generated by local electric fields within the unit cell[32, 33]. Moreover, experiments exploring the breakdown of superconductivity in BPBO have hinted at a hidden two-dimensionality[34–36] despite the three-dimensional structure. In particular, superconducting pairing in bismuthates may be linked to Rashba-type electron-phonon coupling. The local, asymmetric arrangement of substituted cations with different on-site energies[31] could, in principle, drive a large crystal field splitting promoting Rashba-like splitting[5, 6, 37, 38]. In the normal state,

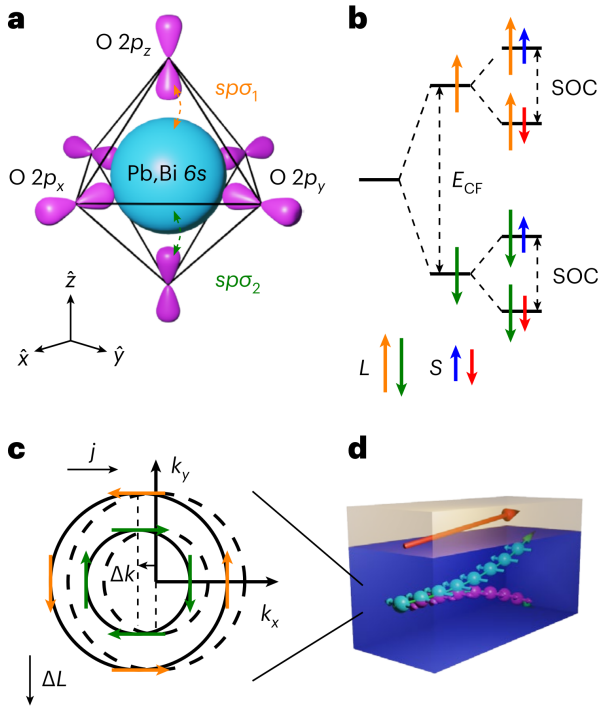

Figure 3.1: **Proposed spin-torque mechanism. a)** Electronic conduction in BPBO is dictated by *spσ* nearest-neighbor hopping. **b)** Energy diagram of band splitting when inversion symmetry is broken. Asymmetric nearest-neighbor hopping now induces crystal field (E_{CF}) splitting of two spin degenerate bands with opposite orbital angular momenta L (orange and green arrows). SOC further splits the orbital bands into spin-split bands with the same orbital angular momentum but opposite spin angular momenta S (blue and red arrows). **c)** Schematic of Rashba-like orbital textured Fermi surface in momentum space with axes k_y and k_x. Colored arrows indicate the opposite orbital angular momenta. The current density j along x shifts the Fermi surfaces along the same axis by an amount Δk and a tangential net orbital angular momentum accumulation ΔL. **d)** When a current is supplied through BPBO (blue layer), a torque acts on the magnetization (orange arrow) of the adjacent ferromagnet (orange layer).

the presence of Rashba spin-splitting could drive spin-charge interconversion that could efficiently be used to manipulate the magnetization in ferromagnetic heterostructures[6, 39–42]. Moreover, Rashba spin-splitting in superconducting heterostructures with Rashba SOC has implications for pairing in locally non-centrosymmetric superconductors [43].

In this chapter, we report a large SOT in thin-film BPBO heterostructures that are in a non-superconducting state but optimally doped for superconductivity ($x = 0.25$). We show that due to the moderate SOC in BPBO, the efficient SOT of 1.7 requires interpretations beyond bulk SHE. We suggest an alternative mechanism in which Rashba-like spin-splitting, sensitive to local inversion symmetry breaking, is responsible (Fig. 3.1). The SOT efficiency (θ_{SOT}) is measured to be around 1.7 and the spin Hall conductivity (σ_{SH}) to be around $1.4 \times 10^5 \frac{\hbar}{2e} \Omega^{-1}\mathrm{m}^{-1}$. This spin Hall conductivity is comparable to that of other efficient spin source materials and is 40 times larger than that predicted for the conventional SHE using first-principles calculations.

Growth, Structural, Magnetic Properties

Interface quality dramatically affects the efficient transfer of spin angular momentum whereas unwanted disorder suppresses superconductivity. In this respect, the fabrication of BPBO heterostructures is made difficult by the relatively large lattice parameter (~ 4.26Å) compared to many common perovskite oxides (around 4Å). Strategies to grow fully or partially coherent epitaxial BPBO have included the use of large lattice parameter substrates [36] and multilayer template engineering [44]. However, despite the large lattice mismatch (greater than 8%), we show that fully relaxed, highly (001) oriented BPBO thin films are possible on common perovskite substrates such as $SrTiO_3$ (STO) and $(La_{0.3}Sr_{0.7})(Al_{0.65}Ta_{0.35})O_3$ (LSAT).

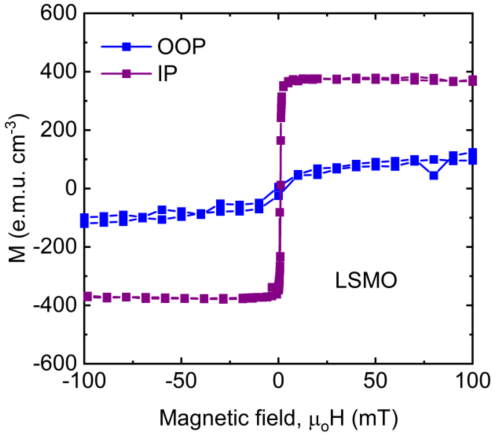

Figure 3.3: **Magnetic characterization.** Superconducting quantum interference device measurements of magnetic hysteresis loops for both in-plane and out-of-plane field directions at 300K for LSMO/BPBO.

To measure SOT in representative all-oxide epitaxial devices, we grew $La_{0.7}Sr_{0.3}MnO_3$ (LSMO) and BPBO bilayers on (001) STO by pulsed laser deposition. BPBO and LSMO were grown by pulsed laser deposition using a 248 nm KrF excimer laser. The LSMO was deposited first at a substrate temperature of 700°C, fluence of 2 J/cm^2, O_2 pressure of 150 mTorr and pulse rate of 5 Hz. The LSMO was cooled to 525°C for BPBO deposition, for which a fluence of 1 J/cm^2, O_2 pressure of 100 mTorr and pulse rate of 5 Hz were used. The samples were then annealed in 400 Torr O_2 at 470°C for 1 hour to improve their transport properties and stability.

Out-of-plane X-ray diffraction and scanning transmission electron microscopy (STEM) were used to confirm the high quality of the heterostructures, which had good crystallinity and a sharp interface between LSMO and BPBO. Fig. 3.2 shows XRD for LSMO (35 nm)/BPBO (65 nm) bilayers on (001) STO grown *in-situ* by pulsed laser deposition. For convenience each complex perovskite structure is treated as pseudocubic. Rocking curves of (002) peak for

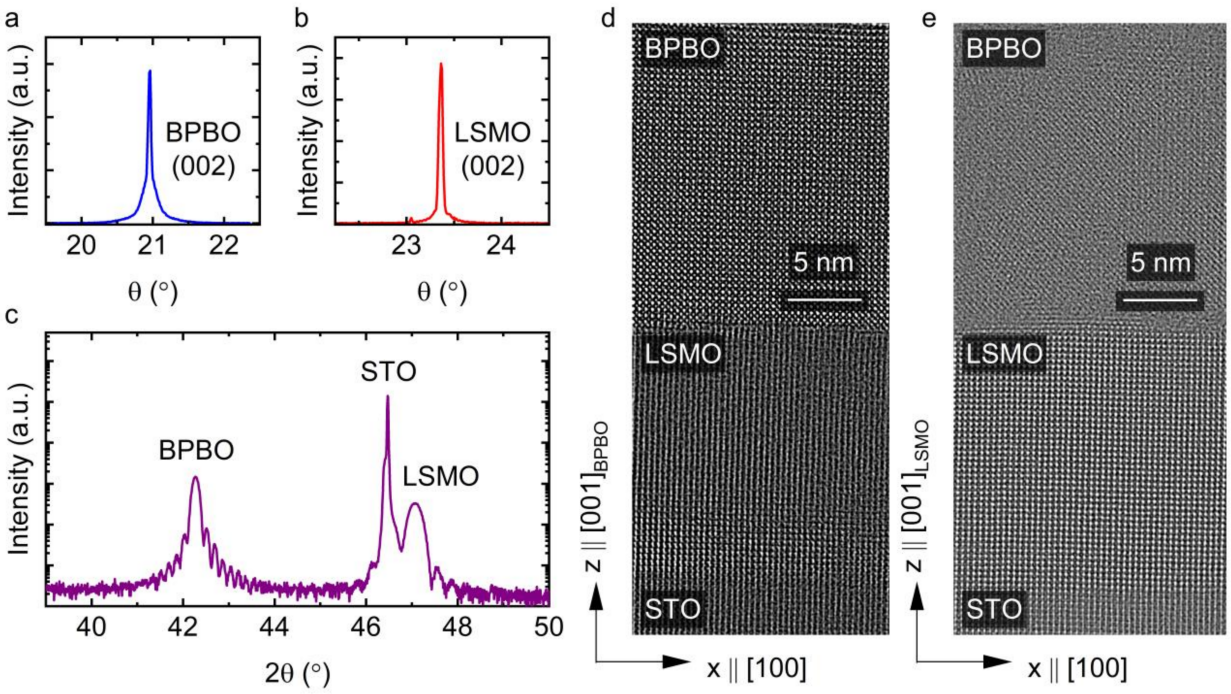

Figure 3.2: **Structural characterization of LSMO/BPBO bilayers. a)** X-ray diffraction rocking curve of (002) BPBO peak. **b)** Rocking curve of (002) LSMO peak. **c)** Symmetric $\theta - 2\theta$ scan around labeled (002) peaks of BPBO, STO, and LSMO. **d)** Scanning transmission electron microscope image of BPBO/LSMO on (001) STO aligned to BPBO. **e)** Image aligned to LSMO. Rotation is 2 mRad about the x-axis.

both BPBO (Fig. 3.2a) and LSMO (Fig. 3.2b) show good crystallinity with FWHM of 0.02°. From symmetric $\theta - 2\theta$ scans of the (002) peaks for BPBO, STO, and LSMO in Fig. 3.2c we estimate the out-of-plane lattice parameters of BPBO and LSMO to be 4.27Åand 3.86 Å. Keissig fringes indicate smooth surfaces. The lattice parameter of BPBO is similar to theoretical bulk values, and optimized thin films confirm the high quality, fully relaxed state. The smaller out-of-plane lattice parameter of LSMO compared to bulk is due to the tensile strain of LSMO on STO. Further structural characterization is done using STEM. Fig. 3.2d shows an image with zone axis aligned to the BPBO film while Fig. 3.2e is aligned to both LSMO and STO. The 2 mRad difference in alignment could be due to sample bending or tilting of the BPBO epitaxial relationship. Although the mismatch between BPBO and LSMO is large, the interface appears well-ordered with crystallinity of both the relaxed BPBO and LSMO maintained near the interface.

In-plane and out-of plane magnetic hysteresis loops shown in Fig. 3.3 were carried out in a Quantum Design MPMS XL. In-plane magnetic fields are applied along the [100] crystallographic direction of the substrates. LSMO exhibits an in-plane magnetic hard axis, with in-plane saturation magnetization around 400 emu/cm^3, which is consistent with the bulk value.

SOT Efficiency

Spin-torque ferromagnetic resonance (ST-FMR) [45, 46] was used to probe the current-driven torque in LSMO/BPBO heterostructures (shown schematically in Fig. 3.5b). Polarized spin accumulation at the interface of BPBO interacts with the adjacent LSMO and exerts a torque on the magnetization. Oscillating fields generated by the injection of radio frequency (rf) current (I_{rf}) drive the magnetization in LSMO through resonance while sweeping an external in-plane magnetic field (H_{ext}). The resonance signal is read as a mixing voltage (V_{mix}) of I_{rf} and anisotropic magnetoresistance. The resulting resonance peak was fitted using symmetric (V_{S}) and antisymmetric (V_{A}) Lorentzian functions proportional to the damping-like (τ_{DL}) and field-like (τ_{FL}) torque components, respectively, as shown in Fig. 3.5c. Using established methods [45], the SOT efficiency ($\theta_{\mathrm{SOT}} = (2e/\hbar) j_{\mathrm{S}}/j_{\mathrm{C}}$) was then determined from the ratio of the symmetric to antisymmetric amplitudes to be ~ 1.7 on average. Here j_{S} and j_{C} are the spin and charge current densities, respectively.

These measurements were done using a BNC 845 rf signal generator to supply a fixed gigahertz-frequency current at 15 dBm, applied to the sample through a bias tee and a three-tipped ground-signal-ground probe (Fig. 3.4a). For each frequency, we swept over a range of fields and measured the mixing voltage using a Keithley 2182A nanovoltmeter on the d.c. end of the bias tee (Fig. 3.4b). For Hall-ST-FMR and angle-dependent measurements, an amplitude-modulated (AM) gigahertz-frequency signal was sourced from an E8257D analog signal generator. SR830 lock-in amplifiers measured the d.c. responses from the bias tee and across a sample with patterned Hall contacts. Both lock-in amplifiers referenced the same AM signal, with $f_{\mathrm{AM}} \approx 1,700$ Hz and microwave frequencies in the range 3-5GHz. The in-plane field was applied at various angles using a projected-field magnet.

To disentangle possible artifacts due to spin pumping and resonant heating, we performed resonant line fitting for both longitudinal (V^{XX}) and transverse (V^{XY}) voltages at many in-plane field angles ϕ, as described in ref. [46]. The dependence of the symmetric and antisymmetric components on ϕ for both longitudinal and transverse signals is shown in Fig. 3.5d,e. We find good agreement for the fit of the longitudinal amplitudes with a $\sin(2\phi)\cos(\phi)$ contribution consistent with the product of anisotropic magnetoresistance in LSMO and conventional Slonczewski-like spin torques of the form $\tau_{y,\mathrm{DL}} \propto \hat{m} \times (\hat{m} \times \hat{y})$ and $\tau_{y,\mathrm{FL}} \propto \hat{m} \times \hat{y}$ with charge current in the $\hat{x}$ direction and orthogonal in-plane spin polarization. Additionally, the symmetric and antisymmetric transverse signals were fitted as:

$$V_S^{XY}(\phi) = S_{XY}^{\mathrm{PHE/art}} \cos(2\phi)\cos(\phi) + S_{XY}^{\mathrm{AHE/art}} \cos\phi, \tag{3.1}$$

$$V_A^{XY}(\phi) = A_{XY}^{\mathrm{PHE}} \cos(2\phi)\cos(\phi) + A_{XY}^{\mathrm{AHE}} \cos\phi, \tag{3.2}$$

where $S_{XY}^{\mathrm{PHE/art}}$ and $S_{XY}^{\mathrm{AHE/art}}$ are the symmetric amplitudes with the respective planar Hall effect (PHE) and anomalous Hall effect (AHE) voltages convoluted with artifact voltages. A_{XY}^{PHE} and A_{XY}^{AHE} are the antisymmetric amplitudes due to the PHE and AHE voltages, respectively. From this, the artifact voltages due to spin pumping or resonant heating were found to be negligibly small, ensuring accurate evaluations of θ_{SOT} (see Appendix A). The measured SOT efficiency for many devices with various thicknesses of BPBO are presented in Fig. 3.5f.

In addition to SOT efficiency, structural and electronic properties are measured across

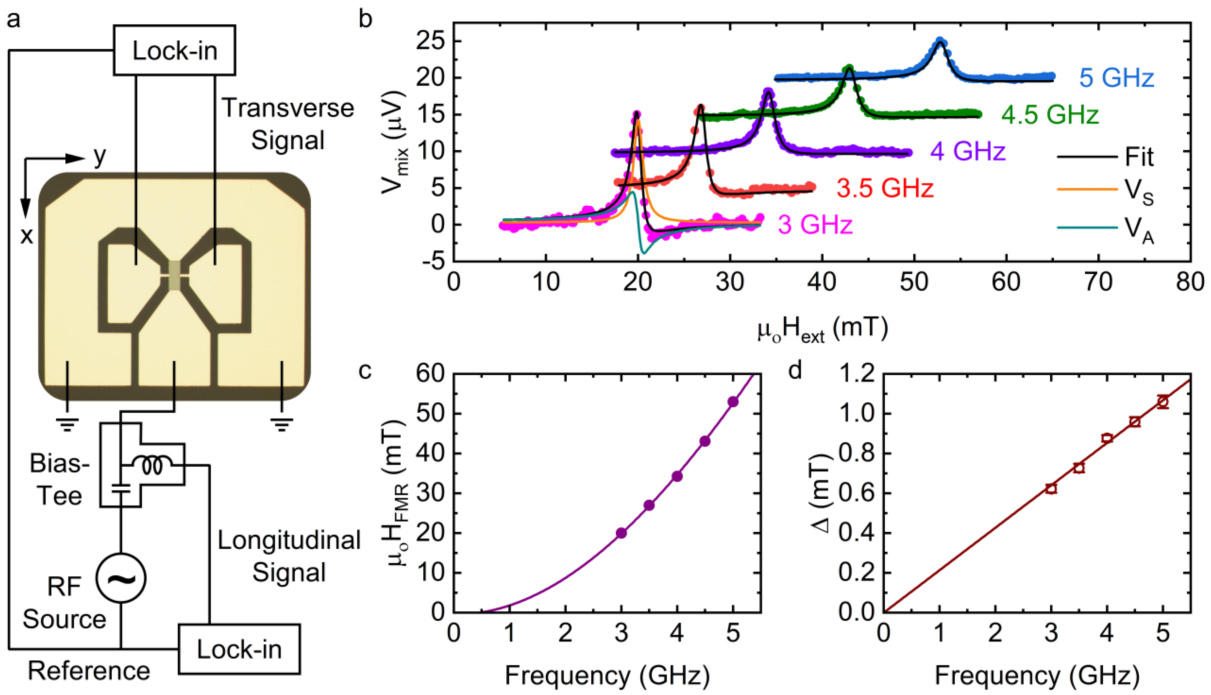

Figure 3.4: **Spin-torque ferromagnetic resonance a)** Schematic of the device geometry and measurement configuration. **b)**Resonance spectrum with varying frequency, each fit with a symmetric (V_S) and antisymmetric (V_A) Lorentzian function. **c)** Resonance magnetic field, H_{FMR}, as a function of frequency, fit to the Kittel formula giving $M_{eff} = 390$kA/m. **d)** Frequency dependence of linewidth broadening Δ, with a linear fit to extract the Gilbert damping parameter $\alpha = 0.008$.

representative thicknesses, as shown in Fig. 3.6. LSMO remains coherently strained in the thickness range studied, while BPBO is fully relaxed. The Kiessig fringes and 2θ broadening trend with thickness. XRD from two representative samples with different thicknesses are shown in Fig. 3.6b. The resistivity of BPBO varies as in Fig 3.6c which may influence SOT efficiency. Thinner samples show higher resistivity consistent with ref. [36], and BPBO becomes insulating for thicknesses less than 5nm. However, there is additional noise which may be attributed to variation in the growth.

Large efficiencies are observed for all devices, with thinner BPBO samples showing slightly larger efficiencies. The sample-to-sample variation could explain the lack of clear thickness dependence in SOT shown in Fig. 3.5f, and prevents us from drawing conclusions about any physics associated with the thickness dependence. Our results are therefore inconclusive in determining if the dominant mechanism is strictly due to either interfacial or bulk conduction. However, the lack of a purely interfacial interpretation and the persistent SOT in devices with thicker BPBO suggests bulk conduction of BPBO may contribute.

Origin of SOT in BPBO-based heterostructures

The observation of an SOT efficiency of 1.7 here is combined and published with alternative measurements of the SOT efficiency, including nonlinear d.c. Hall effect and magnetization switching [47]. The published SOT efficiency in ref. [47] is 2.7, which emphasizes the ro-

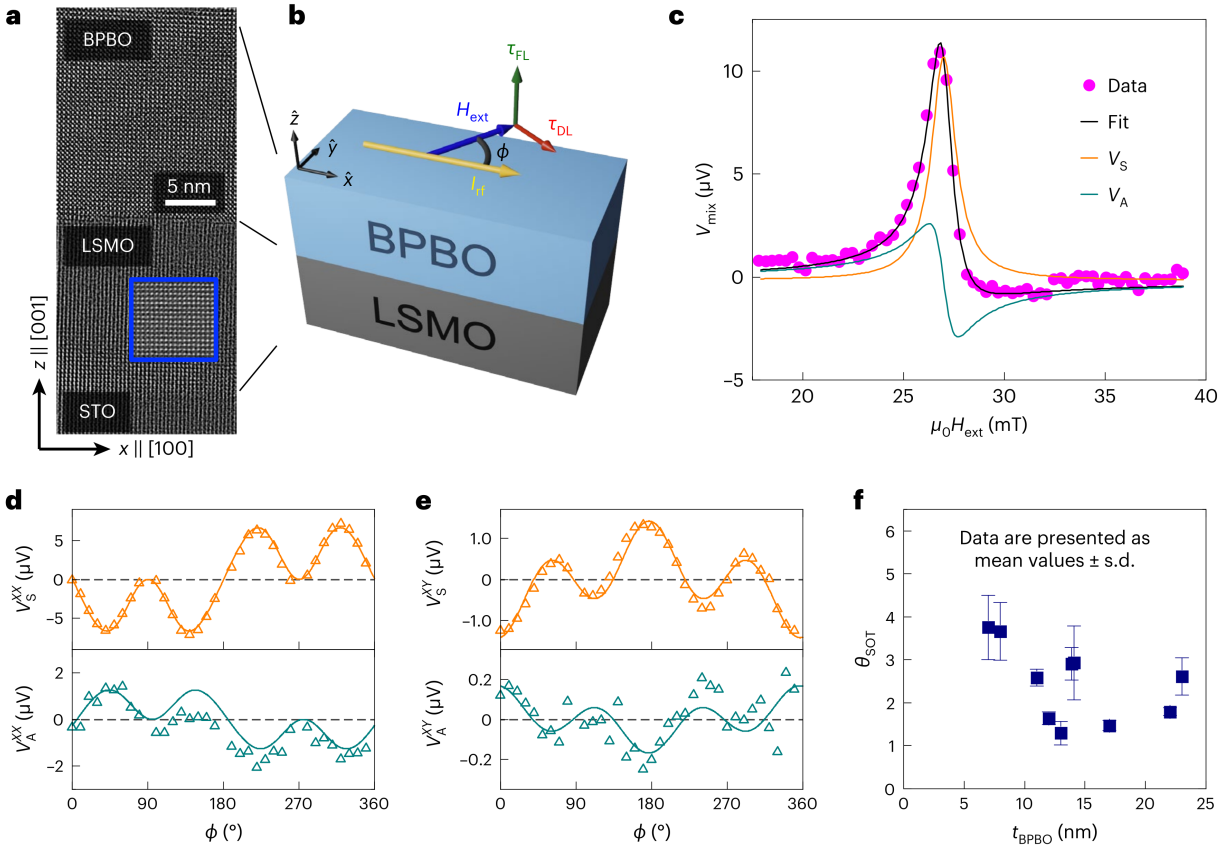

Figure 3.5: **Hall ST-FMR and ST-FMR summary of LSMO/BPBO bilayers. a)** STEM image of LSMO/BPBO on (001) STO, aligned to BPBO [001] (inset aligned to LSMO [001]). **b)** Schematic of the bilayer geometry for measuring damping-like torque (τ_{DL}) and field-like torque (τ_{FL}) where ϕ is the angle between the rf current and the in-plane magnetic field. **c)** Mixing voltage V_{mix} from the ST-FMR signal with the corresponding fit for LSMO (35nm)/BPBO (17nm) with an rf frequency of 3.5 GHz and ϕ at 225°. **d)** Field dependence of symmetric (V_S^{XX}) and antisymmetric (V_A^{XX}) amplitudes of the longitudinal ST-FMR signal with fits to $\sin(2\phi)\cos(\phi)$ for LSMO (14nm)/BPBO (14nm) at 3.5 GHz. **e)** Transverse signals of **d** with symmetric (V_S^{XY}) and antisymmetric (V_A^{XY}) amplitudes fit to Eq. 3.1 and 3.2. **f)** SOT efficiency θ_{SOT} for deices with various BPBO thicknesses. The error bars are standard deviation estimates of the uncertainty including error propagation of parameters in the fit analysis and sample-to-sample variations. For samples with higher θ_{SOT}, the asymmetric Lorentzian components are smaller and more difficult to extract, thus typically leading to higher error primarily due to the larger uncertainty in the fit. Measurements with an uncertainty larger than 30% were not included.

bustness of the result of giant SOT efficiency in BPBO-based heterostructures. The different measurement techniques along with a variety of growth methods for the BPBO films and the magnetic materials strengthen the result and make it applicable to future studies employing diverse combinations of materials. Compared to other spin source materials (Table 3.1), the SOT efficiency is as large as or greater than the most efficient material systems reported, including heavy metals, two-dimensional materials, and topological insulators. This is of note because BPBO is not expected to have strong SOC near the Fermi energy.

The largest contributions to calculated spin Hall conductivities in heavy metals arise due to SOC-induced spin-splitting of nearly degenerate bands in momentum space. How-

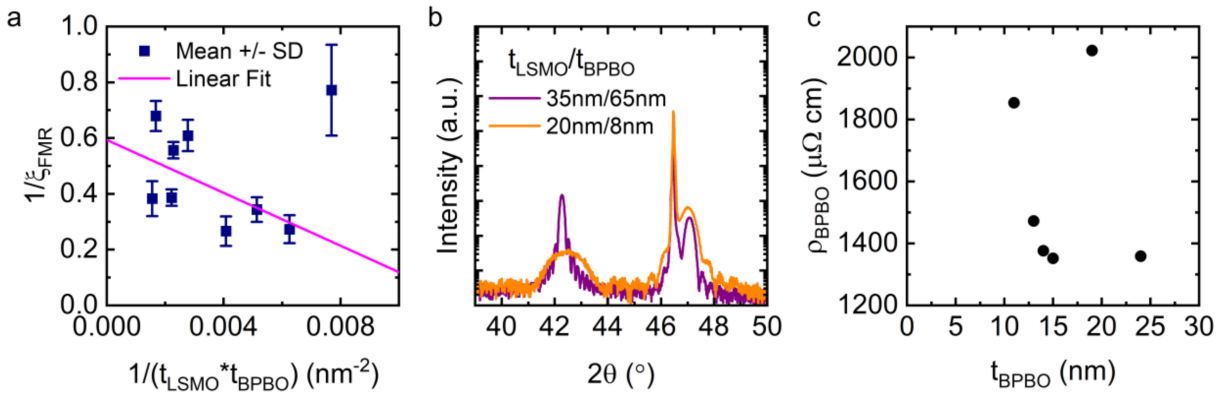

Figure 3.6: **Thickness dependence. a)** Thickness dependence of SOT efficiency calculated using lineshape analysis. Data is linearly fit and damping-like torque is calculated from the intercept while the field-like torque is calculated from the slope. The error bars are standard deviation estimates of uncertainty including error propagation of parameters in the fir analysis and sample-to-sample variations. Measurements with uncertainty larger than 30% were not included. **b)** Symmetric $\theta - 2\theta$ scan around (002) peaks of BPBO, STO, and LSMO for two samples with different thicknesses labeled. **c)** Thickness dependence of isolated BPBO thin film resistivity grown on (001) STO.

ever, the conduction in BPBO is dominated by its weakly spin-orbit-coupled O $2p$ orbital character. From first-principles calculations of the conventional SHE (see Appendix B), the estimated spin Hall conductivity in BPBO is only $\sigma_{\mathrm{SH}} = 3400\frac{\hbar}{2e}\Omega^{-1}\mathrm{m}^{-1}$, which is nearly 70 times smaller than our experimental value. We also considered the effect of rigid octahedral rotations in BPBO[26]. However, applying these rotations has little effect on the calculated spin Hall conductivity, suggesting that these particular distortions and any associated phase separation[48] or octahedral rotation-based strain relaxation are unlikely to explain our results. The large discrepancy between the experimental and the calculated values leads us to conclude that conventional SHEs alone cannot account for our experimental observation.

Instead, we speculate that the giant SOT in bismuthate heterostructures may be attributed to hidden Rashba-like effects promoted by local inversion symmetry breaking. Efficient spin polarization utilizing Rashba effects associated with inversion symmetry breaking has been widely reported in systems including metallic interfaces[40], oxide two-dimensional electron gases[41], heavy metal/ferromagnet/oxide systems[39, 42], and polar semiconductors[54]. Furthermore, inversion symmetry breaking need not apply globally. That is, it may occur only at the interface or in crystal structure. This is highlighted by hidden spin polarization predicted theoretically[32, 33] and observed experimental[55–60] in globally centrosymmetric systems due to electric fields associated with the local symmetry. The recent observation of local inversion symmetry breaking seen in BKBO[31] raises the possibility of hidden Rashba physics in bismuthates not captured in our first-principles calculations. In principle, local inversion symmetry breaking in BPBO due to the distinct electrostatic environments of random cation substitutions could result in the asymmetric orbital hybridization of nearest neighbours. These local dipoles create crystal field splitting of bands with opposite orbital chirality (Fig. 1c), a phenomenon termed the orbital Rashba effect[5–7]. In the limit of much larger crystal field splitting, the SOC acts as a perturbation and, thus, the contributing effects of atomic spin-orbit interactions are maximized[38]. Because of SOC

Table 3.1: **Comparison of SOT efficiency, spin Hall conductivity, and critical current density for magnetization switching for several spin source materials.** j_{sw} is the current density only through the nonmagnetic layer.

Spin Source Material	θ_{SOT}	σ_{SH} $\left(10^5 \frac{\hbar}{2e} \Omega^{-1} m^{-1}\right)$	$j_{sw}(Acm^{-2})$
$BaPb_{0.75}Bi_{0.25}O_3$ (this work)	1.7	1.4	4.0×10^5 [47]
$SrIrO_3$ [49]	0.58	0.5	5.1×10^6
Bi_xSe_{1-x} [19]	18.61	1.5	4.3×10^5
WTe_2 [50, 51]	0.09	0.12	3×10^6
$Pt_{0.7}(MgO)_{0.3}$ [52]	0.26	4	1.15×10^7
β-Ta [53]	-0.15	-0.8	8.6×10^6

within O $2p$ orbitals is weak, the primary role of local inversion symmetry breaking is to establish a large crystal field splitting. The crystal field splitting is independent of SOC and the subsequent role of SOC is to spin-split the degenerate orbital bands (Fig. 3.1b).

We emphasize that our proposed orbital torque mechanism remains largely qualitative and requires further experiments and advancements in theory to confirm. Rather than the bulk orbital Rashba effect, a purely interfacial Rashba effect may exist due to an electric field generated by inversion symmetry breaking at the interface. As noted, the thickness dependence is inconclusive in determining if SOT is purely interfacial. However, an apparent lack of field-like torque in our devices, as discussed in Appendix A, is inconsistent with previous reports on interfacial spin Rashba SOT[61, 62]. Future studies exploring the interfacial effects at relevant length scales may benefit from the further development of methods to reduce the epitaxial lattice mismatch.

Conclusions

Bismuthate heterostructures are versatile systems that challenge traditional concepts in materials engineering for producing efficient spintronics. New approaches, well suited to complex oxides, may include structural and orbital engineering rather than conventional strategies focused on increasing atomic SOC. The physical properties of bismuthates are highly sensitive to the bonding environment, which is tunable by cation substitution. Although local inversion symmetry breaking has been observed in BKBO, there are distinct differences in its global bonding environment compared to other bismuthates, such as BPBO. The relationships between the bonding environments, global crystal symmetry, and local structural distortions are poorly understood at this time and should subsequently be addressed. Future

studies may provide further insights into the structural and orbital contributions by chemical substitution in BPBO, BKBO, or an analogous superconducting compound $Ba_{1-x}K_xSbO_3$ (ref. [63]). Moreover, the implementation of other complex oxides, such as magnetoelectric perovskites[9] and magnetic insulating oxides[64, 65], could eliminate current shunting problems, improve performance and introduce additional functionality. Although our results are strictly for the normal, non-superconducting state, they have intriguing implications for the superconducting properties as well. The observation of current-driven fields in the normal state of a locally non-centrosymmetric superconductor suggests that these heterostructures may support parity mixing or topological phases[43]. Our results serve to stimulate further exploration of the interplay between hidden spin polarization and superconductivity in bismuthate heterostructures.

In conclusion, we have reported a SOT in BPBO-based heterostructures with an efficiency of around 1.7 and a spin Hall conductivity of $1.4 \times 10^5 \frac{\hbar}{2e} \Omega^{-1} m^{-1}$. This spin Hall conductivity is 40 times larger than that predicted for the conventional SHE using first-principles calculations. Questions remain regarding the exact origin of this effect, but we suggest that the unexpectedly large current-induce torques may be the result of an orbital Rashba effect associated with local inversion symmetry breaking in BPBO, which has previously been observed with diffuse X-ray scattering in BKBO[31]. Our results highlight the need to widen the exploration of spin manipulation to include materials and mechanisms that may not rely solely on large intra-atomic SOC. Furthermore, our observation of a large charge-to-spin conversion in the non-superconducting state of bismuthate heterostructures suggests that they could be a model system for investigating the interplay of hidden spin-orbit phenomena and superconductivity. Ultimately, our work could provide new routes in materials engineering that can be used to develop efficient spin-orbitronics.

4 Low Temperature Epitaxy of $BaPb_{1-x}Bi_xO_3$ (BPBO) and $Bi_{0.85}La_{0.15}FeO_3$ (BLFO) Trilayers

Continuing in the theme of BPBO, we discuss the enabling of low temperature multiferroic thin film growth by grapho-epitaxy on BPBO electrodes. Multiferroic materials allowing for the effective control of (anti)ferromagnetic order with an electric field or control of electrical polarization with a magnetic field [8, 66–69]. These properties make them desirable for applications in magnetic field sensing and novel magnetic memory designs for ultrafast and efficient nonvolatile, in-memory computing. One such design, the so-called magnetoelectric spin-orbit logic device, makes use of multiferroics along with a spin-orbit coupled material for efficient reading and writing of a nanomagnetic bit[9]. The perovskite bismuth ferrite ($BiFeO_3$, BFO) - with a robust spontaneous polarization ($\sim$ 1 C/m^2 aligned along the pseudocubic $\langle 111 \rangle$ direction) and canted antiferromagnetic (L) order - is one of the most promising multiferroics due to its high ferroelectric Curie (1143 K) and Néel (643 K) temperatures[70]. Furthermore, the electrically insulating nature of BFO offers a promising path for magnonic devices, where the transfer of spin via magnons plays a key role in energy-efficient and fast information processing[14]. To tune the multiferroic properties of thin-film BFO such as the coercive field and magnetic and polar orders, rare-earth cation doping (e.g., with lanthanum as in $Bi_{1-x}La_xFeO_3$, BLFO) is typically used[71].

Along with cation doping, the choice of substrate and bottom electrode also has a significant impact on the multiferroic properties of BFO thin films. Epitaxial BFO and BLFO thin films are typically grown on metallic perovskites (e.g., $SrRuO_3$, SRO) at high temperatures (650-800°C), and on lattice-matched substrates (e.g., $DyScO_3$, $TbScO_3$, and $SrTiO_3$, STO)[14, 66–69, 72–75]. For device integration, however, it is essential to select a substrate and growth temperature that is compatible with silicon-CMOS processing, while maintaining the desired properties of the B(L)FO films and the bottom electrode[76]. It is known that STO can be deposited epitaxially on silicon substrates[77], however, the B(L)FO growth temperatures of 600-800°C are incompatible with traditional CMOS processing, which typically requires fabrication temperatures of no more than 450°C[76, 78] to avoid damage to underlying CMOS components. The lattice mismatch with CMOS materials leads to challenges in fabrication processes, which require efforts to process the epitaxial BFO growth on very different lattice structures. This may involve the use of buffer layers (primarily discussed here), specialized fabrication techniques (such as pulsed-laser deposition), and innovations in material engineering. Attempts have been made to grow BFO at low temperatures, but the resulting films are polycrystalline with diminished ferroic properties[79–81].

Here, we demonstrate highly [001] textured/epitaxial growth of $Bi_{0.85}La_0.15FeO_3$ (BLFO) thin film on the metallic perovskite $BaPb_0.75Bi_0.25O_3$ (BPBO) at a substrate heater temperature as low as 450°C on STO (001) substrates. This approach addresses major concerns of compatibility with CMOS processing and shows promise for practical applications. From a technological perspective, we believe the total concentration of lead should be well below what is the allowable limit; the mass of Pb on a 6-inch CMOS waver (500μm thick) is calculated to be 0.02ppm, which is under the permissible limit of 1000 ppm[82]. The electrode system, BPBO, is known for its historical significance as one of the first high transition temperature oxide superconductors prior to the discovery of the cuprates and exhibits

a superconducting transition temperature of $\sim$ 11 K[83] at a composition $x = 0.25$. Its normal, metallic state at room temperature is characterized by a resistivity of $\sim 2\text{m}\Omega\cdot\text{cm}$ [47]. As discussed in the previous section, in addition to superconductivity, BPBO has a strong spin-Hall effect, making it attractive for potential use in spintronic devices. Here, we address the low-temperature synthesis requirements for CMOS compatibility and combine the promising transport physics of the BPBO electrode with the robust ferroelectricity in BLFO, opening the door to testing and implementation of multiferroics integrated into CMOS devices. Specifically, this work investigates and compares all-epitaxial heterostructures of BPBO/BLFO/BPBO grown using pulsed-laser deposition (PLD) at 450°C to standard PLD deposited SRO/BLFO/SRO heterostructures grown at high temperatures (700°C) and low temperatures (450°C).

Growth, Structural Properties

All thin films are prepared by PLD using a 248 nm KrF excimer laser with a target-substrate distance of 5 cm. STO (001) substrates are used for all depositions. The BPBO target is prepared with 10% excess of Pb and Bi, the BLFO target for use in low temperature depositions is stoichiometric, and the BLFO target for use in high temperature depositions has 18% excess Bi. The SRO target is stoichiometric. For low temperature BPBO/BLFO/BPBO films, the process is as follows: the first BPBO layer is grown at 450°C in 100 mTorr of O_2 with a 5Hz pulse rate at 0.13 J/cm^2. This first layer is annealed in situ at 435°C in 400 Torr O_2, and then the temperature is reset to 450°C and the pressure is set to 50 mTorr O_2 for the BLFO deposition, which is done with a pulse rate of 1 Hz at 1.5 J/cm^2. Finally, the top BPBO layer is grown with the same conditions as the bottom BPBO layer and then the heterostructure is cooled to room temperature. The SRO/BFO/SRO films are grown with the following process: both SRO layers are deposited in 100 mTorr O_2, with a pulse rate of 5 Hz at a fluence of 0.8J/cm^2. The BLFO is deposited in 110 mTorr O_2, with a pulse rate of 10 Hz at a fluence of 1.8J/cm^2, and this is all done at 450°C and 700°C.

The crystalline quality of the BPBO/BLFO/BPBO trilayers is compared to that of standard high-temperature SRO/BLFO/SRO trilayers as well as that of low-temperature SRO/BLFO/SRO trilayers using X-ray diffraction (XRD) and reciprocal space mapping (RSM). While BPBO and BLFO both share a perovskite lattice structure, there is a $\sim$ 9% lattice mismatch between BPBO and BLFO, and one would not expect any templating of the [001] orientation of the BLFO layer on such a surface. Surprisingly, it is found that all layers in the BPBO/BLFO/BPBO heterostructure grow with [001]-oriented "cube-on-cube" (Fig. 4.1a) epitaxy in a single phase even at 450°C. We posit that this is enabled by the low-temperature epitaxial growth of the BPBO electrode. On the other hand, the SRO quality is severely affected at 450°C, which leads to poor BLFO growth. This is demonstrated by

Table 4.1: **Lattice parameters from RSM.** In-plane (a) and out-of-plane (c) lattice parameters are given for sample I (BPBO/BLFO/BPBO at 450°C), sample II (SRO/BLFO/SRO at 700°C), and sample III (SRO/BLFO/SRO at 450°C).

	BLFO		SRO		BPBO	
Sample	a (Å)	c (Å)	a (Å)	c (Å)	a (Å)	c (Å)
I	3.96	3.96	-	-	4.31	4.29
II	3.91	4.00	3.91	3.96	-	-
III	3.95	3.95	3.93	3.92	-	-

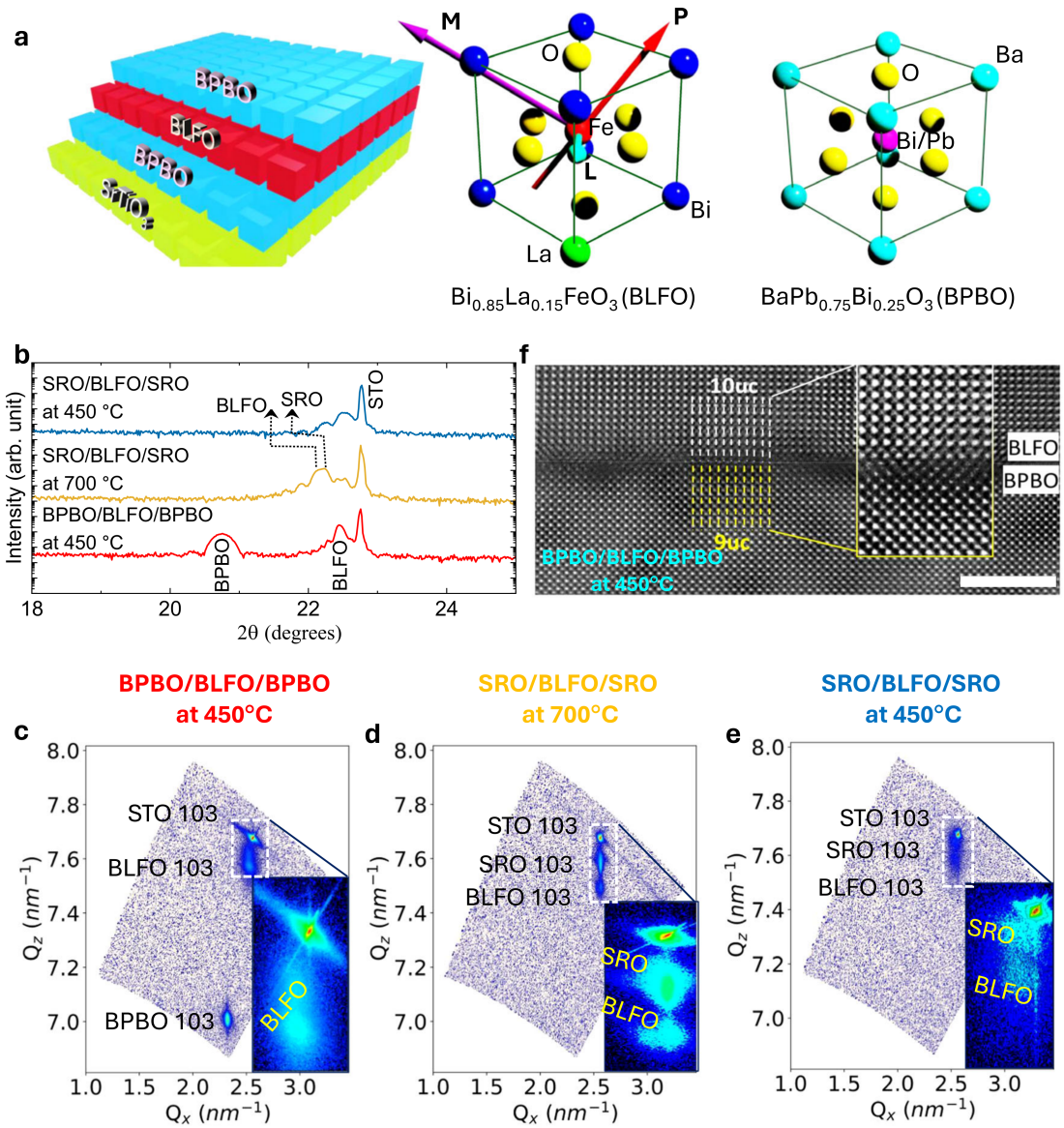

Figure 4.1: **Structural Characteristics.** **a)** Schematic depicting the cube-on-cube growth of BPBO/BLFO/BPBO on STO substrate, alongside unit cells of BLFO and BPBO. The BLFO unit cell is decorated with arrows representing the order parameters polarization **P**, magnetization **M**, and Néel Vector **L**. **b)** $2\theta - \omega$ X-ray diffraction patterns of BPBO and SRO based heterostructures prepared at different temperatures. Reciprocal space mapping of **c)** BPBO/BLFO/BPBO grown at 450°C, **d)** SRO/BLFO/SRO grown at 700°C, and **e)** SRO/BLFO/SRO grown at 450°C. Insets are zoomed cross-sections of the BLFO, SRO, and STO peaks. **f)** Cross-sectional HAADF-STEM image of BLFO/BPBO interface deposited at 450°C. The magnified image (inset) reveals 10uc/9uc domain epitaxy between BLFO and BPBO. The scale bar is 10 Å.

the RSM studies; the 450°C BPBO peak is sharp and shows thickness oscillations indicating high-quality growth, whereas the 450°C SRO peak is diffuse indicating poor coherence, and the resulting BLFO peak on 450°C SRO is much more diffuse than the BLFO peak on 450°C BPBO.

From the diffraction results, we calculate lattice constants for our heterostructures as shown in Table 4.1. The in-plane and out-of-plane lattice constants a and c respectively are calculated using the following formulas:

$$a = \frac{\lambda\sqrt{h^2+k^2}}{2Q_x} \quad \text{and} \quad c = \frac{\lambda l}{2Q_z} \tag{4.1}$$

where h, k, l are the indices for the diffraction peak (103 in this case), λ is the wavelength (Cu K-α, 1.5418Å), and Q_x and Q_z are the parallel and perpendicular wavevectors of the RSM peaks. Since the a values are the same for the high temperature SRO/BLFO/SRO samples, the BLFO is strained to the SRO bottom electrode, but for the BPBO/BLFO/BPBO heterostructure, the BLFO is completely relaxed, which is expected given the large lattice mismatch.

Thin-film epitaxial growth is typically constrained by (1) lattice misfit between substrate and film, (2) variations in the thermal expansion coefficients of the different materials, and (3) microstructural strains due to the defects or substitution dopants. The thermal expansion coefficients of BFO ($10 - 14 \times 10^{-6}$/K) [84], $BaPbO_3$ ($10 - 15 \times 10^{-6}$/K) [85] and the STO substrate (9×10^{-6}/K) (Crystec-GmbH) are similar; therefore it is not expected that thermal expansion mismatch inhibits epitaxial growth. It is established that a film-substrate lattice difference of greater than 7% (up to 22% or in some cases 30%[86]) leads to film growth via grapho-epitaxy[87], also known as domain-matching epitaxy[88], where lattice matching is achieved by different multiples of lattice constants between the two layers. This effectively fixes the lattice misfit between BPBO and BLFO: 10-unit cells of BLFO and 9-unit cells of BPBO are expected to be accommodated with $\sim 1\%$ of mismatch. High-angle annular dark-field scanning transmission electron microscopy (HAADF-STEM) images (Fig. 4.1f) confirm the epitaxial growth of BLFO on BPBO as described above based on domain-matching epitaxy.

In contrast, the SRO grows poorly at 450°C; the diffraction measurements indicate a significant loss of crystalline ordering during low-temperature growth as compared to high-temperature growth at 700°C. This indicates that the electrode quality is critical for good growth of the BLFO layer. Furthermore, it is known that the Pb-O terminated surface provides low surface energy ($\sim$1 eV/nm^2)[89] for adatoms and potentially helps in the nucleation process to grow epitaxial BLFO at sufficiently low temperature in comparison to the high surface energy of the Sr-O surface ($\sim$6 eV/nm^2)[90]. When BLFO is grown directly on STO substrates at 450°C, it is polycrystalline, compared to epitaxial when grown at 700° (Fig. 4.2). This indicates that the high-energy Sr-

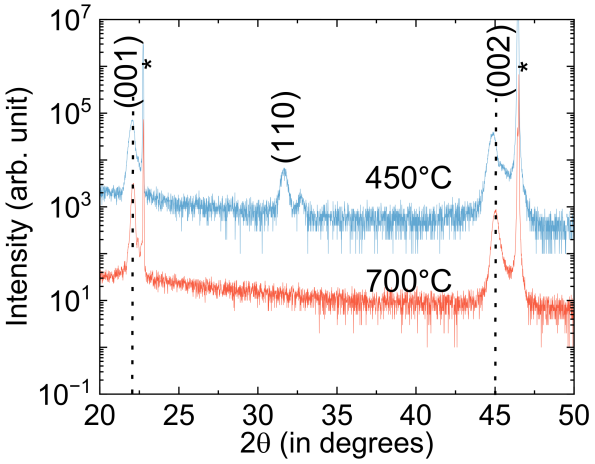

Figure 4.2: **X-ray diffraction of BLFO.** Patterns show crystallinity of BLFO deposited on a bare STO substrate at 700°C and 450°C. The presence of the extra (110) peak in the 450°C deposition implies polycrystallinity, while the 700°C film is epitaxial.

O surface requires increased temperatures for epitaxy, or a relatively low surface such as the Pb-O surface that can be grown epitaxially at 450°C.

TEM

To understand the effect of growth temperature on the polar state of BLFO, we have performed a detailed analysis of HAADF-STEM images. First, we compare the structural TEM images shown in Fig. 4.1f and Fig. 4.3. While the atomically-resolved BPBO/BLFO/BPBO and high temperature SRO/BLFO/SRO interfacial images show sharp interfaces, the interfaces in the low temperature SRO/BLFO/SRO sample are diffuse and show dislocations and other defects. It is interesting to compare the interfaces between the BPBO/BLFO/BPBO and the high temperature SRO/BLFO/SRO samples: while the SRO/BLFO/SRO interface is atomically sharp up to the last unit cell, there is a 2-3 unit cell boundary between the BPBO and BLFO where the 9% mismatch is accommodated, resulting in grapho-epitaxy, where 9 unit cells of BPBO line up with 10 unit cells of BLFO. We expect this interfacial layer to be primarily composed of lead or bismuth oxide.

The high quality HAADF-STEM imgaes also allow us to measure the structural distortion within the layers, and thus the atomic displacement of the Fe-atom. One can infer the degree of polar order from this data: common perovskite ferroelectrics such as $BaTiO_3$, $PbTiO_3$, and BFO all exhibit a direct relationship between the spontaneous dipole moment and the

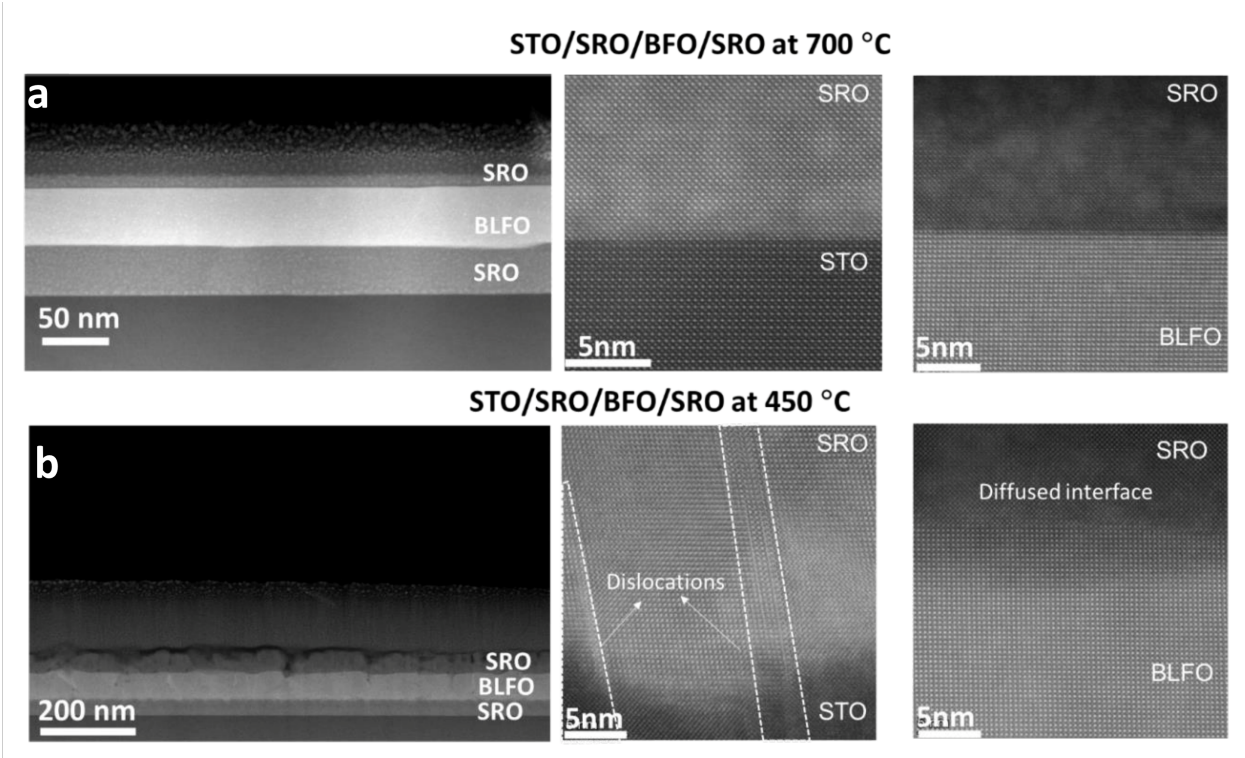

Figure 4.3: **High resolution TEM images.** SRO/BLFO/SRO films deposited at **a)** 700°C and **b)** 450°C. The epitaxial quality of **a** is readily apparent in the smooth atomically flat interfaces, compared to the diffuse interfaces and roughness of **b**.

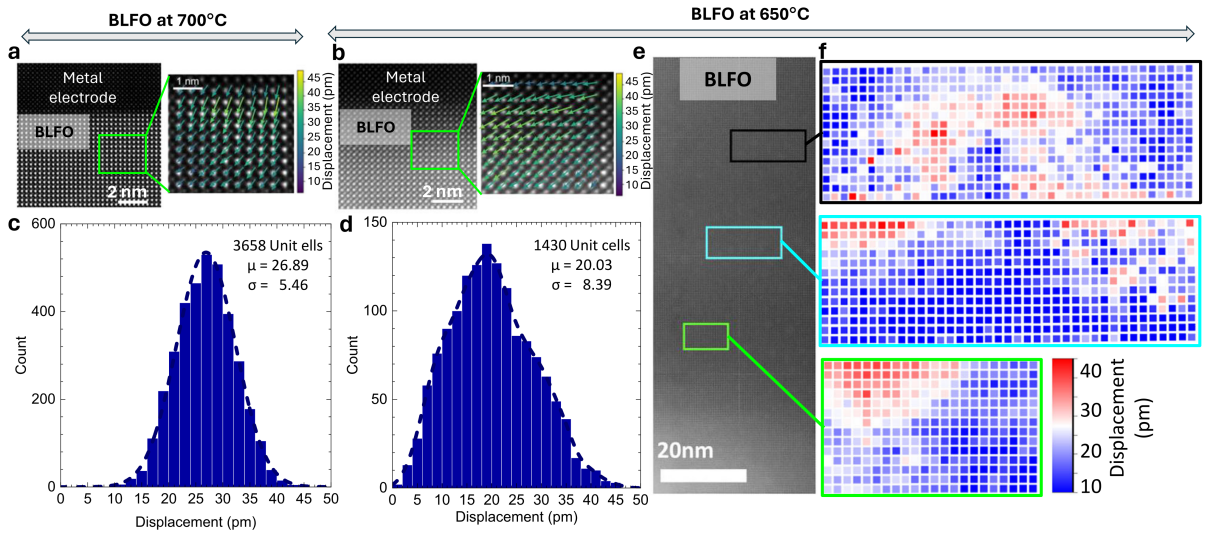

Figure 4.4: **Atomic imaging and polarization mapping.** Polarization displacement vector mapping on BLFO thin film cross-sections deposited at **a)** 700°C and **b)** 450°C. Color arrows indicate the magnitude of polarization as mapped from atomic displacement. Polarization displacement has been calculated using the Fourier-filtered HAADF-STEM images and the histograms include data corresponding to 3658 and 1430 unit cells of BLFO, respectively, for the sample deposited at **c)** 700°C and **d)** 450°C. While **c** closely follows a Gaussian distribution, **d** shows a non-normal distribution of polarization displacement vectors. **e)** HAADF-STEM image of BLFO grown on BPBO at 450°C. **f)** The corresponding polarization displacement distribution maps across the area of **e** at different places. The patches of red are indicative of short-range order, but weak long-range order.

structural distortion[91–93]. The Fourier-filtered HAADF-STEM images were analyzed using CalAtom software to extract the atomic position of Bi/LA and Fe ions by multiple-ellipse fitting[94]. The Fe displacement vector **D** in each unit cell was calculating with the following formula:

$$\mathbf{D} = \mathbf{r}_{\mathrm{Fe}} - \frac{\mathbf{r}_1 + \mathbf{r}_2 + \mathbf{r}_3 + \mathbf{r}_4}{4} \tag{4.2}$$

where $\mathbf{r}_{\mathrm{Fe}}$ is the position vector of the Fe column, and $\mathbf{r}_{1-4}$ are the positions of the four closest Bi/La neighbors in each unit cell. Quantitatively, the polarization displacement vector analysis is shown in Fig. 4.4. Atomic images and **D** maps of high-temperature and low-temperature deposited BLFO films reveal the polarization distribution among the unit cells.

The displacement vector distribution profiles at three different places in the BLFO in the bismuthate heterostructure, shown in Fig. 4.4f, indicate a non-uniform polarization displacement in different regions. Although the material is still polar, the degree of long-range order within the BLFO layer is degraded. In contrast, the high-temperature BLFO shows uniform polarization displacement distributions consistent with previous reports[71]. This indicates a high degree of long-range ferroelectric order. This issue of long-range order of the polar state in such robust ferroelectrics has received very little attention, in contrast to the extremely well-studied short-range order in relaxor ferroelectrics[93, 95, 96].

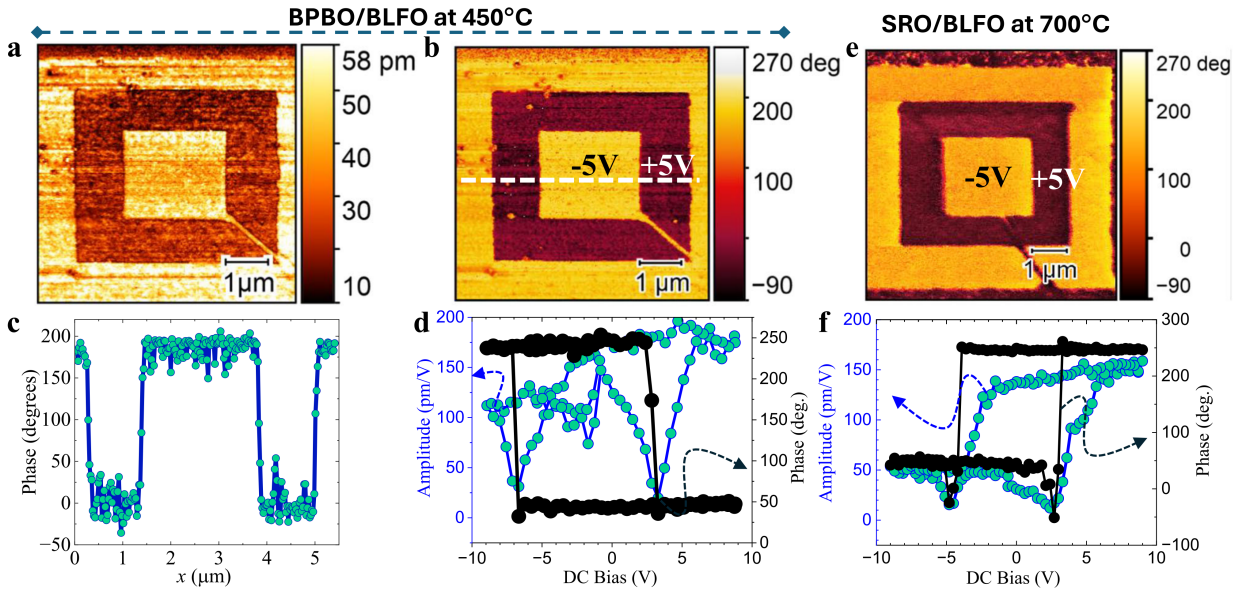

Figure 4.6: **Piezoelectric response.** **a)** Piezoelectric amplitude and **b)** piezoresponse force microscopy (PFM) image of BPBO/BLFO. Box-in-box mapping is done with ±5 V electric field. **c)** Line scan profile of the BLFO phase of **b**. **d)** Point-contact amplitude and piezoelectric hysteresis. **e),f)** PFM and hysteresis data for SRO/BLFO deposited at 700°C. Both sample loops were recorded at a frequency of 0.83 Hz and 1V AC drive amplitude with ±9 V DC scan voltage.

Ferroelectric Behavior

In order to probe how the degree of long-range structural order impacts the macroscopic polar responses, we first demonstrate the piezoelectric and ferroelectric behaviour in the BLFO films using piezoresponse force microscopy (PFM). To do this, films were deposited without the top BPBO electrode, and the PFM tip is used as the "top electrode" for application of localized electric field. To simultaneously demonstrate the piezoelectric and ferroelectric nature, an out-of-pane "box-in-box" pattern is written with the PFM tip by applying −5 V to a 7μm square, followed by +5 V to a 5μm square, and finally −5 V to a 2.5μm square, all squares being concentric. The resulting domain structures are then imaged using PFM (Fig. 4.5 and 4.6). The sharp contrast in the images as well as the clear 180° phase switch in the line profile indicate consistent switching between two stable out-of-plane directions. Furthermore, the retention of the written "box-in-box" pattern is stable after 20 hours, and we expect longer duration stability.

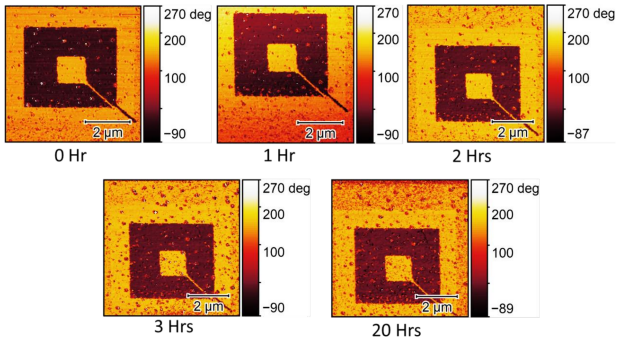

Figure 4.5: **Time resolved piezo-force microscopy.** The ferroelectric polarization of a BLFO thin film deposited on BPBO at 450°C is stable up to 20 hours, and longer stability is expected due to the unchanging phase contrast.

We proceed to quantitatively investigate the ferroelectric properties of our heterostructures by fabricating macroscopic capacitors. To fabricate the capacitors, 5nm of Pt is deposited on top of the trilayer for good electrical contact, and an optical mask consisting of an array of circles is used to make a photoresistive hard mask. We then use an ion mill equipped with a Secondary ion mass spectrometer (SIMS, Hiden Analytical) to etch away the Pt and BPBO/SRO layers, stopping on the BLFO layer. The photoresist is then stripped. The resistance of our BPBO electrodes is ∼1.2 kΩ/square, and the vertical resistance of the whole capacitor stack is ∼ 40MΩ.

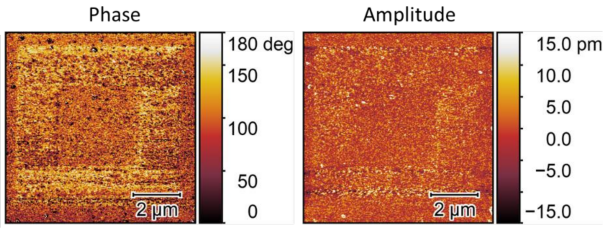

Figure 4.7: **SRO/BLFO deposited at 450°C.** The PFM recorded for this sample was done in the same way as in Figure 4.6, but here we do not see any phase reversal in the polarization contrast, which is expected as no ferroelectric hysteresis loops are visible for the SRO/BLFO/SRO sample deposited at 450°C (Fig. 4.8a). The weak contrast that is visible is from surface perturbations caused by the tip with an applied voltage, not from ferroelectric polarization.

Polarization-electric field hysteresis loops (Fig. 4.8) demonstrate robust ferroelectricity in the 450°C bismuthate heterostructures (heterostructure I) and the 700°C SRO heterostructures (heterostructure II), but not in the 450°C SRO heterostructures (heterostructure III). Two important differences between heterostructures I and II include the absolute magnitude of the switched polarization and the coercive voltage. Heterostructure I has significantly lower remnant polarization and significantly higher coercive field than heterostructure II. The current-electric field measurements (Fig. 4.8c) show that heterostructure II is more leaky than heterostructure I.

Discussion

It is counterintuitive that the remnant polarization of is smaller but the coercive field is larger in heterostructure I compared to heterostructure II. Combined with the HAADF-STEM analysis, we find that the lower degree of long-range order is responsible for both effects: it reduces the spontaneous polarization but also makes switching the polar state more energetically costly, which is consistent with previous results[92, 93]. Moreover, the resistance of the BPBO (1.2 kΩ/sq.) is larger than that of the SRO (0.58 kΩ/sq.), which contributes an additional source of voltage drop across the capacitor that enhances the coercive fields[97].

Another factor contributing to differences in ferroelectric behavior is the concentration electrically inhomogeneous microstructures, such as vacancies, interstitials, and other defects. Such defects can lead to a small, local electric field in the material, fixed by the position of the defect. Some defects, such as dislocations, stretch along one dimension and may provide a conductive channel for leakage currents[98], however 0-dimensional defects would not conduct currents. We measure these leakage currents, and the results are shown in Fig. 4.8c. The higher dielectric constant in heterostructure I (Fig. 4.8b) paired with the lower leakage current in heterostructure I indicates that there is a higher concentration of non-conducting defects in heterostructure I, which will increase the dielectric constant but reduce the leakage. Typically, dislocations and vacancies can serve as channels for leakage currents

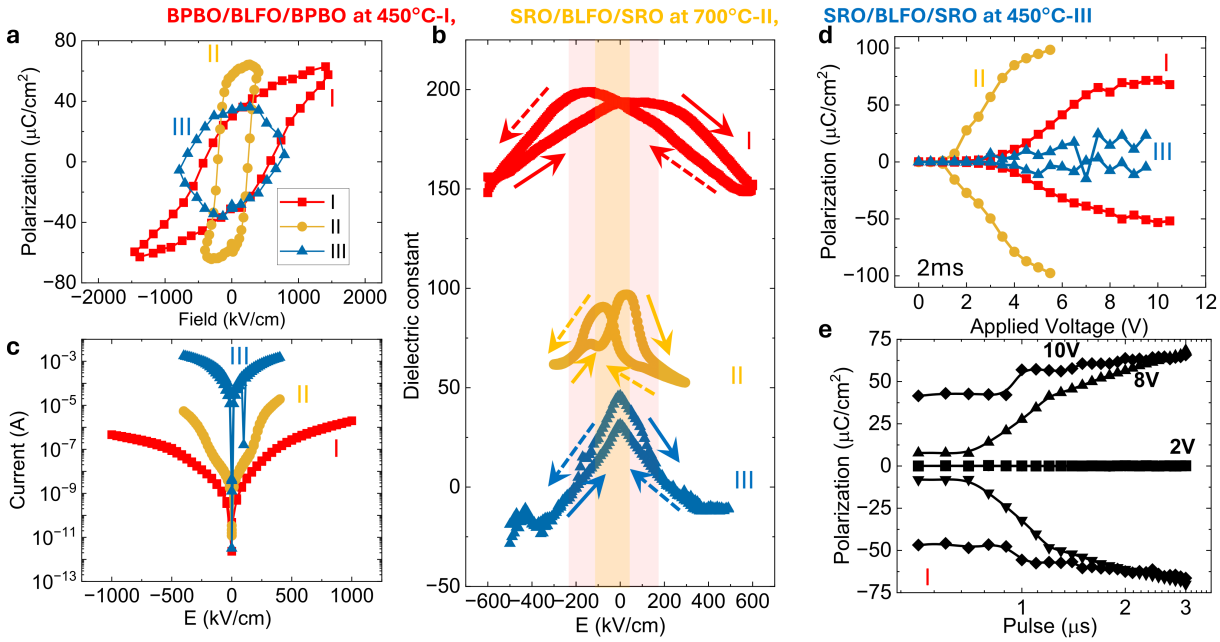

Figure 4.8: **Ferroelectric response.** **a)** Polarization as a function of electric field for the samples BPBO/BLFO/BPBO deposited at 450°C (sample I), SRO/BLFO/SRO deposited at 700°C (sample II), and SRO/BLFO/SRO deposited at 450°C (sample III). **b)** Dielectric constant and **c)** leakage current as a function of electric field across the capacitors in the heterostructures. **d)** Pulsed switched polarization as a function of varying voltage at a fixed 2ms pulse width. **e)** Voltage dependence of switched polarization by varying the pulse widths in sample I.

in ferroelectrics, but some electrically inhomogeneous microstructures can pin domain walls and increase the coercive field without being conductive. A lower degree of long-range order is consistent with a higher concentration of such microstructure defects.

Conclusion

In summary, we demonstrate a method for growing BLFO at low temperatures on metallic BPBO electrodes. Despite a 9% lattice mismatch, the oriented growth of the ferroelectric phase is achieved at temperatures as low as 450°C, due to the high quality low-temperature epitaxial BPBO. Piezoelectric force microscopy and measurements on macroscopic capacitors demonstrate ferroelectric properties comparable to high-temperature BLFO grown on standard SRO electrodes. We note that exiting work on single-crystal BLFO and BFO is done at deposition temperatures that are significantly higher and thus incompatible with CMOS device integration[76], and therefore this work presents a new avenue for integration of the multiferroic in CMOS devices. We also show that the low-temperature BLFO has a significantly reduced long-range polarization ordering which results in the lower remnant polarization. Due to the conducting nature of BPBO and sharp interfaces created by grapho-epitaxy, the electric and ferroelectric properties are consistent even in the full BPBO/BLFO/BPBO stack deposited at a record low temperature. Our study provides a new pathway to control the temperature of multiferroic thin-film growth as well as the polarization ordering, which may be important for a range of new BFO-based applications.

Part III
Magnons in Multiferroics

Magnons (quantizations of spin waves) have become the ideal carriers of information in future spin-based technologies [99–102]. In the push to design next-generation memory and logic technologies that utilize spin, antiferromagnets are particularly attractive due to their stability against external magnetic fields and large magnon propagation group velocities [103–105], and magnons can carry information through insulating antiferromagnets. While manipulating the magnetic order parameter of most antiferromagnets is impractical in device applications, the antiferromagnetic order of multiferroic bismuth ferrite, $BiFeO_3$ (BFO), is switchable by an electric field due to the magnetoelectric coupling between ferroelectricity and antiferromagnetism [9, 106–110].

Transforming between magnetic and electric fields can be done with magnetic induction via electric currents[111, 112]. However, for applications such as manipulating the magnetization of nanoscale magnets in integrated memory and logic, the conventional Oersted field approach has been proven to be energy-inefficient and impractical[113]. To address the imperative of low-energy consumption in nonvolatile magnetic memory and logic, a promising new avenue has emerged – direct voltage control of magnetism [114–119]. Recent proposals use the magnetoelectric coupling inherent in some multiferroics, which allows for direct electric field control of the magnetic state in such a material [106, 117].

A notable example of this innovation is the magneto-electric spin-orbit (MESO) logic device structure, proposed as an inherently non-volatile substitute for complementary metal-oxide-semiconductor (CMOS) devices in integrated logic-in-memory applications [9, 120]. To this end, $BiFeO_3$, possessing strong antiferromagnetic magnetoelectric coupling [106, 108, 121], is considered a desirable material for MESO-type devices. Additionally, with its antiferromagnetic character, the material is robust against external magnetic fields and possesses potentially faster switching dynamics than ferromagnets. Recently, $BiFeO_3$ has also been shown to be an efficient system for demonstrating switchable magnon spin currents [69, 122]. This electric field switchable electro-magnon coupling allows for a simplified version of the MESO device i.e., the antiferromagnetic state is directly read out using the spin-orbit metal in direct contact with the antiferromagnetic layer, without an intermediate ferromagnetic layer. In this context, there have been attempts to realize antiferromagnetic state readout using the electrical control of magnon transport in $BiFeO_3$ [14].

To date, magnon mediated spin transport in multiferroics such as $BiFeO_3$ is still a relatively new field of research, and there are many unanswered questions about the magnon dynamics in the complicated magnetic texture of $BiFeO_3$. The following chapters focus on the physics of magnons in $BiFeO_3$ and related materials, and explore magnon-mediated spin transport through the spin cycloid as well as electric field control of spin transport. Transport measurements were performed using 4-terminal devices where 2 terminals are used to inject spin current from an injector wire and 2 terminals are used to detect voltage along a detector wire. These wires are parallel, and using one terminal from each wire we can apply an electric field across the gap for polarization control. Switching between terminal configurations – to apply an electric field, or measure temperature gradients along different

directions – is done with a Keithley 7001 switchbox. The voltage is measured using an SR830 lock-in amplifier and locking to the second (in the case of thermally excited magnons) or first (in the case of spin Hall excited magnons) harmonic of the excitation current. The excitation current is an AC signal at 7 Hz applied with a Keithley 6221. Schematics can be found in Figures 5.8a, 6.7a, and 7.2a.

Using python scripts to control the switchbox and other electronics, we are able to run magnon experiments repeatably and with high throughput. This greatly enhances the resolution of our electric-field controlled magnon experiments, and has allowed us to make several advances in multiferroic magnonics. In Chapter 5, we explore the magnon anisotropy of magnons traveling throughout the spin-cycloid of $BiFeO_3$, and in Chapter 6 we study magnon transport through single-ferroelectric-domain spin cycloids. Combining these results in Chapter 7, we develop a phenomenological model to predict characteristics of the magnon transport based on the symmetries of the magnetic texture. This approach can be extended generally to electric-field-controlled magnon propagation in all multiferroics, and will serve as an important tool for understanding spin currents in future magnon transport studies.

5 Anisotropy of Magnon Transport in $BiFeO_3$

As previously discussed, BFO is a well-studied antiferromagnetic oxide due to the strong coupling between polarization (ferroelectricity) and magnetic (antiferromagnetism) order at room temperature, enabling all-electric-field control of magnetization [106, 108–110]. Due to this interaction, BFO has garnered interest in the field of spintronics, especially with recent observations showing that electric-field control of spin transport is possible [14]. The fundamental magnetic order in BFO consists of G-type antiferromagnetism which is modulated by broken symmetries stemming from the polarization and from antiferrodistortive FeO_6 octahedral rotations. These phenomena give rise to a long-period ($\lambda \approx 65$ nm) spin cycloid [123]. In its equilibrium structure, when the polarization $\mathbf{P}$ is parallel to [111][124], this antiferromagnetic cycloid propagates along three symmetry-equivalent directions: $\mathbf{k}_1$ ($[\bar{1}10]$), $\mathbf{k}_2$ ($[\bar{1}01]$), and $\mathbf{k}_3$ ($[0\bar{1}1]$), with Fe atomic moments rotating in the $(11\bar{2})$, $(1\bar{2}1)$, and $(\bar{2}11)$ planes respectively [125]. The antiferromagnetic cycloid is then further perturbed by the Dzyaloshinskii-Moriya interaction (DMI), canting the moments slightly out of the $\mathbf{P}$-$\mathbf{k}$ plane and resulting in a spin-density wave with the same period as the antiferromagnetic cycloid [126, 127]. This intrinsic, periodic magnetic structure in BFO can be modulated by an electric field, a capability attributed to its strong magnetoelectric coupling [128, 129]. Despite its fundamental nature, the behavior of spin propagation within such a complex spin structure remains not fully understood. This gap in knowledge suggests that the cycloid's periodicity could have significant, yet unexplored, effects on magnon dispersion.

The intimate coupling between magnetic order and ferroelectric polarization in BFO allows for the use of its ferroelectric structure as a tool to design periodic magnetic structures facilitating spin-wave transport. Previous studies have shown that the ferroelectric domain structure of thin-film BFO can be controlled using electrostatics and the epitaxial arrays of either 71° or 109° domains [66]. This directly influences the magnetic structure [107, 130]. Our current study demonstrates that by engineering these phenomena through the boundary conditions imposed by electrostatics and lattice-mismatch strain, we can effectively guide the ferroelectric domain structure to modulate the spin cycloid. This manipulation results in the creation of a long-range, intrinsic, quasi-1D-ordered lattice. Such a lattice structure creates a gap in the magnon dispersion and introduces a significant spin-transport anisotropy, which is further tunable with an electric field.

Multiferroic Structure

To control the ferroelectric and magnetic structure of BFO, we synthesize epitaxial thin films on both $DyScO_3$ (DSO, ∼0.4% compressive strain) and $TbScO_3$ (TSO, ∼0% strain) substrates using both molecular-beam epitaxy (MBE) and pulsed laser deposition (PLD). MBE films were grown by reactive MBE in a VEECO GEN10 system using a mixture of 80% ozone (distilled) and 20% oxygen. Elemental sources of bismuth and iron were used at fluxes of 1.5×10^{14} and 2×10^{13} atoms/cm^{2}s respectively. All films were grown at a substrate temperature of 675°C and chamber pressure of 5×10^{-6} Torr. PLD samples were deposited using a 248 nm KrF laser with ∼ 1.5 J/cm^2 at 700°C and 90 mTorr O_2. X-ray diffraction (XRD) and reciprocal space mapping (RSM) were performed on a PANalytical Xpert3 diffractometer (Fig. 5.1), and the films are confirmed to be ∼100 nm thick and of excellent crystalline quality as

evidenced by the thickness fringes.

In addition to slightly different epitaxial strain states from the choice of substrate, these systems are chosen to engineer films with different ferroelectric domain structures. These films host characteristic stripe-like 71° ferroelastic domains on DSO and 109° ferroelastic domains on TSO [132]. Piezoresponse

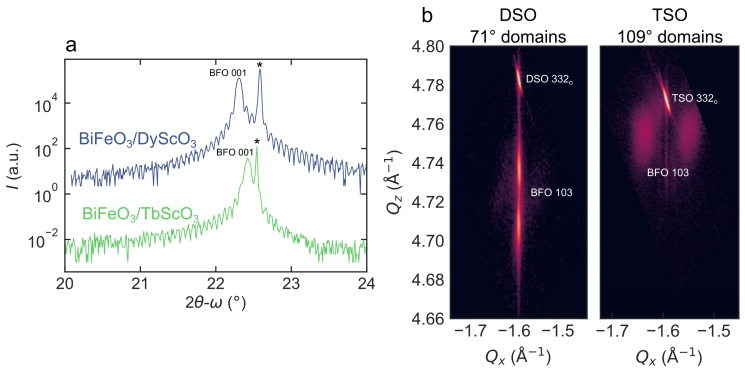

Figure 5.1: **X-ray diffraction. a)** $2\theta-\omega$ linescans of the two samples with thickness fringes. **b)** Reciprocal space maps (RSM) of the 332_O diffraction peak. Differences are due to different configurations of rhombohedral BFO unit cells in different domain configurations [131].

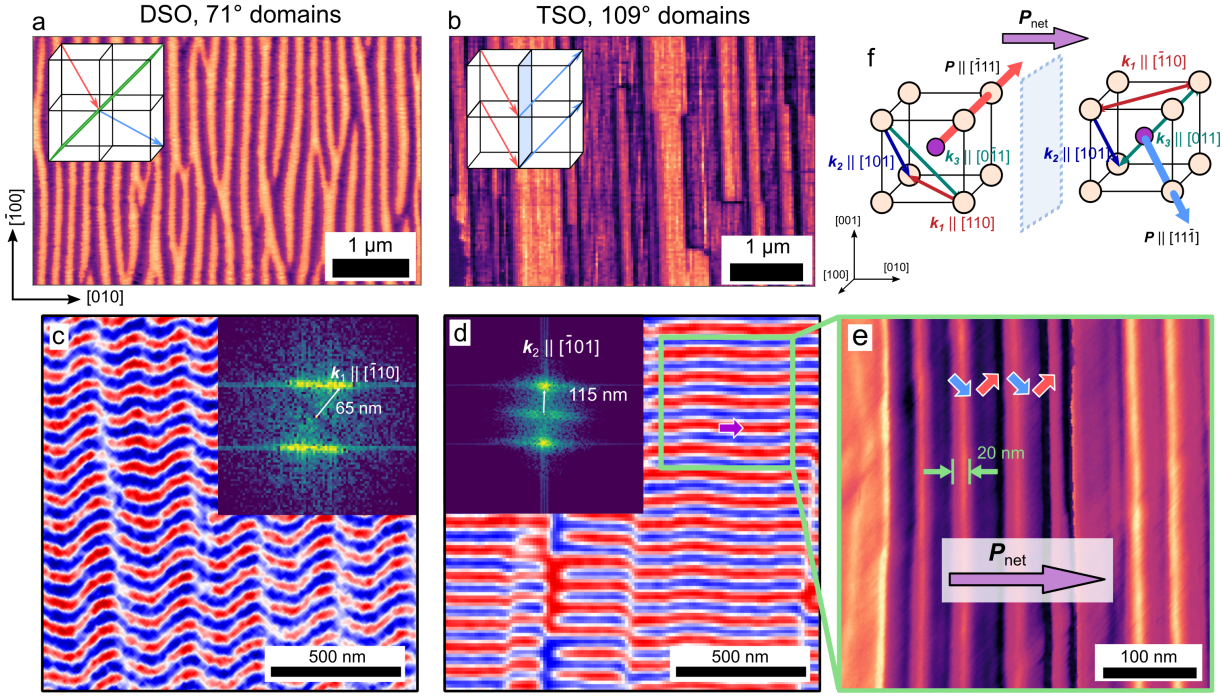

Figure 5.2: **1D ordered lattice.** In the two BFO variants, the ferroelectric domains are arranged into ground states containing **a)** 71° and **b)** 109° ferroelastic domain walls. Insets depict the two types of domain walls and their corresponding polarizations in the BFO unit cell. In films deposited on DSO substrates, the cycloid prefers the $\mathbf{k}_1$ variant, which results in **c)** a chevron-like pattern across the ferroelectric domains. **d)** For films on TSO, however, the domain structure allows selection of the other symmetry allowed axis, in this case $\mathbf{k}_2$. Corresponding Fourier transforms are shown as insets revealing the period and symmetry of the magnetic structures. **e)** Piezoforce microscopy image-zoom of the area shown in green, where the cycloid is unperturbed by the fine, 10-30nm ferroelastic domain walls. **f)** This occurs due to the symmetry of $\mathbf{k}_2$ across the 109° domain wall, where the directionality of the cycloid is preserved with the fixed net polarization P_{net} imposed by the ferroelectric domains.

force microscopy (PFM) images (Fig. 5.2a,b) demonstrate the two-variant strip patterns along [100]. The nanoscale magnetic structures of these different strain and domain configuration are then investigated in real space using scanning nitrogen-vacancy (NV) magnetometry [107, 124, 129, 133] on a Qnami ProteusQ system with a parabolic Quantilever MX+ diamond cantilever.

In films deposited on DSO (Fig. 5.2c), NV magnetometry shows a chevron-like magnetic texture of the stray magnetic field, revealing a $\mathbf{k}_1$-oriented cycloid that switches direction with the change of the $\mathbf{P}$ directions across the 71° ferroelastic domain walls. This is consistent with previous reports [129] and is a result of the magnetoelastic anisotropy from the substrate lattice mismatch [130]. Strikingly, in the sample deposited on TSO (Fig. 5.2d), only a single $\mathbf{k}$ variant of the cycloid is observed, projected along [100]. The longer period of these oscillations indicates that this corresponds to a $\mathbf{k}_2$, [101] axis of the epitaxial strain of TSO. Importantly, this variant of the cycloid even persists across the approximately 20-30 nm wide 109° ferroelectric domains and extends over long distances (up to at least 20μm). This results in the formation of a quasi-long-range, 1D magnonic crystal, as illustrated in Fig. 5.2d.

This propagation of the $\mathbf{k}_2$ cycloid variant across ferroelectric domains can be understood through the symmetry of the 109° ferroelastic domain walls. Starting with the 71° domains in films on DSO substrates, the in-plane $\mathbf{k}_1$ directions are strongly magnetoelastically preferred. At the ferroelectric domain walls, where polarization $\mathbf{P}$ rotates from $[\bar{1}11]$ to [111], the cycloid wave vector directions must be shifted, for example, from [110] to $[\bar{1}10]$, to ensure the perpendicular relation $\mathbf{k}_1 \perp \mathbf{P}$. This shift leads to a chevron-like pattern being favored as an equilibrium state. In contrast, in films on TSO substrates, the magnetoelastic energy is lowered, making the $\mathbf{k}_2$ and $\mathbf{k}_3$ variants closer in energy. Furthermore, considering the 109° domain walls in the films on TSO substrates, assuming $\mathbf{k}_2$ is now an allowed direction, the propagation axis would not need to alter with the polarization change. This is because [101] is perpendicular to both $[\bar{1}11]$ and $[11\bar{1}]$ (Fig. 5.2f), making $\mathbf{k}_2$ also a symmetry-favored equilibrium in this configuration. Consequently, $\mathbf{k}_2$ emerges as the globally preferred equilibrium state, leading to a single cycloid variant that persists across the 109° ferroelastic domain walls, despite their $\sim 20-30$ nm period [131].

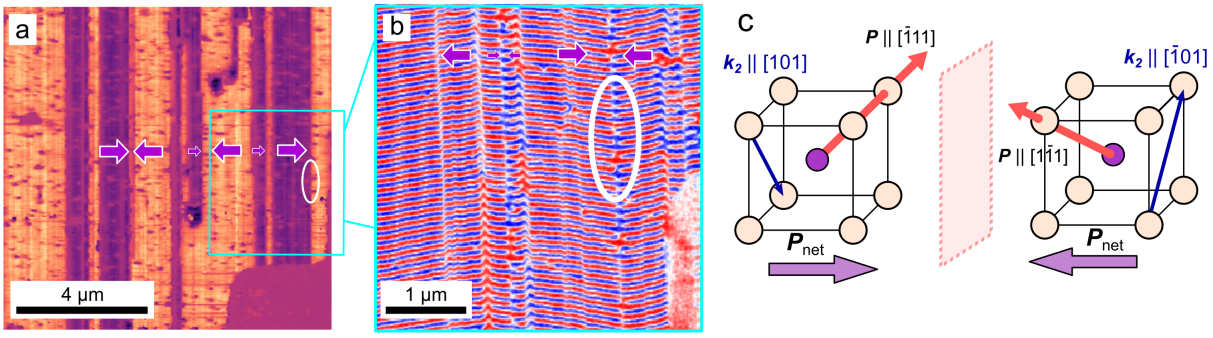

Figure 5.3: **Antiphase boundaries. a)** PFM showing the two families of superdomains with antiparallel net in-plane polarization components. **b)** NV imaging of the same region showing the imprint of the superdomains on the magnetic texture. **c)** A schematic showing the the two different $\mathbf{k}_2$ across the domain wall.

Furthermore in the 109° domain samples, there is a hierarchy of domains. Superimposed on the fine-scale 109° domain ensemble with a spacing of 20-30nm, families of domains with net antiparallel in-plane polarization components are also observed. Comparing the ferroelectric polarization from PFM with the NV data (Fig. 5.3), we observe discontinuities in the 1-D cycloid lattice that correlate with the family domain walls. Though $\mathbf{k}_2$ does not change across the fine-scale (20-30nm) domain walls, it does change (e.g. $\mathbf{k}_2 = [101]$ to $\mathbf{k}_2' = [\bar{1}01]$) across the large domains with a different in-plane polarization. Though $\mathbf{k}_2$ and $\mathbf{k}_2'$ are orthogonal to each other, the in-plane component of the cycloid does not change, giving the appearance of discontinuities (akin to antiphase boundaries) when projected in-plane. When the material is electrically poled, these domain walls are annealed out of the sample.

Magnon Transport

To test spin transport with respect to the directions defined by the quasi-1D spin-spiral lattice, we fabricated test structures that are schematically shown in Figure 5.6a. These structures consist of source and detector wires aligned both parallel and perpendicular to $\mathbf{k}$. The magnon-induced voltage signal in these structures is compared along multiple direc-

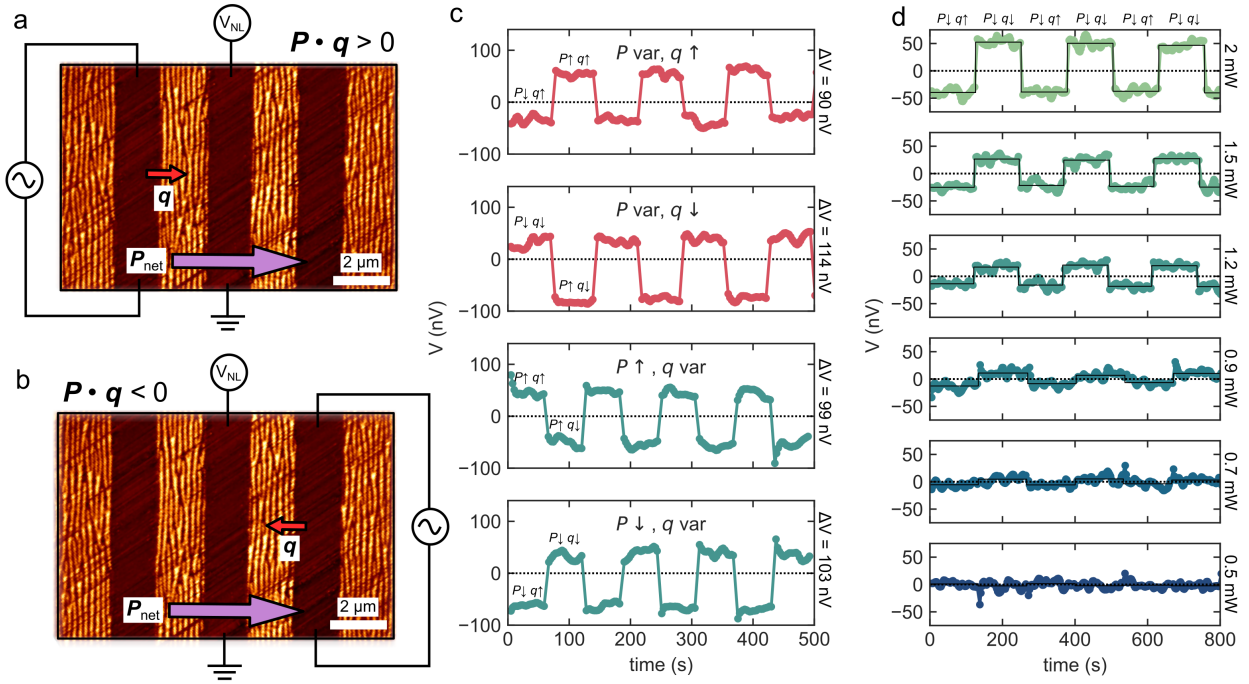

Figure 5.4: **Comparison of measurement schemes. a),b)** PFM and schematics of three-wire device for magnon-driven non-local voltage without an external electric field. The non-local voltage detector is fixed at the center and current is injected left or right to create two different $\mathbf{q}$ while $\mathbf{P}$ remains invariant. **c)** Plots showing nonlocal signal in different configurations, switching $\mathbf{P}$ under constant $\mathbf{q}$ and vice versa. In all four permutations, $\Delta V \approx 100$ nV and the signs of the same states (e.g. $\mathbf{P} \downarrow \mathbf{q} \uparrow$) are consistent. This ± 10 nV may be due to intrinsic device differences, but should be mitigated when averaging across devices. **d)** Power dependence of fixed $\mathbf{P}$ variable $\mathbf{q}$ measurements, showing the appropriate scaling and consistency of the sign.

tions with respect to **k** to show anisotropy, as well as in both the quasi-1D and chevron-like structures (Fig. 5.6b,c). First, considering thermally excited magnons in a two-wire scheme, a current in the source wire is used to create a temperature gradient (∇T) in the device, causing thermally excited spin waves to propagate $\mathbf{q} \parallel -\nabla T$, where **q** is the magnon propagation direction, via the spin Seebeck effect [14]. These magnons are then sensed in the detector wire through the inverse spin Hall effect (ISHE), which converts the spin current to a DC voltage, $V_{\mathrm{NL},1\omega}$ [10, 134]. To preserve the ferroelectric domains, we performed this measurement again by reversing the directionality of the thermal transport with respect to the in-plane polarization. The magnitude of this voltage is reported as the difference between these two measurement configurations, where the propagation direction **q** from the thermal gradient ∇T is switched 180° and the ferroelectric polarization **P** remains fixed.

This was chosen due to the response of domains to an electric field parallel to the domain wall, which can lead to reconfiguration of the domain structure. The application of an electric field parallel to two-variant domain walls transforms the domain structure into 71° domains running perpendicular to the electric field. This in turn changes the magnetic structure of the spin cycloid, making determination of the native anisotropy ⊥ and ∥ to the spin cycloid

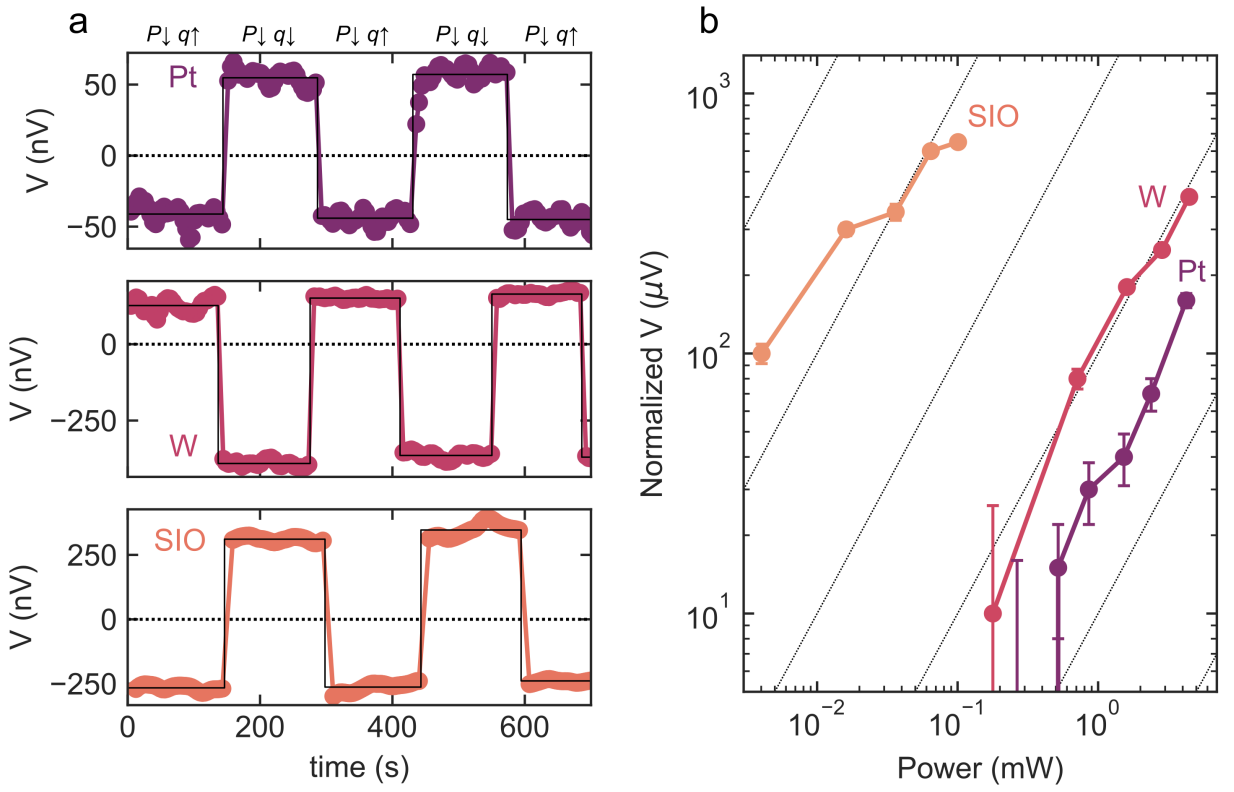

Figure 5.5: **Material and power dependence. a)** The thermally-driven non-local conductivity changes with the sign and magnitude of the spin Hall angle of the detector wire material (Pt, W, and SIO), demonstrating its magnetic origin. Symbols are the raw data and solid lines represent the time average. **P** and **q** are the polarization and the magnon-propagation direction, respectively. **b)** The output voltage also scales with the magnitude of the spin Hall angle of the detector material. The diagonal lines correspond to orders of magnitude.

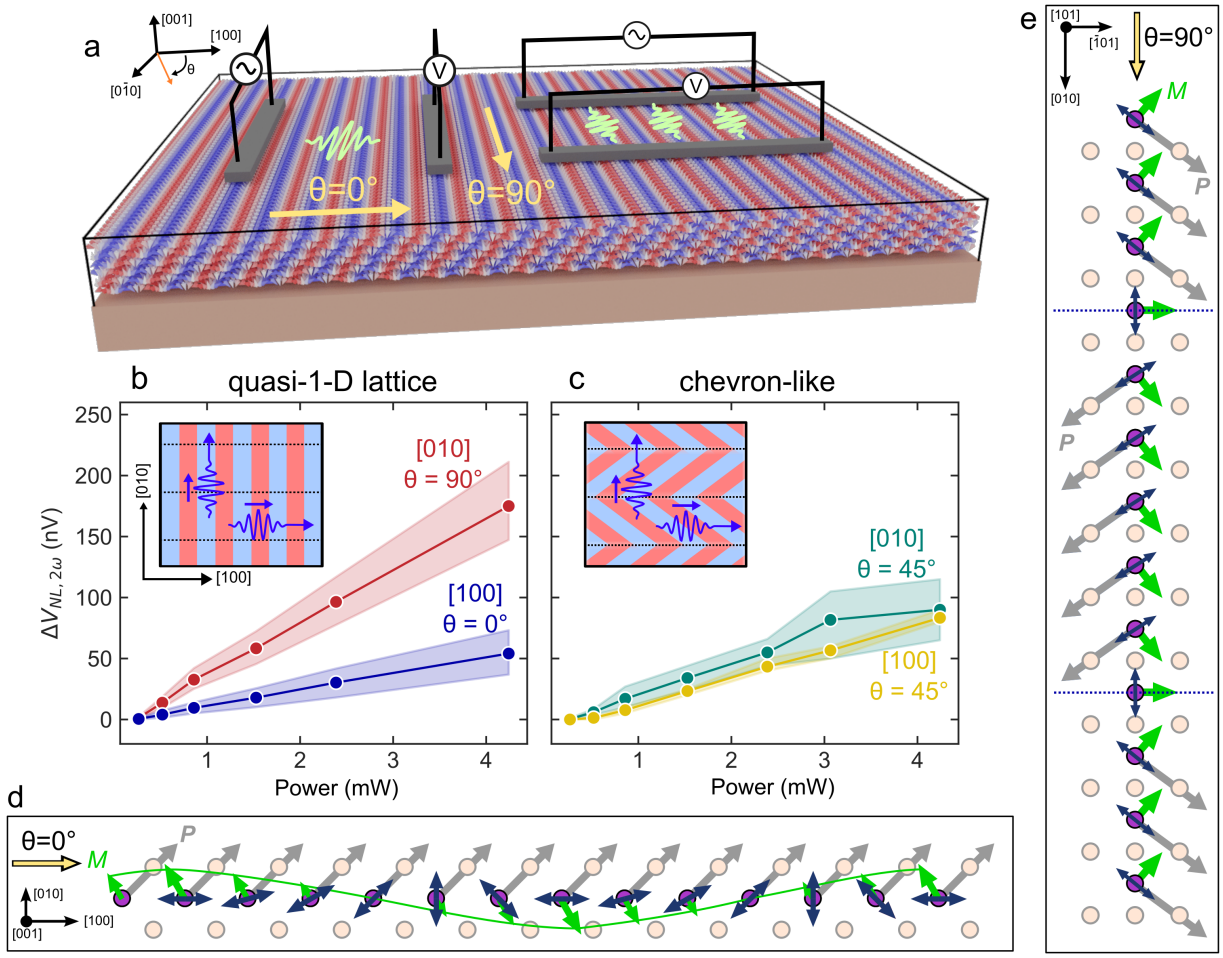

Figure 5.6: **Spin wave anisotropy. a)** Schematic of the sample geometry of the test structures $\parallel$ ($\theta = 0°$) and $\perp$ ($\theta = 90°$) to **k**. **b)** In the quasi-1D lattice of 109° domains, there is high conductivity along the ferromagnetically coupled direction [010], and low conductivity along **k** = [100]. **c)** Conversely, for the 71° domain scenario, the cycloid and thus conductivity display no distinct anisotropy between the $\theta = 0°$ and $\theta = 90°$ directions. The cycloid in **b** can be viewed **d)** along the direction parallel to [010] ($\theta = 0°$) or **e)** along the direction parallel to [100] ($\theta = 90°$).

propagation direction **k** impossible. In samples where the electric field does not perturb the domain structure (**E** is perpendicular to the domain walls), we find that the difference in V_{NL} for the two polarization states is equivalent to the difference ΔV_{NL} from comparing the two configurations (Figure 5.4). We note that while small differences in the heater and detector wire will lead to discrepancies in the measurements, averaging ΔV_{NL} across different devices negates this asymmetry.

Confirmation that the signal is magnetic in origin comes from testing with different detector materials (Fig. 5.5). For example, changing the detector wire from Pt to W (with a larger, opposite-signed spin-Hall angle compared to Pt) reverses the sign of $\Delta V_{NL,2\omega}$. Similarly, moving to a material with a much larger spin-Hall angle, such as $SrIrO_3$ (SIO) [20], proportionally increases the ISHE voltage.

In films featuring the quasi-1D ordered cycloid lattice, a strong anisotropy is observed

with respect to the directions $\mathbf{q} \parallel \mathbf{k}$ and $\mathbf{q} \perp \mathbf{k}$. We define θ here as the angle between $\mathbf{q}$ and $\mathbf{k}$. Notably, the ISHE voltage signal, indicative of spin wave conductivity, is approximately three times larger when $\theta = 90°$ than when $\theta = 0°$. In contrast, samples with the alternating chevron-like structure, characterized by $\mathbf{k}_{net} = \sum \mathbf{k} = 0$, exhibit minimal spin transport anisotropy (Figure 5.6c). Additionally, in the chevron-like structures, where locally $\theta = 45°$, $\Delta V_{NL,2\omega}$ lies between the values at $\theta = 90°$ and $0°$ seen in the 1D ordered system. This behavior can be initially understood by examining the nanoscopic magnetic spin structure within the cycloid as described schematically in Figure 5.6d,e. In a line cut $\perp \mathbf{k}$, the spins are modulated by the presence of the 109° ferroelastic domain walls, but possess a persistent net magnetization component, illustrated in Figure 5.6e. In contrast, oriented parallel to $\mathbf{k}$, the spins rotate by a full 2π over the period of the cycloid (65 nm, Fig. 5.6d).

Phase Field Simulations and Model Hamiltonian Calculations

To further evaluate the physics associated with transport in the quasi-1D structure, we turn to both mesoscale phase-field simulations and model Hamiltonian calculations of spin transport $\parallel \mathbf{k}$ and $\perp \mathbf{k}$. From the phase-field simulations, which are outlined in Appendix C, we observe an anisotropy characterized by reduced spin-wave conductivity along the $\mathbf{q} \parallel \mathbf{k}$ direction, compared to the $\mathbf{q} \perp \mathbf{k}$ direction. Simulations are carried out by imposing a cycloidal magnetic ground state comparable to those observed experimentally and by initiating spin waves within a specified frequency range at one edge of the sample. The efficiency of these waves is quantified by comparing the magnetization precession at the point of origin and a defined distance from the source. In scenarios where $\mathbf{q} \perp \mathbf{k}$, the initial waveform exhibits negligible damping even at a distance equivalent to 10λ (Fig. 5.7a). When $\mathbf{q} \parallel \mathbf{k}$ however, the spin wave exhibits significant attenuation over the same distance.

This is evident in both the spectrum of the magnetization precession angle and its integrated energy across the spectrum, which is shown to be influenced by the magnitude of the anisotropy within the cycloid. As illustrated in Figure 5.7b, a scenario with an anisotropy of $K = 100\text{kJ/m}^3$ leads to approximately 50% damping in spin-wave-energy magnitude over the same length scale. This transport efficiency can then be studied as a function of K to compare with previous calculations and experimental results, defining a reasonable window for the value of K. The precession angles corresponding to other values of K are shown in Appendix C.

At the microscopic scale, analytical calculations of the momentum-dependent magnon dispersion in the quasi-1D lattice illustrate the difference in the magnon conduction $\perp \mathbf{k}$ and $\parallel \mathbf{k}$. Analytical solutions for the magnon bands of BFO are based on a continuum Hamiltonian whose density is given by [135]:

$$\mathcal{H} = \mathcal{A}(\nabla \mathbf{n})^2 - \alpha \mathbf{P} \cdot [\mathbf{n}(\nabla \mathbf{n}) + \mathbf{n} \times (\nabla \times \mathbf{n})] - 2\beta M_0 \mathbf{P} \cdot (\mathbf{m} \times \mathbf{n}) - K_u n_c^2 + \lambda \mathbf{m}^2 \quad (5.1)$$

where the first term is the exchange energy, the second and third terms are DMI terms, the fourth term is the anisotropy, and the last term represents the suppression of the net magnetization due to strong antiferromagnetic coupling. The ground-state configuration can then be obtained (Appendix D), showing the well-known anharmonic spin-cycloid structure [135–137]. Solving the time-dependent Euler-Lagrange equation for the small fluctuations,

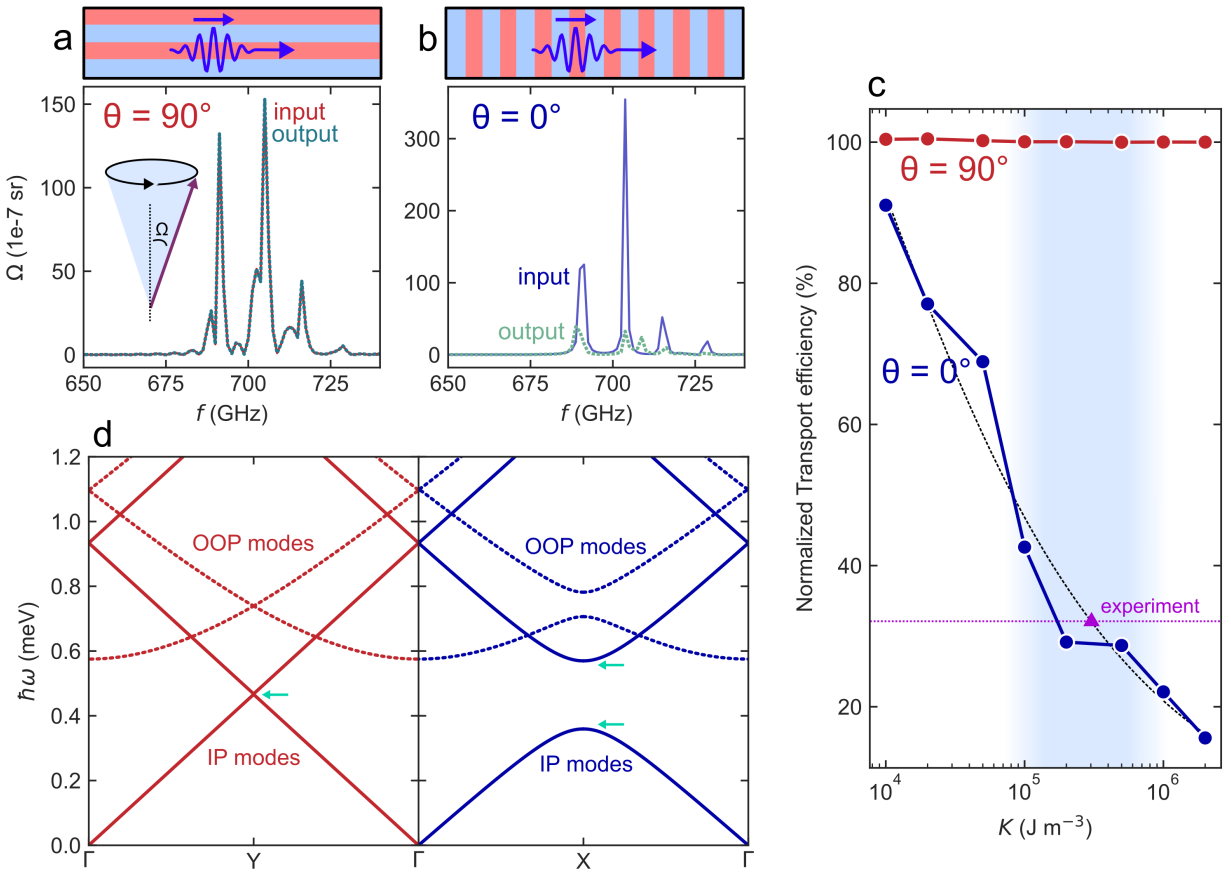

Figure 5.7: **Simulation of magnon conductivity.** Simulations of frequency-dependent magnon power when the spin wave is driven along **q**, either **a)** perpendicular to **k**, or **b)** parallel to **k**, in the quasi-1D lattice. Magnon energy is extracted as $\Omega \times f$, i.e. the product of conical angle Ω of the time-dependent precession of the magnetization in Fourier space, and the frequency f. Input and output spectra are measured at opposite sides of the simulated cell. The integral of this spectra is then reported as a relative conductivity **c)**, simulated as a function of the 1D anisotropy K of the cycloid texture. The shaded region represents a range of energies reported in the literature as well as values matched to the experimental and analytical results presented here. **d)** Calculated magnon dispersion, illustrating the emergence of a gap along the $\mathbf{q} \parallel \mathbf{k}$ direction which leads to reduced spin-wave conductivity. X and Y are the high symmetry points corresponding to the [100] ($\parallel \mathbf{k}$) and [010] ($\perp \mathbf{k}$), respectively.

two spin-wave modes result: 1) An in-plane mode with spin fluctuations within the spin-cycloid plane and 2) an out-of-plane mode with spin fluctuations orthogonal to the spin-cycloid plane. By considering the quasi-2D geometry of the plane-wave-like spin texture of BFO and neglecting the Hamiltonian term $\propto \beta$ that is known to be weak [138], the band structures of in-plane (IP) magnons and out-of-plane (OOP) magnons are obtained analytically (Fig. 5.7d). These solutions show the formation of a gap in the dispersion along the $\mathbf{q} \parallel \mathbf{k}$ direction, due to the periodicity of the magnetic lattice. This gap indicates a lower density of states along this direction, resulting in an anisotropic, lower magnon conductivity.

Magnons excited by the spin-Hall effect

In parallel to measurements of thermally excited magnons, non-local transport measurements have been performed using injected spin currents via the spin-Hall effect (SHE) of the source wire [10] (Figure 5.8a). In this case, the sign of the output signal will correspond directly to the sign of the input signal, rather than only the amplitude of the input, so this nonlocal voltage is measured on the first harmonic of the injector current. While the spin Hall angles of platinum and tungsten are too low to generate an appreciable ISHE signal at the 2 μm electrode spacing, the efficient spin-charge transduction of $SrIrO_3$ (SIO) allows for the detection of the SHE-excited magnon signal [20]. In the device geometry where **q** is perpendicular to the domain walls, where electric fields allow the ferroelastic domain walls to remain largely stationary [14, 108, 133], combining the engineered spin texture with an epitaxial, large SHE oxide can further optimize functionality. This should allow for deterministic switching of the magnetic structure under a continuous rotation of **P** [133].

In test structures using SIO electrodes, we observe a similar anisotropic spin transport, dependent on the underlying magnetic structure. Here, magnons are excited by the SHE and the ferroelectric polarization is switched using an in-plane electric field. Upon switching

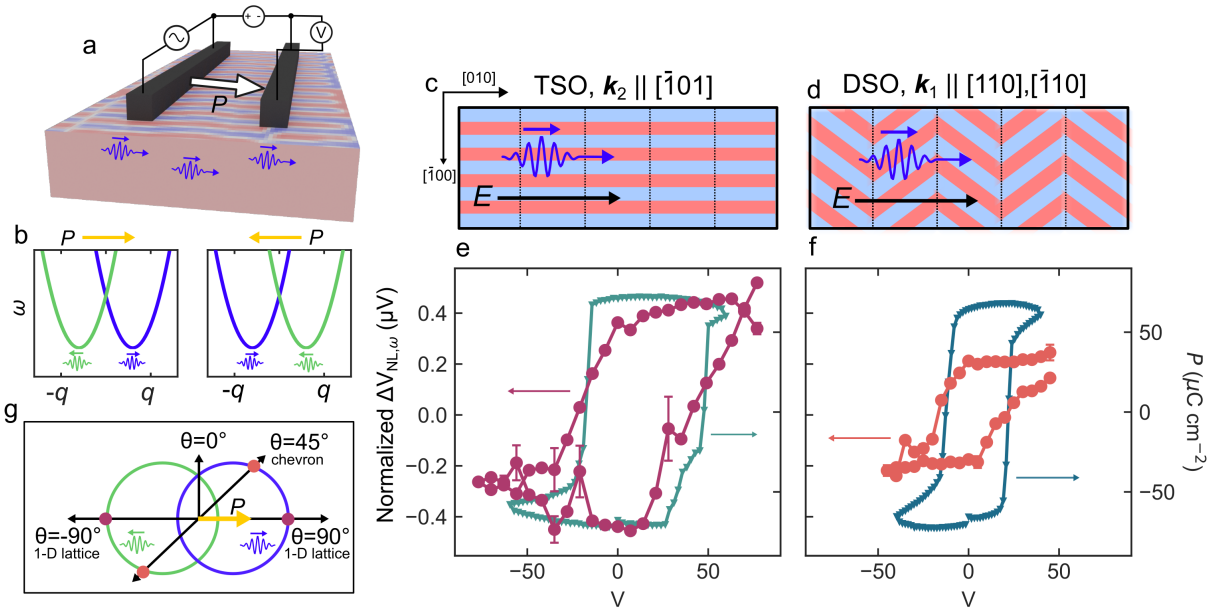

Figure 5.8: **Electric field control of magnon propagation. a)** Schematic showing the non-local device geometry with magnons generated by injection of spin from the source wire. **b)** We hypothesize that the non-reciprocity of the transport is due to a Rashba-like asymmetry of the magnon dispersion emerging from the crystal asymmetry, which is coupled directly to the ferroelectric polarization and DMI. **c),d)** Illustration showing the sense of the cycloid with respect to the device geometry for films deposited on the two different substrates. In these orientations, the ferroelectric domain structure remains stationary with cycling electric field. **e),f)** Switchable non-local signal overlaid with the ferroelectric hysteresis for both the single variant and chevron-like cases. **g)** Combined with the above measurements, we hypothesize that the anisotropy can be explained by a split and anisotropic magnon dispersion, where the magnon conductivity maps to a surface with directions defined by **q** and **k**. The distance from the origin is representative of the conductivity, and thus the population.

the in-plane component of the polarization, where the direction of magnon propagation $\mathbf{q}$ is fixed, the detected first-harmonic non-local voltage $V_{NL,1\omega}$ switches hysteretically on the scale of $\sim 1\mu$V for a device spacing of 2μm. The repeatable difference between the two polarization states is indicative of a non-reciprocity in the magnon dispersion tied to the direction of $\mathbf{P}$. This can be qualitatively rationalized in the form of a Rashba-like, DMI-induced splitting of the spin-dependent magnon bands (sketched in Fig. 5.8b) [139–143]. The result is a $V_{NL,1\omega}$ that is both nonreciprocal and switchable. Since the samples under investigation exhibit no net magnetic moment, the inference is that magnon non-reciprocity in BFO should stem from the magnetic cycloid, which interacts with $\mathbf{P}$.

Under an applied electric field, this hysteresis in $V_{NL,1\omega}$ follows the switching of $\mathbf{P}$, where $\mathbf{P}$ and $\Delta V_{NL,1\omega}$ both flip signs at the same coercive voltage (Figure 5.8e,f) [144]. As the ferroelastic domain walls remain stationary during this event, a comparison can be made between samples with quasi-1D and chevron-like configurations (Fig. 5.8c,d). In quasi-1D samples with a single $\mathbf{k}$ state, the magnitude of $V_{NL.1\omega} \perp \mathbf{k}$ is two-times higher than that of the samples showing a chevron-like magnetic cycloid. The magnitude of this scaling parallels the observations in Figure 5.8, where the chevron-like texture shows a lower conductivity than in the single $\mathbf{k}$ samples with $\mathbf{q} \perp \mathbf{k}$. Taken together, these measurements allows us to sketch the approximate shape of the magnon dispersion projected into the plane of the film (Fig. 5.8g), where $\theta = 90°$ is high conductivity, $\theta = 0°$ is low, $\theta = 45°$ is intermediate, and there is non-reciprocity for magnons with opposite spins.

Conclusion

These results demonstrate control of the magnetic structure of BFO and a method for effectively decoupling the magnetic structure from the ferroelectric domains. This has significant implications for magnonic devices using BFO, in that fundamental anisotropies of the cycloid structure can be used to optimize transport. The formation of a quasi-1D ordered magnonic lattice comprised of the spin cycloid is of fundamental interest in terms of phase transitions in a 1D lattice and the possibility of obtaining long-range order in them. In this sense, future studies could be directed towards controlling the ferroelectric/ferroelastic domain structure through the use of vicinally cut substrates [131].

In conclusion, using heteroepitaxy as a building block and imposing a combination of electrostatic and elastic constraints, we can strategically design both the ferroelectric and magnetic domain structure of multiferroic BFO. This anisotropic structure results in preferential spin-wave conduction orthogonal to its axis, due to the opening of a gap in the magnon dispersion created by the periodicity of the magnetic lattice. Leveraging magnetoelectric coupling, this magnetic texture can be dynamically tuned using an electric field, allowing us to empirically map the magnon dispersion in the film plane with respect to the direction of ferroelectric polarization. This opens the door for the design of magnonic devices using the anisotropy of the spin texture, as well as providing fundamental insights into the conduction of spin waves in complex magnetic systems.

6 Electric-Field Controlled Magnon Transport in a Single Ferroelectric Domain in $Bi_{1-x}La_xFeO_3$

In this chapter, we study magnon transport in La-doped $BiFeO_3$ films. To recount the properties of the parent compound, the ground state of bulk $BiFeO_3$ has a large polarization ($\sim 90\,\mu C/cm^2$) along $[111]_{pc}$ (pc: pseudocubic) and exhibits a canted G-type antiferromagnetism modulated by a spin cycloid (period $\sim$ 65 nm [125]) below the Néel temperature (640K). Rhombohedral $BiFeO_3$ in its G-type antiferromagnetic state shows Rashba splitting which is intrinsically linked to spin-dependent transport [145]. $BiFeO_3$ features two principle Dzyaloshinskii-Moriya (DM)-like interactions, linked to the polarization and the antiferrodistortive octahedral tilts [127], where the tilts and polarization are strongly coupled [146–148]. The octahedral tilt induces a weak magnetic perturbation, and corresponding spin density wave, on top of the antiferromagnetic cycloid of $BiFeO_3$ [127, 148]. This can be imaged directly using scanning Nitrogen-vacancy (NV) magnetometry[129].

To introduce tunability into the multiferroic properties of $BiFeO_3$, rare earth substitution (e.g., Lanthanum for Bismuth) has shown great potential. Often, in these systems, the ferroelectric polarization moves away from $[111]_{pc}$ [149, 150] introducing competition between ferroelectric and antiferroelectric phases [71, 150–152]. This may allow for additional switching pathways compared to the parent compound $BiFeO_3$, leading to the possibility for new ferroelectric domain configurations. Understanding the formation of a single-domain multiferroic and its potential as a model system for efficient spin magnon transport is the focus of this chapter.

Theoretical Calculations

We start with theoretical calculations to understand the energetics of the multiferroic ground state of $BiFeO_3$ (BFO) and La-substituted $BiFeO_3$, $Bi_{0.85}La_{0.15}FeO_3$ (BLFO). We use the effective Hamiltonian given by [127], and use density functional theory to calculate the coupling coefficients for pure BFO and BLFO. The spontaneous polarization largely arises from the 6s electrons in the Bi^{+3} ion [153], and when Bi is substituted for La, which does not have the 6s electrons, the polarizability is decreased. Beyond ∼18% La substitution, the material undergoes a phase transition from a polar state into an antipolar phase [71, 150]. The reduction in polarization is accompanied by a corresponding reduction in the polarization dependent DM interaction strength [154] and thus the cycloid becomes less energetically stable. We find that for pure BFO, the polar structure is $R3c$ and the cycloid is a stable magnetic state. For BLFO, the cycloid is also a stable magnetic state, but since the energy landscape is so modified as previously discussed, the canted moment states $M1$ and $M2$ become much closer in energy to the cycloid. The results of these calculations are shown in Fig. 6.1a, where we have plotted the difference in energy between the $R3c$-cycloid state and the so-called complex states – mixed states of spin cycloid and uniform G-type canted antiferromagnetic phases. The result of these changes in energetics is that the energy landscape is modified as shown schematically in Fig. 6.1b, where the energy barrier to switch between the two degenerate ferroelectric/spin cycloid states is reduced for BLFO.

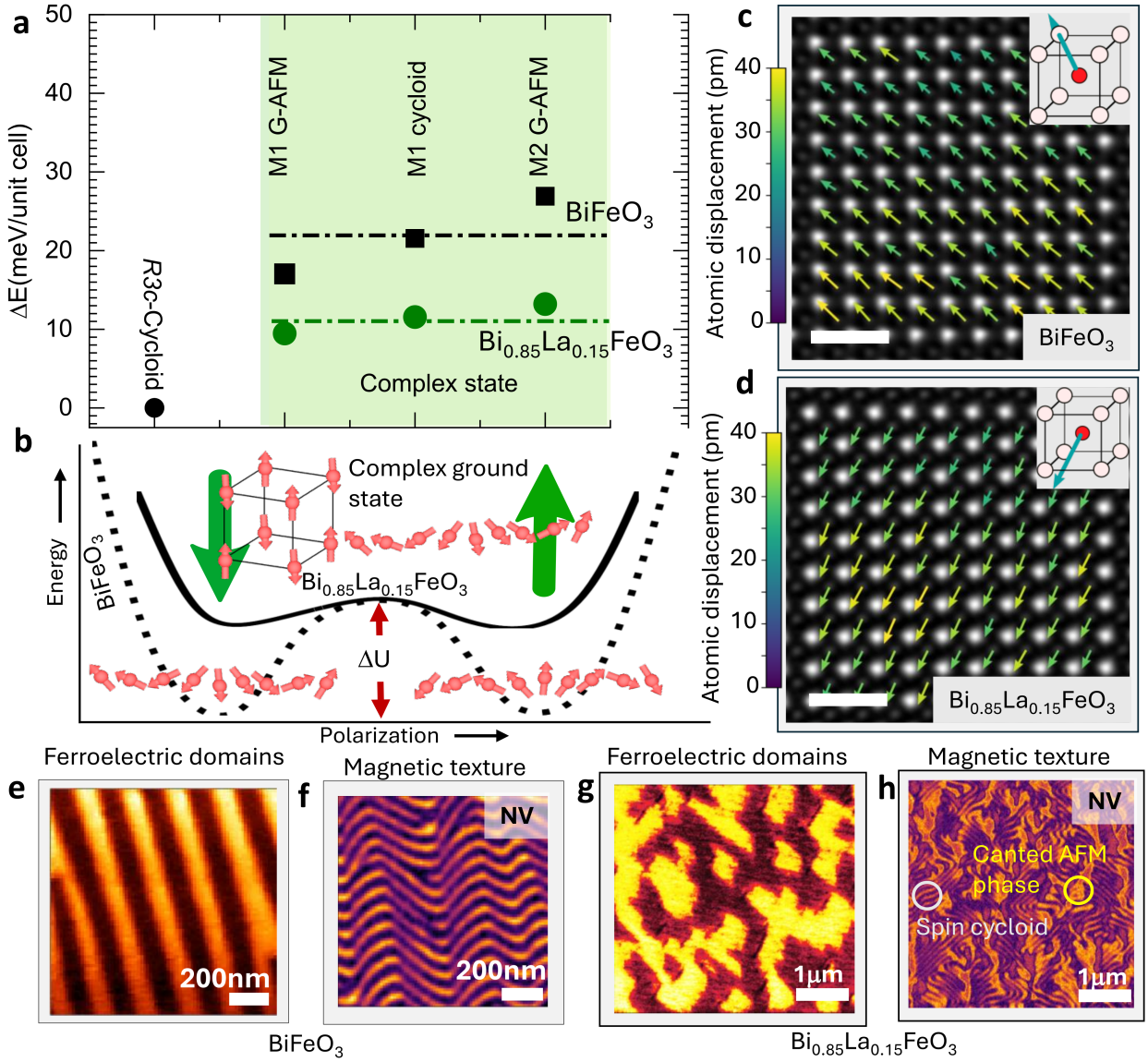

Figure 6.1: **Multiferroic Ground State of BFO and BLFO**. **a)** Calculated magnetic ground state energy of the spin cycloid and G-type antiferromagnetic phases in BFO and BLFO. $R3c$ is the uniform spin cycloid, while $M1$ and $M2$ are modulated polar configurations. **b)** Schematic of the energy landscape of the BFO and BLFO. Red arrows show the Néel vector forming the spin cycloid, or the magnetization in G-type antiferromagnetism. Green arrows represent the polarization in the double-well structure. **c),d)** High angle annular dark field (HAADF) scanning transmission electron microscopy (STEM) images and polar vector mapping in BFO and BLFO. Insets are schematics of the estimated polarization direction in the unit cell of BFO and BLFO. The scale bar is 1 nm. **e)-h)** Ferroelectric domain structure (PFM) and corresponding magnetic texture (iso-B NV images) of pristine BFO and BLFO. The areas of uniform contrast in **h** show the canted phase.

Multiferroic Ground State

BFO and BLFO thin films were prepared by pulsed laser deposition (PLD) in an on-axis geometry with a target-to-substrate distance of ~ 50 mm using a KrF excimer laser (wavelength 248nm, COMPex-Pro, Coherent) on $DyScO_3$ $(110)_O$ (O: Orthorhombic) substrates.

We chose $DyScO_3$ substrates because of the close lattice match (-0.3%) that helps with the high quality epitaxial thin film growth. Film thickness was fixed to 90 nm. BFO and BLFO layers were deposited without a bottom electrode with a laser fluence of 1.8 J/cm^2 under a dynamic oxygen pressure of 140 mTorr at 710°C with a 15 Hz laser pulse repetition rate. The samples were cooled down to room temperature at 30°C/min at a static O_2 atmospheric pressure. The polar and magnetic textures of the samples were measured by Piezoforce microscopy (PFM) and Nitrogen Vacancy (NV) imaging respectively. Fig. 6.1e,f (g,h) show these results for BFO (BLFO). The stripy, characteristic 71° domains can be seen in the BFO, with the corresponding chevron-pattern magnetic cycloid structure as discussed in the previous chapter. However, in BLFO, we find large, blocky domains instead of stripy domains, with a much more varied magnetic structure, with cycloid phases, as well as some of those G-type canted antiferromagnetic phases/complex phases referenced in Fig. 6.1a.

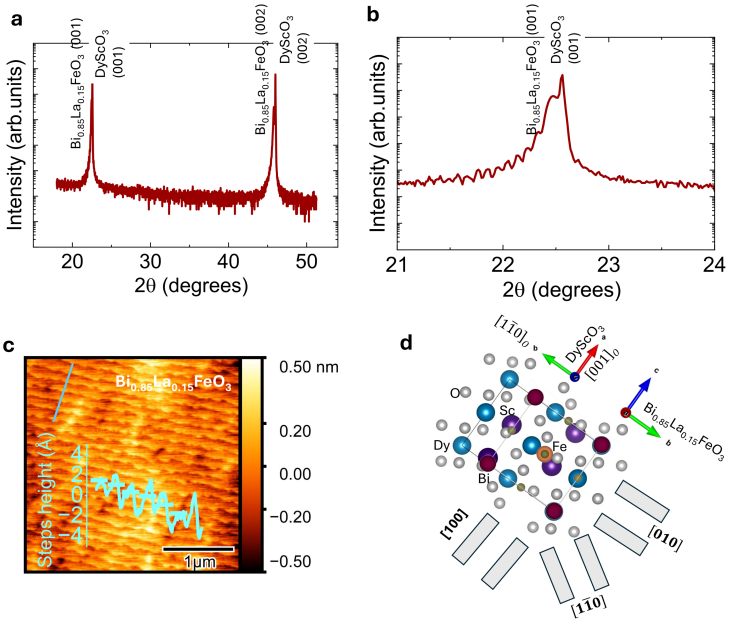

Figure 6.2: **X-ray diffraction and atomic force microscopy**. **a)** XRD of BLFO on DSO substrate, **b)** zoomed in to show the thickness oscillations. **c)** AFM, showing atomically flat steps, with a linescan inset. **d)** Orientation of the devices and BLFO with respect to the orthorhombic DSO substrate.

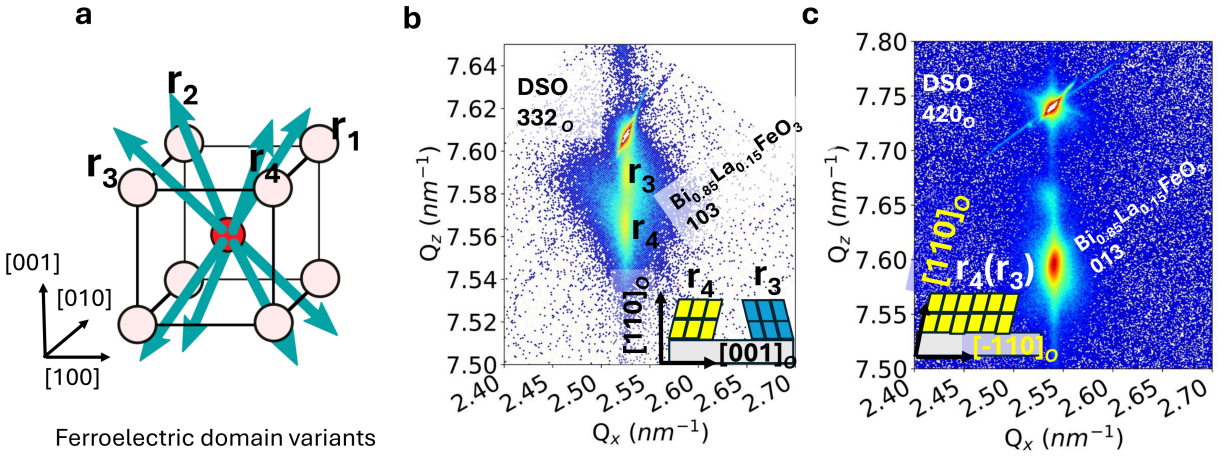

Figure 6.3: **Reciprocal space mapping of BLFO. a)** The 4 structural variants, each with 2 different polarizations, may be present in the sample. **b)** The $(103)_{pc}$ peaks, and **c)** $(013)_{pc}$ peaks, with insets describing which structural variants, drawn schematically, are visible at the given diffraction condition.

Since $DyScO_3$ (DSO) $(110)_O$ in an anisotropic substrate, there should be some anisotropy in the samples. In BFO, the anisotropy comes in the direction of the 71° domain stripes. For the remainder of the paper, we will set aside BFO except for comparisons to BLFO, and focus on BLFO. The misfit strain between BLFO and DSO is $\sim 0.2\%$ along the $[001]_O$ direction and $\sim 0.33\%$ along the $[1\bar{1}0]_O$ direction. These values are evaluated using lattice constants measured from reciprocal space mapping (RSM). We use X-ray diffraction (XRD) and Atomic force microscopy (AFM) in Fig. 6.2 to ensure high quality epitaxial growth. The XRD is single phase with thickness oscillations, and the AFM shows atomically flat BLFO steps. Later in the paper, we use pseudocubic directions to denote device orientations, and those are oriented with respect to the substrate orthorhombic directions in Fig. 6.2d.

Reciprocal space maps of BLFO are measured to further probe the crystal structure (Fig. 6.3). Mapping the $(332)_O$ planes in DSO shows the $(103)_{pc}$ planes in BLFO, suggesting that BLFO is epitaxially strained to the substrate. Peak-splitting occurs in the $(103)_{pc}$ diffraction condition, but not in the $(013)_{pc}$ condition. This indicates that only 2 of the 4 structural variants indicated by Fig. 6.3a are present in the films, consistent with PFM results in previous studies [71].

Polarization mapping is also performed on BFO and BLFO samples – in the same way as it is done on BLFO in Chapter 4 – with the high quality HAADF-STEM images (Fig. 6.1). The BFO polarization is along $\langle 111 \rangle_{pc}$, which is well-understood. The BLFO, however, shows a polarization direction shifted away from $\langle 111 \rangle_{pc}$ towards $\langle 112 \rangle_{pc}$, which is consistent with previous reports [71]. Vertical PFM shown in Fig. 6.4 with no contrast shows that the polarization is either all up or all down, and the TEM indicates that the polarization vectors for the BLFO point down, that is, in conjunction with the structural distortions measured by RSM, the polarization can take on the directions $[\pm 1\bar{1}\bar{2}]_{pc}$ in the pristine state. Other states can be reached with electric field poling.

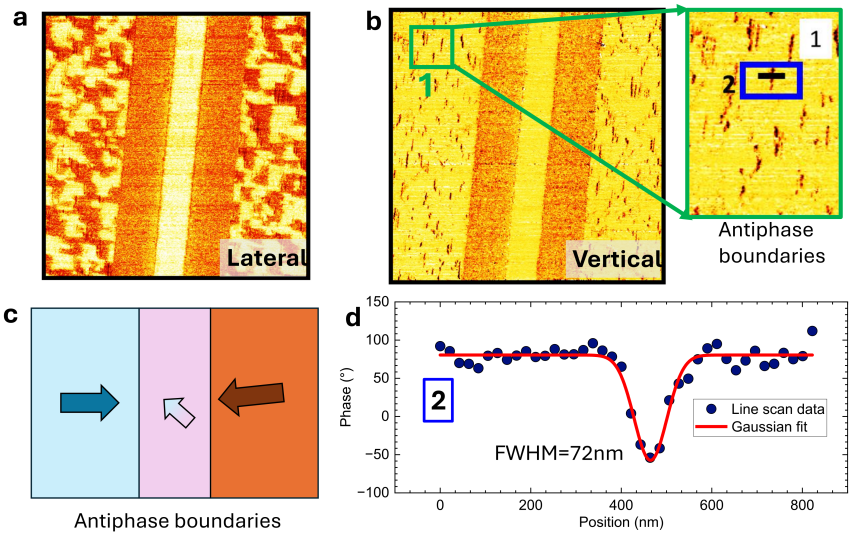

Figure 6.4: **Head-to-head boundaries in multidomain regions. a)** Lateral and **b)** Vertical PFM images of a [010] device after poling. The zoomed section of the vertical phase shows the boundaries, and a linescan in phase across the boundary shows that **d)** the phase drops about 180° across the domain boundary.

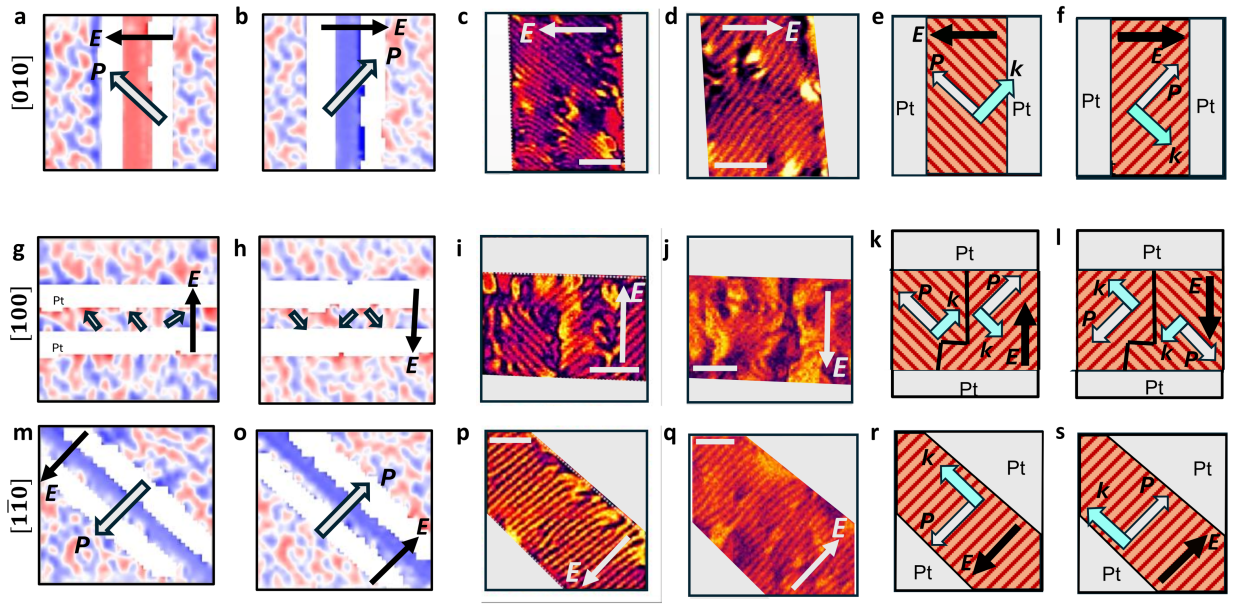

Figure 6.5: **Electric field control of magnetic and polar texture**. SHG linear dichroism maps, iso-B NV images, and schematics for **a)-f)** $[010]_{pc}$ devices, **g)-l)** $[100]_{pc}$ devices, and **m)-s)** $[1\bar{1}0]_{pc}$ devices. SHG for in-plane polarization and NV for magnetic texture are recorded for two opposite poling directions. Solid colored arrows represent the poling electric field direction, bordered arrows represent the in-plane direction of the polarization, and in the schematics, the light blue-filled, black bordered arrows represent the spin cycloid propagation direction **k**. In the schematics, the stripes are indicative of the spin cycloid as observed in previous studies [129, 155]. The schematics highlight the relationship between **k** and **P**. The scale bars in the NV images are 500nm, and the distance between the Pt wires (white rectangles) in the SHG images is $\sim 1.5\mu$m.

Electric field control of multiferroic structure

To understand the effect of electric field on the as-grown ferroelectric domain structure, and therefore the ferroelectric polarization, in-plane capacitors were fabricated by optical lithography (*ex-situ* sputtered platinum (Pt) wires 120μm$\times 1.3\mu$m$\times$15nm, with $\sim 2\mu$m spacing and resistivity of $\sim 20\mu\Omega$cm). The devices were patterned along four different angles in which the long-axis of Pt electrode pairs are parallel to the substrate $[100]_{pc}$, $[010]_{pc}$, $[110]_{pc}$, and $[\bar{1}10]_{pc}$ (Figure 6.7a). To visualize the ferroelectric domain reversal across the in-plane devices, we use both optical second harmonic generation (SHG) and Piezo-force microscopy (PFM) to map the in-plane polarization. From SHG, linear dichroism maps and knowledge of the poling field direction allow us to determine which of the 4 polarization states $[\pm 1 \pm 1\bar{2}]_{pc}$ are achieved within each device, see Appendix E for more detail. To determine the effect electric field has on the magnetic structure, we do NV-imaging after poling in the different directions in different devices. The results are summarized in Fig. 6.5.

First, for the $[010]_{pc}$ devices, that is, when an electric field is applied in the $[100]_{pc}$ direction, the entire region between the wires is switched, to a single domain of either $[1\bar{1}\bar{2}]_{pc}$ or $[\bar{1}\bar{1}\bar{2}]_{pc}$ depending on the direction of the poling field. The magnetic texture is also switched, as can be seen in Fig. 6.5. The formation of a single multiferroic domain here is novel; previously, monodomain features were realized through a non-trivial approach to pure

BFO using a scanning probe-tip-based method in a slow scan mode to physically write a monodomain using a localized electric field from the scanning probe tip [129, 156], requiring several minutes per micron, and an extremely careful experimental protocol [157, 158]. Here, a single voltage pulse is required between the two wires.

For the $[100]_{pc}$ devices, that is, when an electric field is applied in the $[010]_{pc}$ direction, a blocky multidomain state persists, with domains having polarization in $[\pm 11\bar{2}]_{pc}$ or $[\pm 1\bar{1}\bar{2}]_{pc}$ depending on the poling direction. In this multidomain case, upon poling, the domains are locally switched, as can be seen by careful PFM (Fig. 6.6) due to local polarization rotations, where the head-to-head domain wall boundaries that run along the $[010]_{pc}$ direction don't move. We note that these domain walls are only head-to-head in the component of polarization that is normal to the domain wall, and they don't move only in response to a field applied along the $[010]_{pc}$ direction. This asymmetric behavior between $[010]_{pc}$ devices and $[100]_{pc}$ devices can be attributed to the aforementioned anisotropic substrate strain. In devices with electrodes parallel to $[1\bar{1}0]_{pc}$ and [110], a single ferroelectric domain is formed which can be expected since a component of the electric field points along [100], allowing the antiphase boundaries to nucleate and move with the field. In these devices, the in-plane component of the polarization matches the E-field direction, while the out-of-plane component is fixed.

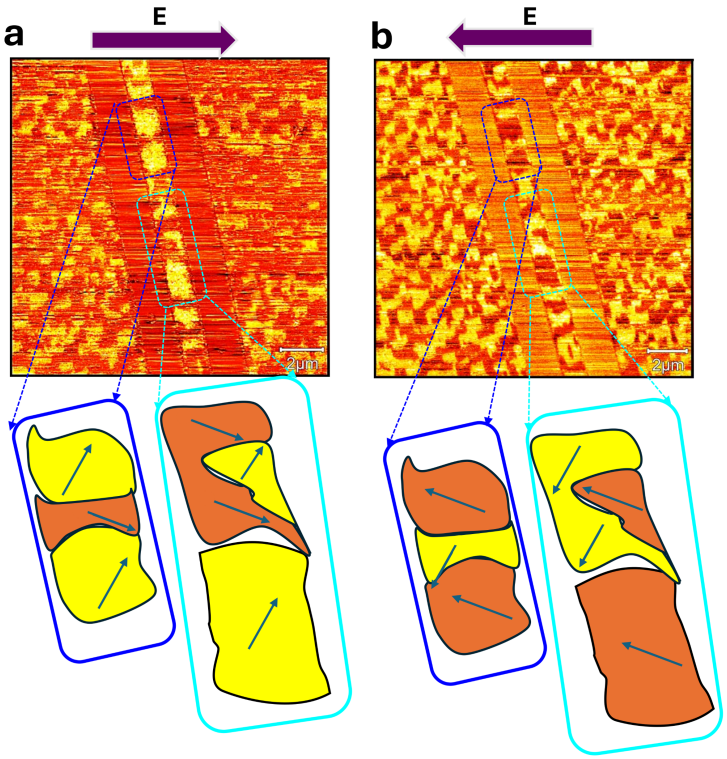

Figure 6.6: **Careful PFM of $[100]_{pc}$ device.** The color corresponds to the polarization as denoted by the schematics, and an opposite E-field poling rotates the polarization of each domain by 90° locally.

Electric Field Control of Magnon Transport

The device structure and procedure for measuring spin transport is identical to that in the previous chapter. However, here, we focus on applying electric field to change **P** and maintain one direction for diffusion direction **q**. First, an in-plane electric field is applied between source and detector wires. Following each electrical pulse, a low-frequency (7Hz) alternating current is introduced into the source wire, generating a magnon spin current through the spin Seebeck effect. Subsequently, a non-equilibrium magnon spin accumulation at the BLFO interface underneath the Pt detector initiates the flow of spin angular momentum into the adjacent Pt. The resulting spin current is then converted into a measurable voltage

through the inverse spin Hall effect (ISHE) of Pt, and the signal is lock-in detected at 2ω. Each data point is averaged over a duration of 150s, with the electric field off. The electric field is only used to pole the multiferroic into a remnant state for spin transport, it is removed for nonlocal voltage (V_{ISHE}) measurement. The nonlocal voltage hysteresis reflects the ferroelectric hysteresis (Fig. 6.7), indicating the existence of polarization-controlled magnon transport. Notably, in the $[010]_{pc}$ devices, the electric field and therefore the polarization has the capacity to control the sign of the magnon spin current flowing through the BLFO. Here, the ferroelectric polarization deterministically controls, in a nonvolatile way, non-reciprocal magnon transport.

Similar experiments on BFO with a stripy domain structure are performed and a comparison is presented in Fig. 6.7e. Data corresponding to BFO is also extracted from prior experiments [14]. We find that the BLFO has a consistently higher voltage output than the

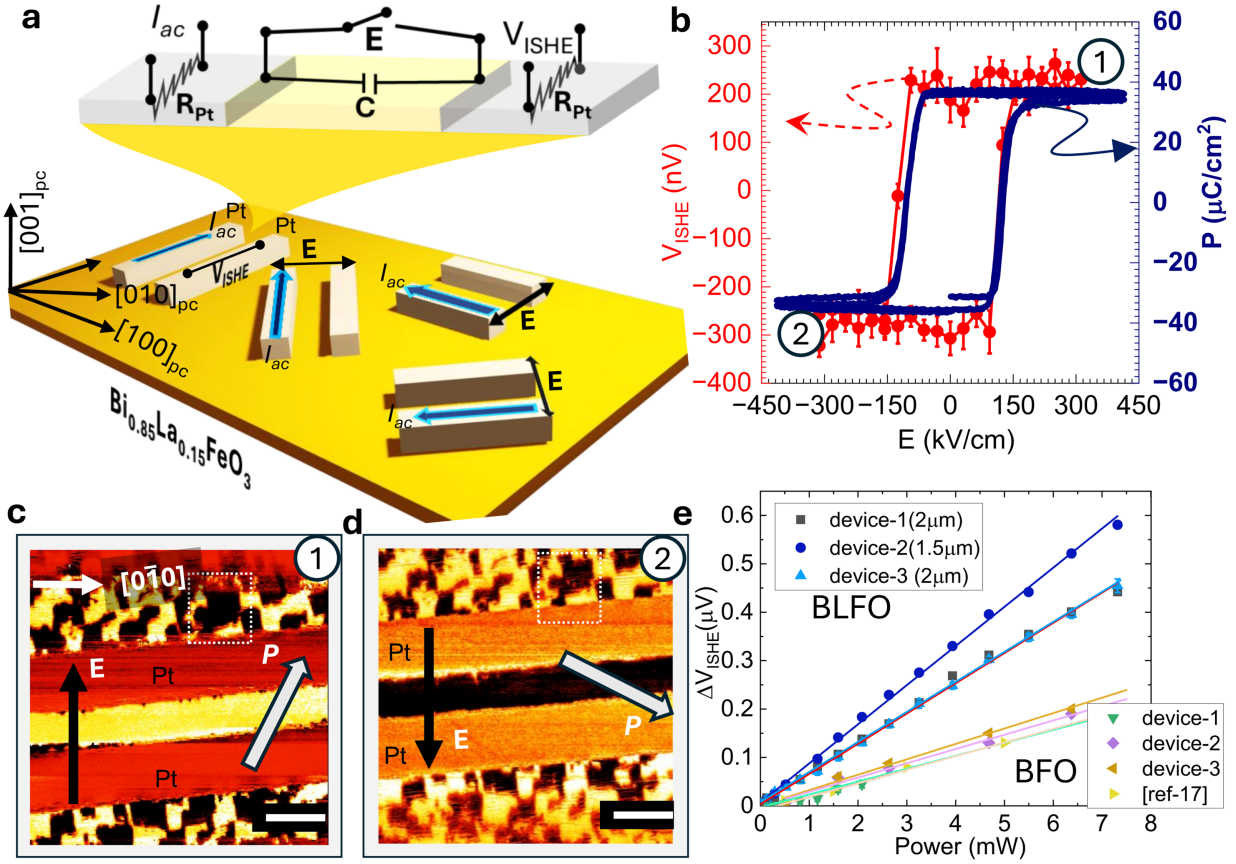

Figure 6.7: **Electric field control of magnons in BLFO $[010]_{pc}$ devices. a)** Nonlocal magnon spin-transport measurement schematic with Pt as source and detector for spin-charge interconversion. A circuit schematic of 4-terminal devices is included, where a switchbox is used to switch between the measurement configuration (resistive circuits) and the electric field application configuration (capacitor circuit). **b)** Polarization and quasi-static magnon hysteresis as a function of external electric field. A Radiant Technologies ferroelectric test system is used to measure the polar hysteresis. Error bars in the ISHE voltage represent the deviation of the lock-in measurement over 150s. **c),d)** The corresponding PFM images after electrical poling in two opposite directions. The scale bar is 2μm. **e)** Differential voltage between the two poled states recorded in $[010]_{pc}$ devices as a function f the power injected into the source, for BLFO and BFO samples.

BLFO, by over a factor of 2 at equal spacing. Furthermore, we find that the magnitude of the electric field required to switch the magnon spin current is smaller, consistent with prior studies [71] (Fig. 6.10). This doubly confirms the key advantages of single-domain BLFO over its parent compound.

We perform the same spin-current measurements on devices pointing along the different crystallographic directions under the same protocol as discussed above. Strikingly, the multidomain $[100]_{pc}$-oriented device does not show any ISHE hysteresis (Fig. 6.8) despite exhibiting a clear ferroelectric hysteresis (Fig. 6.9). This can be explained with the knowledge of how the spin cycloid transforms under electric field in the $[100]_{pc}$ devices: both directions of **k** for the spin cycloid remain present, and if the two domains result in opposite values for V_{ISHE} as seen in the $[010]_{pc}$ devices, then a sample with equal population of both domains should give no V_{ISHE}. There is a considerable offset to the voltage, but no hysteresis, we hypothesize that the offset could come from other thermal sources such as a magnon current in the $[001]_{pc}$-direction [159]. Although a precise correlation between the spin cycloid propagation direction **k** and the nonlocal voltage would be interesting, the present observations affirm that the direction of **k** holds greater significance than the net polarization in determining the non-local magnon signal.

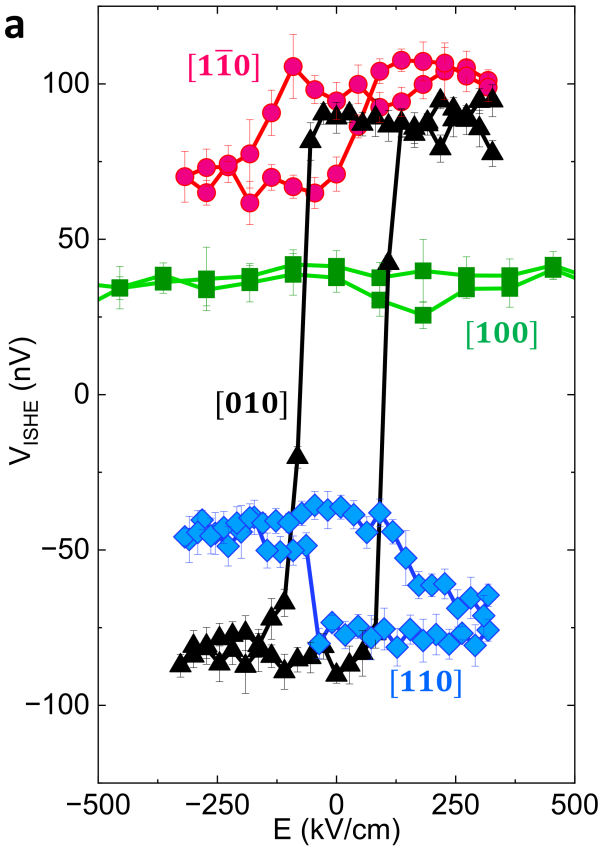

Figure 6.8: **Magnon-generated nonlocal ISHE voltage hysteresis**. Measured as a function of the external in-plane electric field in devices with four different orientations labeled by the pseudocubic direction along which the Pt wires lie. The power in the source wire is fixed to 2mW.

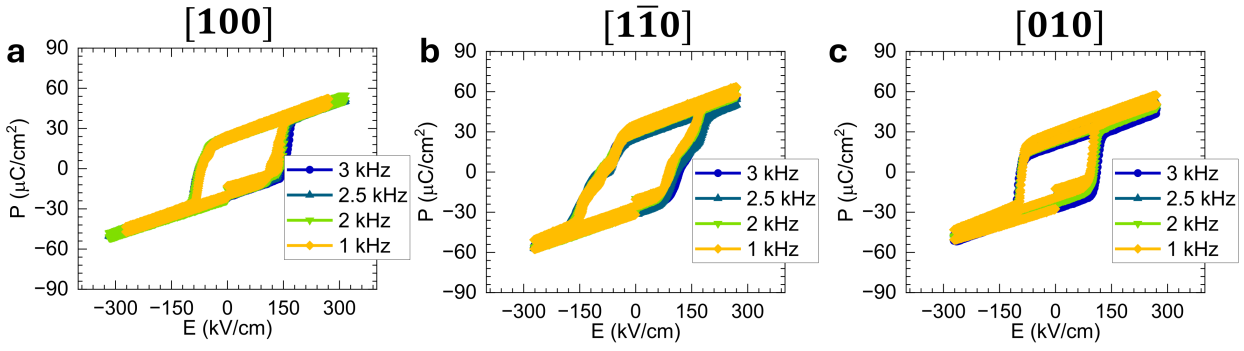

Figure 6.9: **Ferroelectric hysteresis in devices.** A Radiant was used to capture the above ferroelectric hystereses in devices with wires oriented along **a)** $[100]_{pc}$, **b)** $[1\bar{1}0]_{pc}$, and **c)** $[010]_{pc}$. We note that the magnitude of polarization as measured here does not influence the measured nonlocal voltage signal.

As shown in Fig. 6.8, we note that the $[1\bar{1}0]_{pc}$ ($[110]_{pc}$) devices have a lower magnitude hysteresis with a positive or negative offset. The sign of the offset is consistent from device to device. From first glance at the NV-data in Fig. 6.5 for these devices, it appears that the spin cycloid propagation **k** does not change when **P** is thus switched by electric field poling, however, it is possible that a more complicated switching mechanism takes place that switches a particular symmetry of the spin cycloid in a way that leaves it invariant under NV imaging but not under nonlocal magnon excitation measurements. This might be a chirality or handedness, which we leave to further experiments to uncover. Nevertheless, upon closer examination of Fig. 6.9b, the kink in the dynamic ferroelectric hysteresis may indicate a complicated switching pathway that swings the polarization (and the magnetic texture) through two 71° switching events, as opposed to a simple $[11\bar{2}]_{pc}$ to $[\bar{1}\bar{1}\bar{2}]_{pc}$ transformation. We end this discussion by claiming that while the sign of magnon voltage seems to be governed by the direction of cycloid propagation **k**, there may be other aspects of the underlying magnetic texture that govern the magnitude of the magnon spin transport.

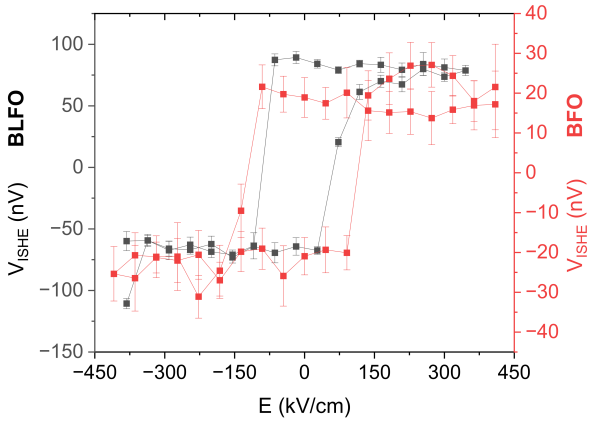

Figure 6.10: Nonlocal magnon transport in BFO and BLFO recorded under identical conditions. The BFO data offset is removed for better comparison, while BLFO $[010]_{pc}$ devices always exhibit little or no offset.

Conclusion

In summary, our study demonstrates the effective transmission of magnons in La-substituted $BiFeO_3$, resulting in a multiferroic material that can be polarized into a stable non-volatile uniform ferroelectric domain with a single variant of the spin cycloid. This stands in contrast to pure $BiFeO_3$, where the coexistence of two variants in both spin cycloids and stripe-like ferroelectric domains leads to a diminished magnon signal. We observe that by suitably choosing the direction of the applied electric field, it is possible to maximize or cancel out the effect of ferroelectric switching on magnon transport. This research provides a means to customize ferroelectric domains and complex antiferromagnetic spin cycloids, as well as to understand the resulting spin transport, offering a pathway to design the single domain multiferroics for efficient magnon transport for future applications in magnetoelectric spin-orbit logic and memory.

7 Phenomenological Model of Electric-Field Controlled Magnon Transport in Multiferroics

Electric field control of magnon transport through BFO – such as that described in Chapters 5 and 6 and in Fig. 7.1 below – has recently been demonstrated [14, 15, 110, 160]; however, the microscopic mechanism of the magnon-mediated spin transport remains unknown. This is in contrast to ferro(ferri)magnets, where the spin carried by magnons is simply controlled by the magnetic field, and the microscopic origins of spin transport are well described [10–12].

Despite the complexity of the magnetic structure in BFO [129, 155], a simple phenomenological approach to magnon-mediated spin transport in a generalized magnetic texture would offer insight into the physical mechanisms of electric-field-controlled magnon transport. By applying mirror and time-reversal operations on the magnon propagation, it is possible to predict the behaviour of the spin current based on the transformations of the magnetic texture

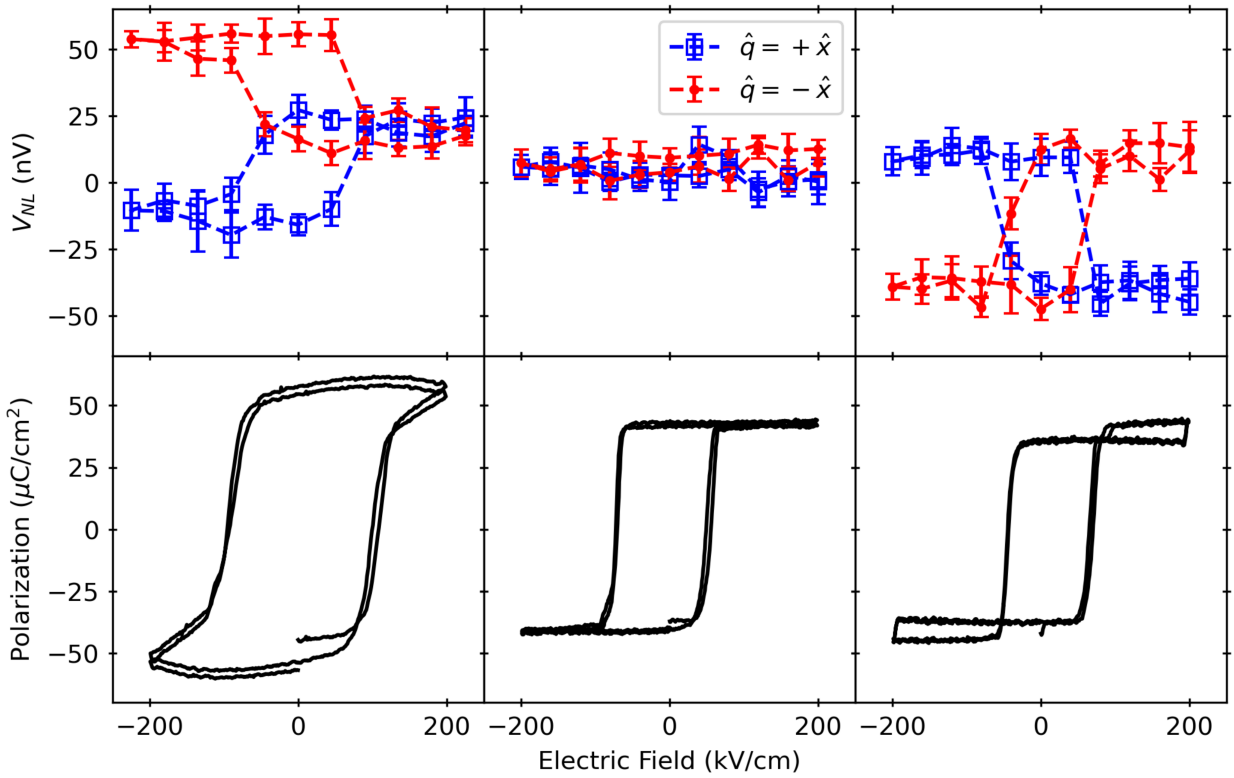

Figure 7.1: **Nonlocal voltage and Polarization.** V_{ISHE}, the detection of a thermal magnon-mediated spin current, is measured here as a function of poling electric field for 3 samples; from left to right: 50nm BFO on a $TbScO_3$ (TSO) substrate, two-domain La-doped BFO on a $DyScO_3$ (DSO) substrate (from previous chapter, [100] devices on BLFO), and single-domain La-doped BFO on DSO substrate (from previous chapter, [010] devices). The polarization hysteresis is a dynamic measurement with electric field, however the nonlocal voltage is a remnant measurement, where the electric field is turned off during the V_{ISHE} measurement. V_{ISHE} switches when the ferroelectric polarization, and the underlying magnetic state, switches. In two samples, this corresponds to changes in V_{ISHE}, however in one sample it does not. Measurements are made for two different magnon diffusion directions $\hat{\mathbf{q}} = \pm\hat{\mathbf{x}}$ through the multiferroic.

under these operations. We apply this to thermally excited magnon-spin transport in three model BFO samples with different spin-cycloid configurations, where the behavior of the polarization and the magnetic texture under different electric fields has been mapped. We find that the model's predictions, based on the symmetries associated with the samples' magnetic textures, match the measured magnon-transport data. These results show that this model can be a powerful tool to guide further studies into the microscopic origin of magnon-mediated spin transport, as well as predict the qualities of magnon transport in new multiferroic systems.

Devices and Measurements

Thin films of BFO and $Bi_{0.85}La_{0.15}FeO_3$ (BLFO) were deposited using pulsed-laser deposition and molecular-beam epitaxy, and Platinum (Pt) was sputtered for voltage detection of spin currents arising from non-local excitations [10, 161, 162] (Fig 7.2a). For details on the material depositions, please refer to the notes on BLFO/DSO and BFO/TSO depositions in the previous chapters. Device fabrication is also identical to previous chapters, however some more detail on the device fabrication is given here for completeness. After Pt deposition, which was sputtered at room temperature in 7mTorr of Ar, a positive photoresist (MIR 701), approximately 500 nm thick, was uniformly spin-coated onto the sample. Photolithography was executed through a Karl Suss MA6 Mask Aligner. Following exposure, the resist underwent wet-etching using Megaposit MF-26A photoresist developer, and the Pt layer was

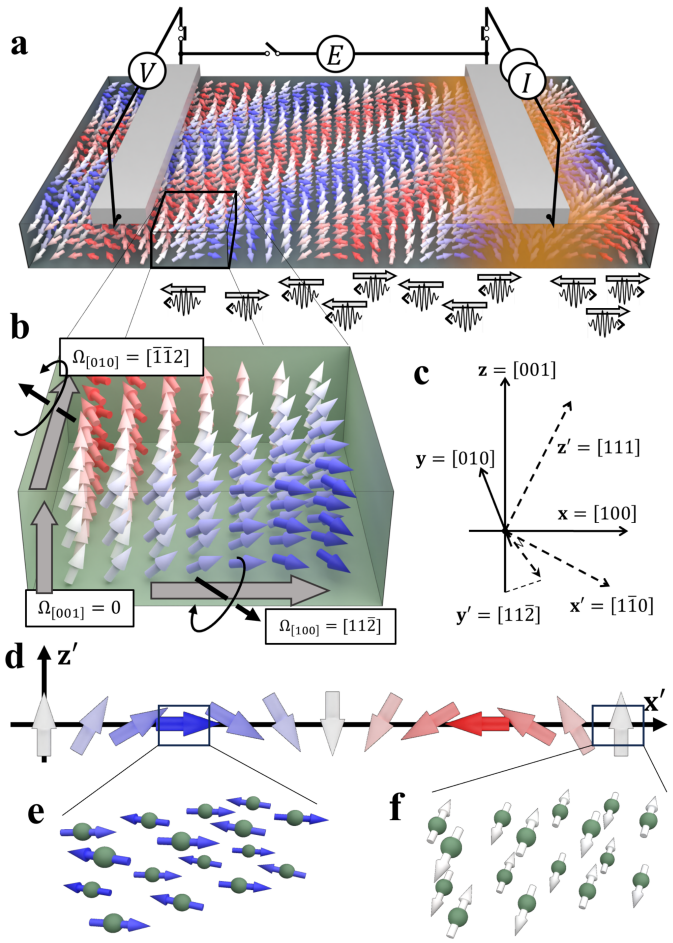

Figure 7.2: **Schematics.** **a)** Magnons (represented by wavepackets) with $\langle S_x \rangle \sim \pm\hat{\mathbf{x}}$, as notated by the block grey arrows, diffuse along the temperature gradient through the BFO (or BLFO) and impart their spin to the detector, generating an ISHE voltage. **b)** The colored arrows represent the local Néel vector in the BFO. The polarization is along $\mathbf{z}' = [111]$ and the cycloid propagation direction is $\mathbf{x}' = [1\bar{1}0]$. The red/blue coloring gives the net moment due to canting, as would be detected in NV microscopy. The vector $\mathbf{\Omega_b}$ represents the axis around which the Néel vector rotates along the direction $\mathbf{b}$. Looking at the change of the Néel vector along the $\mathbf{b} = [100]$, $[010]$, or $[001]$ directions, the Néel vector rotates clockwise, counterclockwise, or not at all around $[\bar{1}\bar{1}2]$, so $\mathbf{\Omega}_{[100],[010],[001]} = [11\bar{2}], [\bar{1}\bar{1}2], 0$. **c)** The device axes has $\mathbf{x}$ parallel to the applied field and temperature gradient, $\mathbf{y}$ parallel to the Pt wires, and $\mathbf{z}$ as the film normal. Cycloid (primed) coordinates have $\mathbf{z}'$ parallel to the BFO polarization, $\mathbf{x}'$ parallel to the cycloid propagation axis, and $\mathbf{y}' = \mathbf{z}' \times \mathbf{x}'$ normal to the plane of the cycloid, which is shown in **d**). **e),f)** The atom to atom variation in magnetic moment from the spin cycloid drawn to scale, including the spin density wave (not drawn to scale). Here, the arrows represent the atomic magnetic dipoles.

subsequently ion-milled down to the multiferroic film surface (using an Intlvac Nanoquest with a Hiden Analytical SIMS), resulting in the formation of rectangular Pt stripes measuring 120 μm $\times$ 1.3 μm. This process was conducted at the Marvell Nanofabrication laboratory at UC Berkeley.

An electric field can be applied between the two wires to set the polarization state of the BFO (BLFO) while disconnecting the source current and voltage detector. The polarization-electric field hysteresis is measured dynamically with a Radiant technologies P-PMF (Fig. 7.1). For nonlocal voltage hysteresis measurements, a Keithley 2400 voltage source is used to apply the electric field between the wires, subsequently the electric field is turned off and a current source is connected across one wire, and the lock-in voltage detector is connected across the other. The lock-in references the second harmonic of the low frequency (7 Hz) source current [10, 161] to select magnons generated from the spin-Seebeck effect (SSE). This is repeated over a range of electric fields to extract the inverse spin-Hall effect (ISHE) voltage (V_{ISHE}) as a function of poling field, and then the identities of the source and detector wires are switched to extract the data from a thermal gradient applied in the opposite direction (Fig. 7.5 and 7.1). It is clear from the data that the nonlocal magnon voltage is not entirely dependent on the net polarization: in two samples, V_{NL} shows a hysteresis corresponding to the ferroelectric hysteresis (and the two hystereses for different choices of $\hat{\mathbf{q}}$ have different relative offsets between those samples), whereas in the third sample, there is no hysteresis in V_{NL} corresponding to any change in net polarization. As described in this chapter, we find that a symmetry-inspired phenomenological model can predict this behavior, and we maintain that this model can be applied to other multiferroic magnon systems.

Magnon Dynamics

To tie the observed magnon signal to the microscopic magnetic structure, we begin with a phenomenological model for magnon transport in a generic multiferroic. In equilibrium, the local magnetization $\mathbf{m}(\mathbf{r})$ will feel an effective field $\mathbf{H}_{\text{eff}} = \delta E/\delta \mathbf{m}(\mathbf{r})$ where E is the magnetic Hamiltonian of the system. Excitations of the local magnetization then follow the dynamics as given by the Landau-Lifshitz-Gilbert (LLG) equation,

$$\dot{\mathbf{m}}(\mathbf{r}) = -\gamma \mathbf{m} \times \mathbf{H}_{\text{eff}}(\mathbf{r}) - \alpha \mathbf{m} \times \dot{\mathbf{m}} \tag{7.1}$$

where γ is the gyromagnetic ratio and α is the Gilbert damping. The solutions $\mathbf{m}(\mathbf{r}, t)$ of this equation are the magnon modes, labeled by μ and $\mathbf{k}$, where $\mathbf{k}$ is the wavevector of the magnon. Since the excitations are bosons, there will be an equilibrium number of magnons in each mode $n^0_{\mu\mathbf{k}}$ as given by the Bose-Einstein distribution. In equilibrium, there is no net flow of spin from the multiferroic to an adjacent detector wire, however, the magnons $n_{\mu\mathbf{k}}(\mathbf{r})$ in non-equilibrium $n_{\mu\mathbf{k}} \neq n^0_{\mu\mathbf{k}}$ underneath the detector wire generate a transfer of spin angular momentum and thus a voltage in the electrode via the inverse spin-Hall effect (ISHE). The spin current $\mathbf{j}_s(\mathbf{r})$ is given by the spin pumping from the total motion of the magnetization [2, 11], or equivalently from the individual spins of each magnon [2, 12, 13]:

$$\mathbf{j}_s(\mathbf{r}) = \tfrac{\hbar}{4\pi} g^{\uparrow\downarrow} \langle \mathbf{m}(t) \times \dot{\mathbf{m}}(t) \rangle \sim \sum_{\mu} \langle \mathbf{S} \rangle_{\mu} \int d^3k \, v_{\mu\mathbf{k},z} (n_{\mu\mathbf{k}} - n^0_{\mu\mathbf{k}}) \tag{7.2}$$

where $g^{\uparrow\downarrow}$ is the spin mixing conductance, $v_{\mu\mathbf{k},z}$ is the $\mathbf{z}$-component of the magnon group velocity $\mathbf{v}_{\mu\mathbf{k}} = \hat{\mathbf{k}}\frac{\partial\omega_{\mathbf{k}}}{\partial\mathbf{k}}$, and $\langle\mathbf{S}\rangle_\mu$ is the expected value of spin of magnon mode μ [163]. One result of the time average in Eq. 7.2 is that a linearly oscillating magnetization transfers no spin, but a precessing magnetization does. The summand in Eq. 7.2 is a generalization of similar equation in thermal magnon studies [2, 12, 13] to include any possible modes μ carrying different spins $\langle\mathbf{S}\rangle_\mu$.

In equilibrium, there is not an excess of magnons beneath the detector wire, however, under a thermal gradient, the diffusion of magnons is governed by the Boltzmann transport equation [12]:

$$n_{\mu\mathbf{k}} - n^0_{\mu\mathbf{k}} = -\tau_{\mu\mathbf{k}}\mathbf{v}_{\mu\mathbf{k}} \cdot \nabla_{\mathbf{r}} n^0_{\mu\mathbf{k}} - \tau_{\mu\mathbf{k}}\mathbf{v}_{\mu\mathbf{k}} \cdot \nabla_{\mathbf{r}}[n_{\mu\mathbf{k}} - n^0_{\mu\mathbf{k}}] \tag{7.3}$$

where $\tau_{\mu\mathbf{k}}$ is the lifetime of a magnon mode given by scattering rates. Each term and boundary condition is derived from either the temperature gradient, the experimental geometry, or the energetics of magnon modes as given by the magnetic Hamiltonian and underlying magnetic state of the multiferroic. These diffusive, non-equilibrium magnons, represented pictorially (Fig. 7.2a), are responsible for the finite spin-current output. Due to this excess of magnons, a total spin current can be calculated by integrating over the detector surface S the spin current coming into the detector interface:

$$\mathbf{I}_s = \int_S d^2r \mathbf{j}_s(\mathbf{r}) \approx \sum_\mu \langle S\rangle_\mu \eta_\mu \quad \text{where} \quad \eta_\mu = \int_S d^2r d^3k \, v_{\mu\mathbf{k},z}(n_{\mu\mathbf{k}} - n^0_{\mu\mathbf{k}}). \tag{7.4}$$

Here, we have introduced η_μ as the extent to which the magnon mode μ contributes its spin $\langle\mathbf{S}\rangle_\mu$ to the detector wire. As a phenomenological function, η_μ is dependent on a) the underlying effective Hamiltonian and the magnetic state, which we will label by Ψ, b) the direction of the magnon diffusion $\hat{\mathbf{q}}$, and c) the device geometry, which is effectively constant throughout all of the studies.

Symmetry-Inspired Model

In a multiferroic, an electric field along $\hat{\mathbf{e}}$ can be used to switch between different ferroelectric (polarization) states, which correspond to different magnetic ground state $\Psi^{\hat{\mathbf{e}}}$. Furthermore, the direction of the thermal gradient (i.e., the direction of magnon diffusion $\hat{\mathbf{q}}$) can also be changed. In our experiment, we can alternate between $\hat{\mathbf{q}} = \pm\hat{\mathbf{x}}$ by switching the identity of the source wire and the detector wire. This is done automatically with a switchbox to ensure repeatability. We switch the ferroelectric state by poling with positive or negative voltage across the detector and source wires, giving $\hat{\mathbf{e}} = \pm\hat{\mathbf{x}}$, where $\hat{\mathbf{e}}$ is the direction of the poling field above the critical field (see Fig. 7.1). Thus, for our phenomenological function which gives the extent to which magnon mode μ imparts its spin to the detector wire, we write $\eta^{\hat{\mathbf{e}}}_\mu(\hat{\mathbf{q}})$ for the magnetic ground state $\Psi^{\hat{\mathbf{e}}}$ as a function of $\hat{\mathbf{q}}$. The nonlocal voltage, $V = R_{\mathrm{Pt}}\theta_{\mathrm{Pt}}(\mathbf{I}_s \cdot \hat{\mathbf{x}})$ is then also a function of $\Psi^{\hat{\mathbf{e}}}$ and $\hat{\mathbf{q}}$ ($\mathcal{I}$ row of Fig 7.3). R_{Pt} and θ_{Pt} are the resistance and spin-Hall angle of Pt. We are only interested in the $\hat{\mathbf{x}}$ component of $\mathbf{I}_s$ because the ISHE current is a cross product between the spin-current direction, $\hat{\mathbf{z}}$, and the spin-current polarization, $\hat{\mathbf{I}}_s$, and we can only measure ISHE voltages in the $\hat{\mathbf{y}}$-direction. Any other components of $\mathbf{I}_s$ do not contribute to the measured voltage.

Next, we consider symmetry operations on the ground state, experimental configuration, and magnon dynamics to impose constraints on the four values $V_{\text{ISHE}} \equiv V^{\hat{\mathbf{e}}}(\hat{\mathbf{q}})$ (Fig. 7.3) for $\hat{\mathbf{e}}, \hat{\mathbf{q}} = \pm\hat{\mathbf{x}}$. First, we consider the time reversal operation $\mathcal{T}$. A magnetic ground state with unpaired spins will break time-reversal symmetry, however, it is possible that the action of $\mathcal{T}$ on a magnetic texture is equivalent to a translation. For a translation in such a periodic magnetic texture with no global net magnetization, the magnon dynamics (i.e., diffusion, spin transport) integrated over an area much larger than the periodicity of the texture will be invariant under the translation, and thus will also be invariant under $\mathcal{T}$.

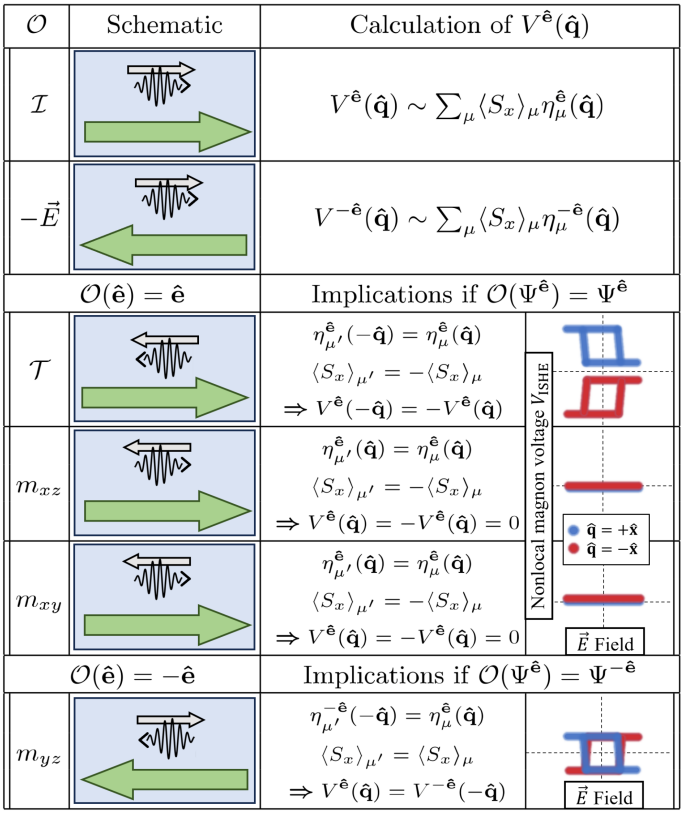

Figure 7.3: **Symmetry operations.** Several symmetry operations on a magnon mode μ with spin $\langle \mathbf{S} \rangle_\mu \parallel \hat{\mathbf{x}}$ diffusing in the $\hat{\mathbf{x}}$ direction, through a multiferroic poled along $\hat{\mathbf{x}}$. The black arrow attached to the wavepacket denotes the magnon diffusion direction, the grey arrow denotes the magnon spin direction, and the large green arrow denotes the poling direction. The rows show, from top to bottom, the identity, electric field poling, time reversal, and mirror operations over the xz, xy, and yz planes. If the material (blue background) is invariant under the operations, we would expect each of the mathematical relations and their reflections on the measured magnon signal (as shown in the implications column) to hold true. We note that the $V^{\hat{\mathbf{e}}}(\hat{\mathbf{q}})$ values in the hypothetical magnon signals shown here are arbitrary. A visualization of these symmetry operations carried out on the spin cycloid is included in Fig. 7.4, however we emphasize that this model can be used for any generalized magnetic texture, not just the spin cycloid of BFO.

For any thermal magnon mode μ in such a magnetic texture, the action of $\mathcal{T}$ will transform the mode μ into the mode μ', with spin and diffusion reversed, as shown schematically ($\mathcal{T}$ row of Fig. 7.3). Due to the invariance of the magnetic texture under $\mathcal{T}$, however, the dynamics encapsulated by η will be the same for both modes. Summing over all modes μ' to get a nonlocal voltage, we find that $V^{\hat{\mathbf{e}}}(\hat{\mathbf{q}}) = -V^{\hat{\mathbf{e}}}(-\hat{\mathbf{q}})$, which can be seen by combining the first two equations in the $\mathcal{T}$ row with the equation in the $\mathcal{I}$ row of Fig. 7.3. When the two-hysteresis measurements of V_{ISHE} are made for such a multiferroic texture and the four voltage measurements are extracted, the above condition causes the polarity of the hysteresis to reverse, and the ΔV_{ISHE} of the hysteresis to say the same in switching from a $+\hat{\mathbf{q}}$ measurement to a $-\hat{\mathbf{q}}$ measurement as depicted in the $\mathcal{T}$ row of Fig. 7.3.

Any symmetry operation $\mathcal{O}$ can be analyzed in this way to find implications in the magnetic texture on the V_{ISHE} measurements. This process is done for three mirror operations m_{xz}, m_{xy}, and m_{yz} (Fig. 7.3) over the xz, xy, and yz planes relative to the device geometry (see the unprimed coordinate system in Fig. 7.2c). We note that upon applying m_{yz}, the poling direction is flipped, so the magnetic texture $m_{yz}(\Psi^{\hat{\mathbf{e}}})$ must be compared to the oppo-

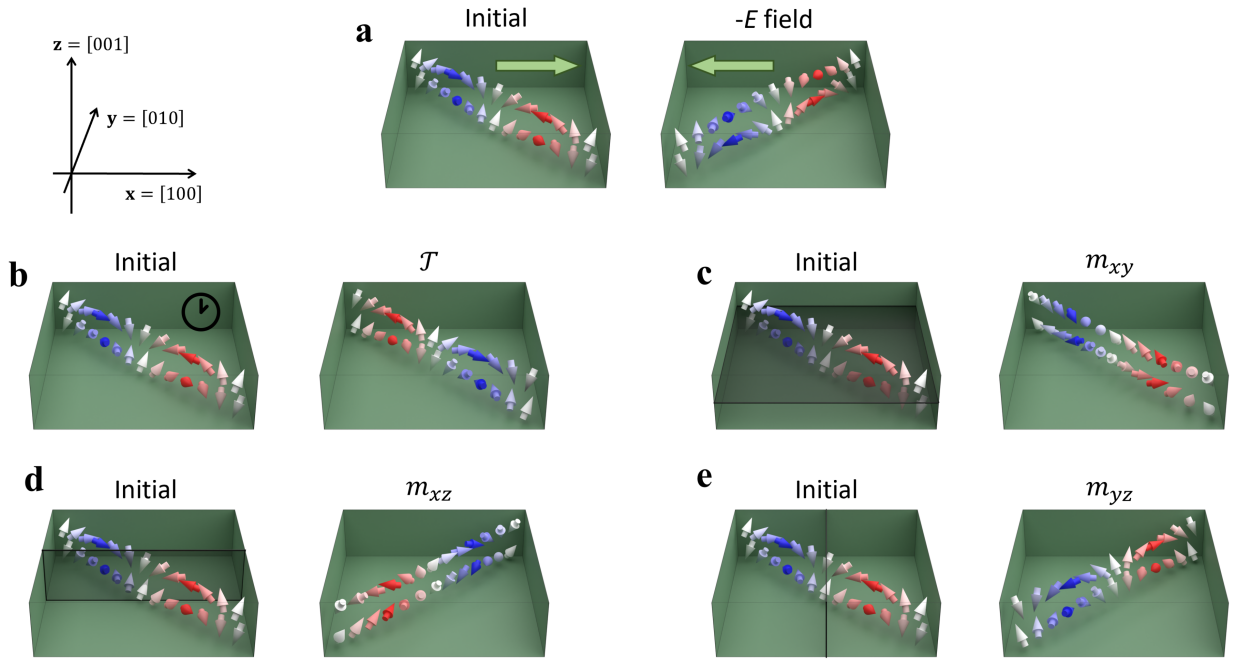

Figure 7.4: Symmetry operations on a spin cycloid. **a)** The cycloid is pictured here with initial denoting electric field poling in $+\hat{\mathbf{x}}$, to the right, adjacent to a cycloid under electric field poling in $-\hat{\mathbf{x}}$. The initial cycloid is repeated to aid the reader in comparing the states with and without the application of **b)** time reversal symmetry operation $\mathcal{T}$, as well as **c)** m_{xy}, **d)** m_{xz}, and **e)** m_{yz}. for the mirror symmetry operations, the mirror planes are drawn with the initial cycloid as an aid to the reader. We note that the arrows represent an average local magnetic moment, with spin-density-wave canting and spin cycloid rotation exaggerated for the viewer's sake. The location of the arrows transforms as a vector under the symmetry operations, and the direction of the arrows, which represents the magnetic moment, transforms as a pseudovector under the symmetry operations. The red shading denotes a local net moment in $+\hat{\mathbf{z}}$, and the blue shading denotes a local net moment in $-\hat{\mathbf{z}}$, from the spin-density wave.

sitely poled multiferroic texture $\Psi^{-\hat{\mathbf{e}}}$, as indicated by the table (Fig. 7.3). A visualization of the symmetry operations on the magnetic dipoles making up the BFO spin cycloid is included in Fig. 7.4, however we emphasize that these operations can be applied to any magnetic texture.

V_{ISHE} Experiments on BFO

To test this model, we choose a set of three samples with different magnetic textures. The magnetic textures of each sample was determined in a previous chapter, however for the reader's convenience we repeat the summary of the determination of $\Psi^{\hat{\mathbf{e}}}$ for each sample in Appendix F. Sample I is a 50-nm-thick BFO film grown on a $TbScO_3$ (110) substrate, with wires patterned parallel to the 109° ferroelectric strip domains. Samples II and III are 45-nm-thick BLFO films grown on $DyScO_3$ (110) substrates, with wires patterned parallel to $[100]_{pc}$ and $[010]_{pc}$ (pc: pseudocubic), respectively. All subsequent vectors are written in pseudocubic notation. Samples I and III have one variant of spin cycloid within the poled area, but sample II has two variants, with propagation vectors as noted (Fig. 7.5). The spin cycloid ground state of BFO is given by Fishman *et al.* [164], and our first observation is

that for all samples, $\mathcal{T}$, which flips each spin, is equivalent to a translation by half a period of the cycloid (Appendix. H). Since the magnetic texture is thus invariant under $\mathcal{T}$, we expect the V_{ISHE} data to exhibit the corresponding implications as shown (Fig. 7.3).

Measurements of V_{ISHE} for the three samples are provided (Fig. 7.5), and it can be seen that the polarity of the hysteresis is reversed while the magnitude of ΔV_{ISHE} remains the same upon switching $\hat{\mathbf{q}}$, as expected from the $\mathcal{T}$ invariance. While each sample has a 5-20 nV offset, we surmise that this could be from a gradient in the $\mathbf{z}$ direction and the resulting spin transport [159].

To analyze the mirror-symmetry operations, we take a closer look at the cycloidal texture in each domain. The precise determination of the polarization direction $\mathbf{z}'$ and the cycloid-propagation direction $\mathbf{x}'$ are discussed in Appendix F. The rotation of the Néel vector around the cycloid plane normal $\mathbf{y}'$ (Fig. 7.2c) changes under the mirror operations (Fig. 7.5 and Fig. 7.4). Since $\mathbf{y}'$ depends on the choice of $\mathbf{x}'$ (the cycloid propagation is an axis, and $\pm\mathbf{x}'$ are equivalent choices, however for self-consistent comparisons one formalism must be chosen and used exclusively), we define $\mathbf{\Omega_b}$ as the rotation of the Néel vector as measured along $\mathbf{b}$ (Fig. 7.2b):

$$\mathbf{\Omega_b} = (\mathbf{b}\cdot\mathbf{x}')\mathbf{y}'. \tag{7.5}$$

It is clear that this observable does not depend on the sign of $\mathbf{x}'$ chosen, since the sign of $\mathbf{x}'$ determines the sign of $\mathbf{y}'$. Figure 7.5 presents calculations for the three different BFO samples of $\mathbf{\Omega_b}$ with $\mathbf{b} = [100]$, $[010]$, and $[001]$, in the two different experimental configurations ($\hat{\mathbf{e}} = +\hat{\mathbf{x}}$, Identity, or $\hat{\mathbf{e}} = -\hat{\mathbf{x}}$, $\vec{E}$ poled) and under the three different mirror operations (acting on $\Psi^{\hat{\mathbf{e}}}$ for $\hat{\mathbf{e}} = +\hat{\mathbf{x}}$). Although only the directions are recorded here, the results hold if the magnitudes are included. The corresponding V_{ISHE}

a Sample I

Operation	$\mathbf{z}'$	$\mathbf{x}'$	$\mathbf{y}'$	$\mathbf{\Omega}_{[100]}$	$\mathbf{\Omega}_{[010]}$	$\mathbf{\Omega}_{[001]}$
Identity	$[111]$ $[1\bar{1}\bar{1}]$	$[01\bar{1}]$	$[011]$	0	$[011]$	$[0\bar{1}\bar{1}]$
m_{xz}	$[\bar{1}\bar{1}1]$ $[11\bar{1}]$	$[0\bar{1}\bar{1}]$	$[01\bar{1}]$	0	$[0\bar{1}1]$	$[0\bar{1}1]$
m_{xy}	$[11\bar{1}]$ $[\bar{1}\bar{1}1]$	$[011]$	$[0\bar{1}1]$	0	$[0\bar{1}1]$	$[0\bar{1}1]$
m_{yz}	$[\bar{1}11]$ $[\bar{1}\bar{1}\bar{1}]$	$[01\bar{1}]$	$[0\bar{1}\bar{1}]$	0	$[0\bar{1}\bar{1}]$	$[011]$
$\vec{E}$ poled	$[\bar{1}\bar{1}\bar{1}]$ $[\bar{1}11]$	$[011]$	$[01\bar{1}]$	0	$[0\bar{1}1]$	$[01\bar{1}]$

b Sample II

Operation	$\mathbf{z}'$	$\mathbf{x}'$	$\mathbf{y}'$	$\mathbf{\Omega}_{[100]}$	$\mathbf{\Omega}_{[010]}$	$\mathbf{\Omega}_{[001]}$
Identity	$[112]$ $[1\bar{1}2]$	$[1\bar{1}0]$ $[110]$	$[11\bar{1}]$ $[\bar{1}11]$	$[11\bar{1}]$ $[\bar{1}11]$	$[\bar{1}\bar{1}1]$ $[\bar{1}11]$	0 0
m_{xz}	$[1\bar{1}2]$ $[112]$	$[110]$ $[1\bar{1}0]$	$[\bar{1}11]$ $[11\bar{1}]$	$[\bar{1}11]$ $[11\bar{1}]$	$[\bar{1}11]$ $[\bar{1}\bar{1}1]$	0 0
m_{xy}	$[11\bar{2}]$ $[1\bar{1}2]$	$[1\bar{1}0]$ $[110]$	$[1\bar{1}\bar{1}]$ $[\bar{1}\bar{1}1]$	$[1\bar{1}\bar{1}]$ $[\bar{1}\bar{1}1]$	$[\bar{1}11]$ $[\bar{1}\bar{1}1]$	0 0
m_{yz}	$[\bar{1}12]$ $[\bar{1}\bar{1}2]$	$[\bar{1}\bar{1}0]$ $[110]$	$[\bar{1}\bar{1}1]$ $[\bar{1}\bar{1}\bar{1}]$	$[\bar{1}\bar{1}1]$ $[111]$	$[\bar{1}\bar{1}1]$ $[\bar{1}\bar{1}\bar{1}]$	0 0
$\vec{E}$ poled	$[\bar{1}\bar{1}2]$ $[\bar{1}\bar{1}\bar{2}]$	$[\bar{1}\bar{1}0]$ $[\bar{1}10]$	$[\bar{1}11]$ $[\bar{1}\bar{1}1]$	$[1\bar{1}\bar{1}]$ $[\bar{1}\bar{1}1]$	$[1\bar{1}\bar{1}]$ $[11\bar{1}]$	0 0

c Sample III

Operation	$\mathbf{z}'$	$\mathbf{x}'$	$\mathbf{y}'$	$\mathbf{\Omega}_{[100]}$	$\mathbf{\Omega}_{[010]}$	$\mathbf{\Omega}_{[001]}$
Identity	$[112]$	$[1\bar{1}0]$	$[11\bar{1}]$	$[11\bar{1}]$	$[\bar{1}\bar{1}1]$	0
m_{xz}	$[1\bar{1}2]$	$[110]$	$[\bar{1}11]$	$[\bar{1}11]$	$[\bar{1}11]$	0
m_{xy}	$[11\bar{2}]$	$[1\bar{1}0]$	$[\bar{1}\bar{1}\bar{1}]$	$[\bar{1}\bar{1}\bar{1}]$	$[111]$	0
m_{yz}	$[\bar{1}12]$	$[110]$	$[\bar{1}\bar{1}1]$	$[\bar{1}\bar{1}1]$	$[\bar{1}\bar{1}1]$	0
$\vec{E}$ poled	$[\bar{1}\bar{1}2]$	$[\bar{1}10]$	$[\bar{1}\bar{1}\bar{1}]$	$[\bar{1}\bar{1}1]$	$[\bar{1}\bar{1}1]$	0

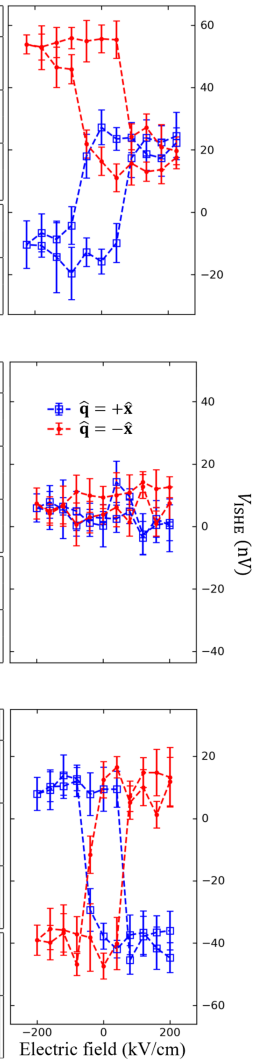

Figure 7.5: **Calculation of $\mathbf{\Omega_b}$.** The polarization directions $\mathbf{z}'$ and cycloid propagation directions $\mathbf{x}'$, as well as the effects of $\vec{E}$ poling, are taken from prior PFM, NV, and SHG work on these samples (Appendix F), and Eq. 7.5 is used to calculate $\mathbf{\Omega_b}$ for the three different samples. The V_{ISHE} hysteresis as a function of poling field for each sample is shown to the right for $\hat{\mathbf{q}} = \pm\hat{\mathbf{x}}$. All data is consistent with time reversal invariance. Sample II (III) shows m_{xz} (m_{yz}) invariance in all three $\mathbf{\Omega_b}$ (and therefore has invariance in $\mathbf{\Omega_b}$ for an $\mathbf{b}$, see Appendix G), as highlighted by the green boxes. The implications from these invariances as outlined by Fig. 7.3 are indeed reflected in the data.

data is included to the right for comparison. Sample I has ∼20-nm-wide stripy ferroelectric domains with polarization $\mathbf{z}'_1$ and $\mathbf{z}'_2$ at a 109° angle that lead to a a single variant spin cycloid with a propagation direction $\mathbf{x}'$ which is perpendicular to both $\mathbf{z}'_1$ and $\mathbf{z}'_2$ and a cycloid plane given by $\mathbf{y}' = \frac{1}{2}(\mathbf{z}'_1 + \mathbf{z}'_2) \times \mathbf{x}'$. We find that under the action of any mirror symmetry, $\mathbf{\Omega_b}$ changes, and so we expect no further than the $\mathcal{T}$ implications in the signal. The data reflect that symmetry, and show only the signatures of $\mathcal{T}$ invariance.

Sample II has two types of larger ferroelectric domains, each with their own spin cycloid as parameterized by the $\mathbf{z}'$, $\mathbf{x}'$, and $\mathbf{y}'$ in Fig. 7.5b. The m_{xz} operation effectively maps the cycloids, quantified by $\mathbf{\Omega_b}$, in each domain onto each other, leaving the global magnetic structure invariant up to a domain exchange. Since the population of both domains across the macroscopic area of the detector wire is the same, a domain exchange leaves the magnon signal invariant, so the sample is effectively invariant under m_{xz}. The implication, as given by Fig. 7.3, is that $V^{\hat{\mathbf{e}}}(\hat{\mathbf{q}}) = -V^{\hat{\mathbf{e}}}(\hat{\mathbf{q}}) = 0$, and aside from the small offset, the signal is uniformly zero as expected, despite a robust ferroelectric hysteresis (Fig. 7.1). This is an important result: the phenomenological model can be used to predict a lack of V_{ISHE} switching based on the symmetry of the magnetic texture, even without a microscopic understanding of the physics of magnon-spin transport.

Sample III has a single ferroelectric domain with one variant of spin cycloid. Notably for this sample, the effect of the m_{yz} operation on $\mathbf{\Omega_b}$ is identical to the effect of opposite field poling; $m_{yz}(\Psi^{\hat{\mathbf{e}}}) = \Psi^{-\hat{\mathbf{e}}}$. The implications, which is that the two hystereses lie on top of each other with no relative offset (Fig. 7.3), are indeed reflected in the data. The main difference between sample II and III is in the global magnetic texture, and our model identifies that the reduced symmetry of the magnetic texture in sample III allows for nonzero V_{ISHE}.

Conclusion

We note that in comparing predictions to experimental data, the model is limited by a) the ability of the spin-current absorbing contacts to average over the periodicity of the texture (as previously discussed) and b) any magnetic anomalies created by symmetry-breaking defects. Such defects will add signals that do not obey the implications of the symmetries broken. Despite this, the model still guides the overall understanding and predictions of the physical origin of magnon spin transport in these complicated magnetic textures. For example we apply these same ideas to predict the detection of magnons created by the spin-Hall effect in the source wire (Appendix I).

In conclusion, we have developed a phenomenological model for magnon-mediated spin transport in multiferroics, which summarizes the dynamics of a magnon mode μ with a phenomenological function η_μ of the experimental configuration. We have shown how this simple model, paired with an analysis of the magnetic texture based on symmetry operations, helps us to explain the behavior of magnon-mediated spin currents. We find that the model's predictions match well with the experimental data for second harmonic non-local magnon transport in BFO/Pt based systems. The approach can be extended generally to electric-field-controlled magnon propagation in all multiferroics, and will serve as an important tool for understanding spin currents in future magnon transport studies.

Part IV
Conclusions

While the road to multiferroic magnonic memory devices is challenging, and realizable applications are still far in the future, there is much to be learned from research towards this goal. Some of the main challenges include 1) finding materials with efficient spin-charge interconversion, 2) growing multiferroics with CMOS-compatibility, and 3) understanding magnon transport in multiferroics.

In addressing the first challenge in Chapter 3, we have introduced $BaPb_{1-x}Bi_xO_3$ (BPBO) to the spintronics community as a potential spin-charge interconversion material with a high efficiency. One exciting aspect of this material is that the efficiency is much higher than theoretically predicted for the intrinsic spin-Hall effect. This indicates that some exotic spintronic physics is present in this system, and by studying BPBO, we can uncover new avenues to efficiently convert between spin and charge currents. Furthermore, BPBO has also helped us address the second challenge in a surprising manner in Chapter 4: BPBO and $Ba_{1-x}La_xFeO_3$ (BLFO), materials which were not expected to be compatible due to high substrate mismatch, are in fact compatible at relatively low deposition temperatures, enabling potential CMOS compatibility. Studying the grapho-epitaxial nature of this pairing allows us to push the bounds of possible heterostructure combinations, and enables the combination of highly functional materials for studying new physics and potential applications.

In addressing the third challenge, we have made significant contributions to the understanding of magnons in $BiFeO_3$ and potentially other multiferroics. In the Chapters 5 and 6, we have characterized the anisotropy of magnon diffusion through several variants of spin cycloid configurations through changing the diffusion direction of the magnons as well as the ferroelectric polarization of the multiferroic. The combination of precise magnetic characterization through Nitrogen-vacancy magnetometry and careful measurements of magnon spin transport has allowed us to extensively map spin transport through the spin cycloid. The results from these chapters, enabled by our automated magnon-transport experimental setup, are combined in Chapter 7 to present a phenomenological model that uses symmetries inherent to the magnetic texture of the multiferroic to predict properties of the magnon transport. This model is generalizable to all multiferroics, and will be helpful in designing new experiments and applications using electric field control of magnon spin transport.

Future Experiments

New discoveries and advances will always lead to more questions and opportunities for advances, and this dissertation is no exception. The following important experiments will add to our understanding of physics pertaining to oxide spintronics and multiferroic magnonics.

While the demonstration of the efficient charge-to-spin conversion of BPBO is an important milestone, further experiments studying BPBO would uncover some of the physics behind the mechanisms of the charge-to-spin conversion. One such experiment is to vary the Bismuth doping of the BPBO films, and measure the spin-orbit torque (SOT) efficiency as a function of Bi doping as well as temperature. The crystal structure of BPBO as a function of Bi doping is already well understood [26], and comparing changes in the SOT

efficiency to changes in the structure and composition will illuminate the physics of the elusive mechanism for the strong spin-Hall effect. Furthermore, as the temperature changes, the resistivity changes and crosses a superconducting transition, and to measure the SOT efficiency across the superconducting transition would introduce exciting new physics of the interplay between superconductivity and spin-charge interconversion.

While all of the magnon spin-transport experiments done here are in a lateral geometry, we expect applications to use devices in a vertical geometry. The next step in demonstrating potential multiferroic magnonic memory is to create heterostructures with a multiferroic sandwiched between two spin-charge interconversion layers, and to create magnon transport devices with these heterostructures. While the fabrication of devices presents many challenges, the research here has identified materials that will make such devices possible. $SrIrO_3$ (SIO) has been identified as a spin-charge interconversion material that is compatible with $BiFeO_3$ [20], and in Chapter 4 we have identified that BPBO is also compatible with La-doped $BiFeO_3$.

While making devices with these materials is the first challenge, predicting their magnon signal is enabled by the phenomenological model presented in Chapter 7. A vertical device has different symmetries compared to a lateral device, and a symmetry operation analysis with the magnetic texture of the desired multiferroic will allow us to predict the resulting magnon signal, and determine if it will vanish (that is, the magnon signal may be unaffected by changing the ferroelectric polarization of the multiferroic) due to symmetries in the texture. An analysis similar to that done in Chapter 7 will determine the magnetic texture that must be used in such a device, and decisions with respect to electrode material and substrate strain will be made clearer upon such an analysis.

In conclusion, while this research has made important progress towards multiferroic magnonic memory using epitaxial oxide spintronics, there is more work to be done and more to be learned from the followup studies suggested above. We hope that the research summarized in this dissertation will serve as a road-map for future studies in the fields of oxide spintronics and multiferroic magnonics.

References

1. Sinova, J., Valenzuela, S. O., Wunderlich, J., Back, C. & Jungwirth, T. Spin hall effects. *Reviews of modern physics* **87,** 1213 (2015).
2. Adachi, H., Uchida, K.-i., Saitoh, E. & Maekawa, S. Theory of the spin Seebeck effect. *Reports on Progress in Physics* **76,** 036501 (2013).
3. Dieny, B. *et al.* Opportunities and challenges for spintronics in the microelectronics industry. *Nature Electronics* **3,** 446–459 (2020).
4. Liu, L. *et al.* Current-induced self-switching of perpendicular magnetization in CoPt single layer. *Nature Communications* **13,** 3539 (2022).
5. Park, S. R., Kim, C. H., Yu, J., Han, J. H. & Kim, C. Orbital-angular-momentum based origin of Rashba-type surface band splitting. *Physical review letters* **107,** 156803 (2011).
6. Chen, X. *et al.* Giant antidamping orbital torque originating from the orbital Rashba-Edelstein effect in ferromagnetic heterostructures. *Nature Communications* **9,** 2569 (2018).
7. Go, D. *et al.* Toward surface orbitronics: giant orbital magnetism from the orbital Rashba effect at the surface of sp-metals. *Scientific reports* **7,** 46742 (2017).
8. Heron, J., Schlom, D. & Ramesh, R. Electric field control of magnetism using BiFeO3-based heterostructures. *Applied Physics Reviews* **1** (2014).
9. Manipatruni, S. *et al.* Scalable energy-efficient magnetoelectric spin–orbit logic. *Nature* **565,** 35–42 (2019).
10. Cornelissen, L., Liu, J., Duine, R., Youssef, J. B. & Van Wees, B. Long-distance transport of magnon spin information in a magnetic insulator at room temperature. *Nature Physics* **11,** 1022–1026 (2015).
11. Xiao, J., Bauer, G. E., Uchida, K.-c., Saitoh, E., Maekawa, S., *et al.* Theory of magnon-driven spin Seebeck effect. *Physical Review B* **81,** 214418 (2010).
12. Rezende, S. M., Azevedo, A. & Rodríguez-Suárez, R. L. Magnon diffusion theory for the spin Seebeck effect in ferromagnetic and antiferromagnetic insulators. *Journal of Physics D: Applied Physics* **51,** 174004 (2018).
13. Rezende, S. M., Azevedo, A. & Rodríguez-Suárez, R. L. Introduction to antiferromagnetic magnons. *Journal of Applied Physics* **126** (2019).
14. Parsonnet, E. *et al.* Nonvolatile electric field control of thermal magnons in the absence of an applied magnetic field. *Physical review letters* **129,** 087601 (2022).
15. Huang, X. *et al.* Manipulating chiral spin transport with ferroelectric polarization. *Nature Materials,* 1–7 (2024).
16. Guo, G.-Y., Murakami, S., Chen, T.-W. & Nagaosa, N. Intrinsic spin Hall effect in platinum: First-principles calculations. *Physical review letters* **100,** 096401 (2008).
17. Guo, G. Ab initio calculation of intrinsic spin Hall conductivity of Pd and Au. *Journal of Applied Physics* **105** (2009).

18. Sui, X. *et al.* Giant enhancement of the intrinsic spin Hall conductivity in β-tungsten via substitutional doping. *Physical Review B* **96,** 241105 (2017).

19. Dc, M. *et al.* Room-temperature high spin–orbit torque due to quantum confinement in sputtered Bi x Se (1–x) films. *Nature materials* **17,** 800–807 (2018).

20. Huang, X. *et al.* Novel Spin–Orbit Torque Generation at Room Temperature in an All-Oxide Epitaxial La0. 7Sr0. 3MnO3/SrIrO3 System. *Advanced Materials* **33,** 2008269 (2021).

21. Sleight, A. W., Gillson, J. & Bierstedt, P. High-temperature superconductivity in the BaPb1-xBixO3 systems. *Solid State Communications* **17,** 27–28 (1975).

22. Cava, R. *et al.* Superconductivity near 30 K without copper: the Ba0. 6K0. 4BiO3 perovskite. *nature* **332,** 814–816 (1988).

23. Cox, D. & Sleight, A. Crystal structure of Ba2Bi3+ Bi5+ O6. *Solid State Communications* **19,** 969–973 (1976).

24. Uchida, S., Kitazawa, K. & Tanaka, S. Superconductivity and metal-semiconductor transition in BaPb1-xBixO3. *Phase Transitions* **8,** 95–128 (1987).

25. Yin, Z., Kutepov, A. & Kotliar, G. Correlation-Enhanced Electron-Phonon Coupling: Applications of G W and Screened Hybrid Functional to Bismuthates, Chloronitrides, and Other High-T c Superconductors. *Physical Review X* **3,** 021011 (2013).

26. Climent-Pascual, E., Ni, N., Jia, S., Huang, Q. & Cava, R. Polymorphism in BaPb 1-x Bi x O 3 at the superconducting composition. *Physical Review B* **83,** 174512 (2011).

27. Mattheiss, L. & Hamann, D. Electronic structure of Ba Pb 1- x Bi x O 3. *Physical Review B* **28,** 4227 (1983).

28. Foyevtsova, K., Khazraie, A., Elfimov, I. & Sawatzky, G. A. Hybridization effects and bond disproportionation in the bismuth perovskites. *Physical Review B* **91,** 121114 (2015).

29. Khazraie, A., Foyevtsova, K., Elfimov, I. & Sawatzky, G. A. Oxygen holes and hybridization in the bismuthates. *Physical Review B* **97,** 075103 (2018).

30. Li, G., Yan, B., Thomale, R. & Hanke, W. Topological nature and the multiple Dirac cones hidden in Bismuth high-Tc superconductors. *Scientific Reports* **5,** 10435 (2015).

31. Griffitt, S. *et al.* Local inversion-symmetry breaking in a bismuthate high-T c superconductor. *Nature communications* **14,** 845 (2023).

32. Zhang, X., Liu, Q., Luo, J.-W., Freeman, A. J. & Zunger, A. Hidden spin polarization in inversion-symmetric bulk crystals. *Nature Physics* **10,** 387–393 (2014).

33. Yuan, L. *et al.* Uncovering and tailoring hidden Rashba spin–orbit splitting in centrosymmetric crystals. *Nature communications* **10,** 906 (2019).

34. Giraldo-Gallo, P. *et al.* Field-tuned superconductor-insulator transition in BaPb 1- x Bi x O 3. *Physical Review B* **85,** 174503 (2012).

35. Parra, C. *et al.* Signatures of two-dimensional superconductivity emerging within a three-dimensional host superconductor. *Proceedings of the National Academy of Sciences* **118,** e2017810118 (2021).

36. Harris, D. T. *et al.* Superconductivity-localization interplay and fluctuation magnetoresistance in epitaxial BaPb 1- x Bi x O 3 thin films. *Physical Review Materials* **2,** 041801 (2018).

37. Bihlmayer, G., Noël, P., Vyalikh, D. V., Chulkov, E. V. & Manchon, A. Rashba-like physics in condensed matter. *Nature Reviews Physics* **4,** 642–659 (2022).

38. Sunko, V. *et al.* Maximal Rashba-like spin splitting via kinetic-energy-coupled inversion-symmetry breaking. *Nature* **549,** 492–496 (2017).

39. Mihai Miron, I. *et al.* Current-driven spin torque induced by the Rashba effect in a ferromagnetic metal layer. *Nature materials* **9,** 230–234 (2010).

40. Sánchez, J. R. *et al.* Spin-to-charge conversion using Rashba coupling at the interface between non-magnetic materials. *Nature communications* **4,** 2944 (2013).

41. Lesne, E. *et al.* Highly efficient and tunable spin-to-charge conversion through Rashba coupling at oxide interfaces. *Nature materials* **15,** 1261–1266 (2016).

42. Miron, I. M. *et al.* Perpendicular switching of a single ferromagnetic layer induced by in-plane current injection. *Nature* **476,** 189–193 (2011).

43. Fischer, M. H., Sigrist, M., Agterberg, D. F. & Yanase, Y. Superconductivity and local inversion-symmetry breaking. *Annual review of condensed matter physics* **14,** 153–172 (2023).

44. Kim, J. *et al.* Coherent-strained superconducting BaP b 1- x B i x O 3 thin films by interface engineering. *Physical Review Materials* **3,** 113606 (2019).

45. Liu, L., Moriyama, T., Ralph, D. & Buhrman, R. Spin-torque ferromagnetic resonance induced by the spin Hall effect. *Physical review letters* **106,** 036601 (2011).

46. Karimeddiny, S., Mittelstaedt, J. A., Buhrman, R. A. & Ralph, D. C. Transverse and longitudinal spin-torque ferromagnetic resonance for improved measurement of spin-orbit torque. *Physical Review Applied* **14,** 024024 (2020).

47. Edgeton, A. L. *et al.* Large spin–orbit torque in bismuthate-based heterostructures. *Nature Electronics* **6,** 973–980 (2023).

48. Giraldo-Gallo, P. *et al.* Stripe-like nanoscale structural phase separation in superconducting BaPb1- x Bi x O3. *Nature communications* **6,** 8231 (2015).

49. Liu, L. *et al.* Current-induced magnetization switching in all-oxide heterostructures. *Nature nanotechnology* **14,** 939–944 (2019).

50. Shi, S. *et al.* All-electric magnetization switching and Dzyaloshinskii–Moriya interaction in WTe2/ferromagnet heterostructures. *Nature nanotechnology* **14,** 945–949 (2019).

51. Kao, I.-H. *et al.* Deterministic switching of a perpendicularly polarized magnet using unconventional spin–orbit torques in WTe2. *Nature Materials* **21,** 1029–1034 (2022).

52. Zhu, L., Zhu, L., Sui, M., Ralph, D. C. & Buhrman, R. A. Variation of the giant intrinsic spin Hall conductivity of Pt with carrier lifetime. *Science Advances* **5,** eaav8025 (2019).

53. Liu, L. *et al.* Spin-torque switching with the giant spin Hall effect of tantalum. *Science* **336,** 555–558 (2012).

54. Ishizaka, K. *et al.* Giant Rashba-type spin splitting in bulk BiTeI. *Nature materials* **10,** 521–526 (2011).

55. Riley, J. M. *et al.* Direct observation of spin-polarized bulk bands in an inversion-symmetric semiconductor. *Nature Physics* **10,** 835–839 (2014).

56. Gotlieb, K. *et al.* Revealing hidden spin-momentum locking in a high-temperature cuprate superconductor. *Science* **362,** 1271–1275 (2018).

57. Wu, S.-L. *et al.* Direct evidence of hidden local spin polarization in a centrosymmetric superconductor LaO0. 55 F0. 45BiS2. *Nature communications* **8,** 1919 (2017).

58. Yao, W. *et al.* Direct observation of spin-layer locking by local Rashba effect in monolayer semiconducting PtSe2 film. *Nature communications* **8,** 14216 (2017).

59. Santos-Cottin, D. *et al.* Rashba coupling amplification by a staggered crystal field. *Nature communications* **7,** 11258 (2016).

60. Ciccarelli, C. *et al.* Room-temperature spin–orbit torque in NiMnSb. *Nature physics* **12,** 855–860 (2016).

61. Haney, P. M., Lee, H.-W., Lee, K.-J., Manchon, A. & Stiles, M. D. Current induced torques and interfacial spin-orbit coupling: Semiclassical modeling. *Physical Review B* **87,** 174411 (2013).

62. Shao, Q. *et al.* Strong Rashba-Edelstein effect-induced spin–orbit torques in monolayer transition metal dichalcogenide/ferromagnet bilayers. *Nano letters* **16,** 7514–7520 (2016).

63. Kim, M. *et al.* Superconductivity in (Ba, K) SbO3. *Nature materials* **21,** 627–633 (2022).

64. Emori, S. *et al.* Ultralow damping in nanometer-thick epitaxial spinel ferrite thin films. *Nano letters* **18,** 4273–4278 (2018).

65. Avci, C. O. *et al.* Current-induced switching in a magnetic insulator. *Nature materials* **16,** 309–314 (2017).

66. Martin, L. W. *et al.* Nanoscale control of exchange bias with BiFeO3 thin films. *Nano letters* **8,** 2050–2055 (2008).

67. Heron, J. *et al.* Electric-field-induced magnetization reversal in a ferromagnet-multiferroic heterostructure. *Physical review letters* **107,** 217202 (2011).

68. Cherifi, R. *et al.* Electric-field control of magnetic order above room temperature. *Nature materials* **13,** 345–351 (2014).

69. Parsonnet, E. *et al.* Toward intrinsic ferroelectric switching in multiferroic BiFeO 3. *Physical review letters* **125,** 067601 (2020).

70. Sando, D. *et al.* Control of ferroelectricity and magnetism in multi-ferroic BiFeO3 by epitaxial strain. *Philosophical Transactions of the Royal Society A: Mathematical, Physical and Engineering Sciences* **372,** 20120438 (2014).

71. Huang, Y.-L. *et al.* Manipulating magnetoelectric energy landscape in multiferroics. *Nature communications* **11,** 2836 (2020).

72. Wang, J. *et al.* Epitaxial BiFeO3 multiferroic thin film heterostructures. *science* **299,** 1719–1722 (2003).

73. Fiebig, M., Lottermoser, T., Meier, D. & Trassin, M. The evolution of multiferroics. *Nature Reviews Materials* **1,** 1–14 (2016).

74. Chu, Y.-H. *et al.* Nanoscale control of domain architectures in BiFeO3 thin films. *Nano letters* **9,** 1726–1730 (2009).

75. Huxter, W. S., Sarott, M. F., Trassin, M. & Degen, C. L. Imaging ferroelectric domains with a single-spin scanning quantum sensor. *Nature Physics* **19,** 644–648 (2023).

76. Sedky, S., Witvrouw, A., Bender, H. & Baert, K. Experimental determination of the maximum post-process annealing temperature for standard CMOS wafers. *IEEE transactions on Electron Devices* **48,** 377–385 (2001).

77. Zhou, X. *et al.* Epitaxial growth of SrTiO3 thin film on Si by laser molecular beam epitaxy. *Applied physics letters* **90** (2007).

78. Francois, T. *et al. Demonstration of BEOL-compatible ferroelectric Hf 0.5 Zr 0.5 O 2 scaled FeRAM co-integrated with 130nm CMOS for embedded NVM applications* in *2019 IEEE International Electron Devices Meeting (IEDM)* (2019), 15–7.

79. Yun, K. Y. *et al.* Structural and multiferroic properties of BiFeO 3 thin films at room temperature. *Journal of Applied Physics* **96,** 3399–3403 (2004).

80. Lee, Y.-H., Wu, J.-M., Chueh, Y.-L. & Chou, L.-J. Low-temperature growth and interface characterization of BiFeO3 thin films with reduced leakage current. *Applied Physics Letters* **87** (2005).

81. Yun, K. Y., Noda, M. & Okuyama, M. Prominent ferroelectricity of BiFeO 3 thin films prepared by pulsed-laser deposition. *Applied physics letters* **83,** 3981–3983 (2003).

82. *E. U. Restriction of Hazardous Substances Directives (RoHS): An Essential Guide* 2021. `https://compliancegate.com/rohs-directive/`.

83. Marx, D. *et al.* Metastable behavior of the superconducting phase in the BaBi 1- x Pb x O 3 system. *Physical Review B* **46,** 1144 (1992).

84. Bucci, J., Robertson, B. & James, W. The precision determination of the lattice parameters and the coefficients of thermal expansion of BiFeO3. *Journal of Applied Crystallography* **5,** 187–191 (1972).

85. Klyndyuk, A., Petrov, G. & Bashkirov, L. Anomalous high-temperature properties of BaPbO3-based solid solutions. *Inorganic materials* **37,** 399–404 (2001).

86. Liang, Y. *et al.* Hetero-epitaxy of perovskite oxides on GaAs (001) by molecular beam epitaxy. *Applied physics letters* **85,** 1217–1219 (2004).

87. Mozhaev, P. B. *et al.* Three-dimensional graphoepitaxial growth of oxide films by pulsed laser deposition. *Physical Review Materials* **2,** 103401 (2018).

88. Narayan, J. Recent progress in thin film epitaxy across the misfit scale (2011 Acta Gold Medal Paper). *Acta Materialia* **61,** 2703–2724 (2013).

89. Livey, D. & Murray, u. Surface energies of solid oxides and carbides. *Journal of the American Ceramic Society* **39,** 363–372 (1956).

90. Woo, S. *et al.* Surface-orientation-dependent growth of SrRuO3 epitaxial thin films. *Applied Surface Science* **499,** 143924 (2020).

91. Yadav, A. *et al.* Observation of polar vortices in oxide superlattices. *Nature* **530,** 198–201 (2016).

92. Chen, P. *et al.* Atomic imaging of mechanically induced topological transition of ferroelectric vortices. *Nature communications* **11,** 1840 (2020).

93. Sato, Y. *et al.* Lamellar-like nanostructure in a relaxor ferroelectrics Pb (Mg 1/3 Nb 2/3) O 3. *Journal of Materials Science* **56,** 1231–1241 (2021).

94. Zhang, Q., Zhang, L., Jin, C., Wang, Y. & Lin, F. CalAtom: A software for quantitatively analysing atomic columns in a transmission electron microscope image. *Ultramicroscopy* **202,** 114–120 (2019).

95. Li, F. *et al.* The origin of ultrahigh piezoelectricity in relaxor-ferroelectric solid solution crystals. *Nature communications* **7,** 13807 (2016).

96. Cowley, R., Gvasaliya, S., Lushnikov, S., Roessli, B. & Rotaru, G. Relaxing with relaxors: a review of relaxor ferroelectrics. *Advances in Physics* **60,** 229–327 (2011).

97. Wang, J. *et al.* On the importance of the work function and electron carrier density of oxide electrodes for the functional properties of ferroelectric capacitors. *physica status solidi (RRL)–Rapid Research Letters* **14,** 1900520 (2020).

98. Han, M.-G. *et al.* Interface-induced nonswitchable domains in ferroelectric thin films. *Nature communications* **5,** 4693 (2014).

99. Chumak, A., Serga, A. & Hillebrands, B. Magnonic crystals for data processing. *Journal of Physics D: Applied Physics* **50,** 244001 (2017).

100. Khitun, A., Bao, M. & Wang, K. L. Magnonic logic circuits. *Journal of Physics D: Applied Physics* **43,** 264005 (2010).

101. Kruglyak, V., Demokritov, S. & Grundler, D. Magnonics. *Journal of Physics D: Applied Physics* **43,** 264001 (2010).

102. Pirro, P., Vasyuchka, V. I., Serga, A. A. & Hillebrands, B. Advances in coherent magnonics. *Nature Reviews Materials* **6,** 1114–1135 (2021).

103. Jungwirth, T., Marti, X., Wadley, P. & Wunderlich, J. Antiferromagnetic spintronics. *Nature nanotechnology* **11,** 231–241 (2016).

104. Han, J., Cheng, R., Liu, L., Ohno, H. & Fukami, S. Coherent antiferromagnetic spintronics. *Nature Materials* **22,** 684–695 (2023).

105. Jungwirth, T. *et al.* The multiple directions of antiferromagnetic spintronics. *Nature Physics* **14,** 200–203 (2018).

106. Bibes, M. & Barthélémy, A. Towards a magnetoelectric memory. *Nature materials* **7,** 425–426 (2008).

107. Haykal, A. *et al.* Antiferromagnetic textures in BiFeO3 controlled by strain and electric field. *Nature communications* **11,** 1704 (2020).

108. Heron, J. *et al.* Deterministic switching of ferromagnetism at room temperature using an electric field. *Nature* **516,** 370–373 (2014).

109. Spaldin, N. A. & Ramesh, R. Advances in magnetoelectric multiferroics. *Nature materials* **18,** 203–212 (2019).

110. Rovillain, P. *et al.* Electric-field control of spin waves at room temperature in multiferroic BiFeO3. *Nature materials* **9,** 975–979 (2010).

111. Landau, L. D. & Lífshíts, E. M. *Electrodynamics of continuous media* (Pergamon Press Oxford, 1946).

112. Folen, V., Rado, G. & Stalder, E. Anisotropy of the magnetoelectric effect in Cr 2 O 3. *Physical Review Letters* **6,** 607 (1961).

113. Janesky, J. Impact of external magnetic fields on MRAM products. *Freescale Semiconductor Application Note AN3525 Rev. 0, Nov* (2007).

114. Chiba, D., Yamanouchi, M., Matsukura, F. & Ohno, H. Electrical manipulation of magnetization reversal in a ferromagnetic semiconductor. *Science* **301,** 943–945 (2003).

115. Ohno, H. *et al.* Electric-field control of ferromagnetism. *Nature* **408,** 944–946 (2000).

116. Matsukura, F., Tokura, Y. & Ohno, H. Control of magnetism by electric fields. *Nature nanotechnology* **10,** 209–220 (2015).

117. Arima, T.-h. Spin-driven ferroelectricity and magneto-electric effects in frustrated magnetic systems. *Journal of the Physical Society of Japan* **80,** 052001 (2011).

118. Fert, A., Ramesh, R., Garcia, V., Casanova, F. & Bibes, M. Electrical control of magnetism by electric field and current-induced torques. *Reviews of modern physics* **96,** 015005 (2024).

119. Yuan, W. *et al.* Electrical switching of the edge current chirality in quantum anomalous Hall insulators. *Nature Materials* **23,** 58–64 (2024).

120. Manipatruni, S., Nikonov, D. E. & Young, I. A. Beyond CMOS computing with spin and polarization. *Nature Physics* **14,** 338–343 (2018).

121. Chu, Y.-H. *et al.* Electric-field control of local ferromagnetism using a magnetoelectric multiferroic. *Nature materials* **7,** 478–482 (2008).

122. Liao, Y.-C. *et al.* Understanding the switching mechanisms of the antiferromagnet/ferromagnet heterojunction. *Nano Letters* **20,** 7919–7926 (2020).

123. Burns, S. R., Paull, O., Juraszek, J., Nagarajan, V. & Sando, D. The experimentalist's guide to the cycloid, or noncollinear antiferromagnetism in epitaxial BiFeO3. *Advanced Materials* **32,** 2003711 (2020).

124. Zhong, H. *et al.* Quantitative Imaging of Exotic Antiferromagnetic Spin Cycloids in Bi Fe O 3 Thin Films. *Physical Review Applied* **17,** 044051 (2022).

125. Sosnowska, I., Neumaier, T. P. & Steichele, E. Spiral magnetic ordering in bismuth ferrite. *Journal of Physics C: Solid State Physics* **15,** 4835 (1982).

126. Ramazanoglu, M. *et al.* Local weak ferromagnetism in single-crystalline ferroelectric BiFeO3. *Physical review letters* **107,** 207206 (2011).

127. Rahmedov, D., Wang, D., Íniguez, J. & Bellaiche, L. Magnetic cycloid of BiFeO 3 from atomistic simulations. *Physical review letters* **109,** 037207 (2012).

128. Lebeugle, D. *et al.* Electric-field-induced spin flop in BiFeO 3 single crystals at room temperature. *Physical review letters* **100,** 227602 (2008).

129. Gross, I. *et al.* Real-space imaging of non-collinear antiferromagnetic order with a single-spin magnetometer. *Nature* **549,** 252–256 (2017).

130. Sando, D. *et al.* Crafting the magnonic and spintronic response of BiFeO3 films by epitaxial strain. *Nature materials* **12,** 641–646 (2013).

131. Chu, Y.-H. *et al.* Nanoscale domain control in multiferroic BiFeO3 thin films. *Advanced Materials* **18,** 2307–2311 (2006).

132. Chu, Y.-H. *et al.* Domain control in multiferroic BiFeO3 through substrate vicinality. *Advanced Materials* **19,** 2662 (2007).

133. Meisenheimer, P. *et al.* Persistent anisotropy of the spin cycloid in BiFeO3 through ferroelectric switching. *arXiv preprint arXiv:2311.10169* (2023).

134. Wesenberg, D., Liu, T., Balzar, D., Wu, M. & Zink, B. L. Long-distance spin transport in a disordered magnetic insulator. *Nature Physics* **13,** 987–993 (2017).

135. Park, J.-G., Le, M. D., Jeong, J. & Lee, S. Structure and spin dynamics of multiferroic BiFeO3. *Journal of Physics: Condensed Matter* **26,** 433202 (2014).

136. Sosnowska, I. & Zvezdin, A. Origin of the long period magnetic ordering in BiFeO3. *Journal of magnetism and magnetic materials* **140,** 167–168 (1995).

137. Kadomtseva, A. *et al.* Phase transitions in multiferroic BiFeO3 crystals, thin-layers, and ceramics: enduring potential for a single phase, room-temperature magnetoelectric 'holy grail'. *Phase Transitions* **79,** 1019–1042 (2006).

138. Park, H. S. *et al.* Observation of the magnetic flux and three-dimensional structure of skyrmion lattices by electron holography. *Nature nanotechnology* **9,** 337–342 (2014).

139. Gitgeatpong, G. *et al.* Nonreciprocal magnons and symmetry-breaking in the noncentrosymmetric antiferromagnet. *Physical Review Letters* **119,** 047201 (2017).

140. Dos Santos, F. J., dos Santos Dias, M. & Lounis, S. Nonreciprocity of spin waves in noncollinear magnets due to the Dzyaloshinskii-Moriya interaction. *Physical Review B* **102,** 104401 (2020).

141. Kawano, M., Onose, Y. & Hotta, C. Designing Rashba–Dresselhaus effect in magnetic insulators. *Communications Physics* **2,** 27 (2019).

142. Kawano, M. & Hotta, C. Discovering momentum-dependent magnon spin texture in insulating antiferromagnets: Role of the Kitaev interaction. *Physical Review B* **100,** 174402 (2019).

143. Shiomi, Y. *et al.* Spin Seebeck effect in the polar antiferromagnet α- Cu 2 V 2 O 7. *Physical Review B* **96,** 180414 (2017).

144. Bhattacharjee, S., Rahmedov, D., Wang, D., Íniguez, J. & Bellaiche, L. Ultrafast switching of the electric polarization and magnetic chirality in BiFeO 3 by an electric field. *Physical Review Letters* **112,** 147601 (2014).

145. Ahmad, T., Jindal, K., Tomar, M. & Jha, P. K. Theoretical insight of origin of Rashba–Dresselhaus effect in tetragonal and rhombohedral phases of BiFeO 3. *Physical Chemistry Chemical Physics* **25,** 5857–5868 (2023).

146. Fedorova, N. S., Nikonov, D. E., Li, H., Young, I. A. & Íñiguez, J. First-principles Landau-like potential for BiFeO 3 and related materials. *Physical Review B* **106,** 165122 (2022).

147. Dong, S., Xiang, H. & Dagotto, E. Magnetoelectricity in multiferroics: a theoretical perspective. *National Science Review* **6,** 629–641 (2019).

148. Fedorova, N. S. *et al.* Understanding magnetoelectric switching in BiFeO 3 thin films. *Physical Review B* **109,** 085116 (2024).

149. Kan, D., Anbusathaiah, V. & Takeuchi, I. Chemical Substitution-Induced Ferroelectric Polarization Rotation in BiFeO3. *Advanced Materials* **23,** 1765 (2011).

150. Kan, D. *et al.* Universal behavior and electric-field-induced structural transition in rare-earth-substituted BiFeO3. *Advanced Functional Materials* **20,** 1108–1115 (2010).

151. Yadav, A. K. *et al.* Spatially resolved steady-state negative capacitance. *Nature* **565,** 468–471 (2019).

152. Prasad, B. *et al.* Ultralow voltage manipulation of ferromagnetism. *Advanced materials* **32,** 2001943 (2020).

153. Neaton, J., Ederer, C., Waghmare, U., Spaldin, N. & Rabe, K. First-principles study of spontaneous polarization in multiferroic Bi Fe O 3. *Physical Review B* **71,** 014113 (2005).

154. Albrecht, D. *et al.* Ferromagnetism in multiferroic BiFeO 3 films: a first-principles-based study. *Physical Review B* **81,** 140401 (2010).

155. Meisenheimer, P. *et al.* Switching the spin cycloid in BiFeO3 with an electric field. *Nature Communications* **15,** 2903 (2024).

156. Balke, N. *et al.* Deterministic control of ferroelastic switching in multiferroic materials. *Nature nanotechnology* **4,** 868–875 (2009).

157. Matzen, S. *et al.* Super switching and control of in-plane ferroelectric nanodomains in strained thin films. *Nature communications* **5,** 4415 (2014).

158. Cruz, M. *et al.* Strain control of domain-wall stability in epitaxial BiFeO 3 (110) films. *Physical review letters* **99,** 217601 (2007).

159. Shan, J. *et al.* Criteria for accurate determination of the magnon relaxation length from the nonlocal spin Seebeck effect. *Physical Review B* **96,** 184427 (2017).

160. Chen, W. & Sigrist, M. Dissipationless multiferroic magnonics. *Physical Review Letters* **114,** 157203 (2015).

161. Ross, A. *et al.* Exceptional sign changes of the nonlocal spin Seebeck effect in antiferromagnetic hematite. *Physical Review B* **103,** 224433 (2021).

162. Das, S. *et al.* Anisotropic long-range spin transport in canted antiferromagnetic orthoferrite YFeO3. *Nature Communications* **13,** 6140 (2022).

163. Here we assume that the spin carried by the magnon is independent of the wavevector k of the magnon, which is not always the case [165].

164. Fishman, R. S., Haraldsen, J. T., Furukawa, N. & Miyahara, S. Spin state and spectroscopic modes of multiferroic BiFeO 3. *Physical Review B* **87,** 134416 (2013).

165. Okuma, N. Magnon spin-momentum locking: Various spin vortices and Dirac magnons in noncollinear antiferromagnets. *Physical Review Letters* **119,** 107205 (2017).

166. Vanderbilt, D. Soft self-consistent pseudopotentials in a generalized eigenvalue formalism. *Physical review B* **41,** 7892 (1990).

167. Giannozzi, P. *et al.* QUANTUM ESPRESSO: a modular and open-source software project for quantum simulations of materials. *Journal of physics: Condensed matter* **21,** 395502 (2009).

168. Perdew, J. P., Burke, K. & Ernzerhof, M. Generalized gradient approximation made simple. *Physical review letters* **77,** 3865 (1996).

169. Murnaghan, F. D. The compressibility of media under extreme pressures. *Proceedings of the National Academy of Sciences* **30,** 244–247 (1944).

170. Franchini, C., Kresse, G. & Podloucky, R. Polaronic hole trapping in doped BaBiO 3. *Physical review letters* **102,** 256402 (2009).

171. Paier, J., Marsman, M. & Kresse, G. Why does the B3LYP hybrid functional fail for metals? *The Journal of chemical physics* **127** (2007).

172. Marsman, M., Paier, J., Stroppa, A. & Kresse, G. Hybrid functionals applied to extended systems. *Journal of Physics: Condensed Matter* **20,** 064201 (2008).

173. Nardelli, M. B. *et al.* PAOFLOW: A utility to construct and operate on ab initio Hamiltonians from the projections of electronic wavefunctions on atomic orbital bases, including characterization of topological materials. *Computational Materials Science* **143,** 462–472 (2018).

174. Agapito, L. A., Ferretti, A., Calzolari, A., Curtarolo, S. & Buongiorno Nardelli, M. Effective and accurate representation of extended Bloch states on finite Hilbert spaces. *Physical Review B—Condensed Matter and Materials Physics* **88,** 165127 (2013).

175. Agapito, L. A., Ismail-Beigi, S., Curtarolo, S., Fornari, M. & Nardelli, M. B. Accurate tight-binding Hamiltonian matrices from ab initio calculations: Minimal basis sets. *Physical Review B* **93,** 035104 (2016).

176. Boyd, R. W., Gaeta, A. L. & Giese, E. *Nonlinear optics* 1–67 (Springer, 2008).

177. Zhang, Y. *et al.* Ferroelectricity in a semiconducting all-inorganic halide perovskite. *Science advances* **8,** eabj5881 (2022).

Appendices

A Spin-Torque Ferromagnetic Resonance

ST-FMR devices with additional Hall contacts are used to separate spin-orbit torque signals from artifacts (Fig. 3.4a). It is well known that many artifacts can contribute to the symmetric signal in traditional, longitudinal ST-FMR such as spin pumping (SP) and the inverse spin Hall effect (ISHE), the anomalous Nernst effect (ANE), and the spin Seebeck effect (SSE). We use transverse Hall measurements as presented by ref. [46] to calculate the effects of these artifacts on our longitudinal ST-FMR signal. The applied radio-frequency current $I_{\mathrm{rf}}e^{-i\omega t}$ excites the unit magnetization $\hat{\mathbf{m}}$ of the BPBO into precession governed by the LLGS equation, shown below:

$$\frac{d\hat{\mathbf{m}}}{dt} = \gamma\hat{\mathbf{m}} \times \frac{dF}{d\hat{\mathbf{m}}} + \alpha\hat{\mathbf{m}} \times \frac{d\hat{\mathbf{m}}}{dt} + \boldsymbol{\tau}_{\mathrm{FL}} + \boldsymbol{\tau}_{\mathrm{DL}} + \boldsymbol{\tau}_{\mathrm{Oe}} \tag{A.1}$$

where γ and F are the gyromagnetic ratio and free energy which govern precession about the external field B, α is the Gilbert damping, and $\boldsymbol{\tau}_{\mathrm{FL,DL,Oe}}$ are the field-like, damping-like, and Oersted torques driving $\hat{\mathbf{m}}$ into precession. The resonant field which maximizes deflection of the magnetization is the field B_0 which solves the Kittel equation $\omega = \gamma\sqrt{B(B+\mu_0 M_{\mathrm{eff}}}$ where $\mu_0 M_{\mathrm{eff}} = \mu_0 M_S - 2K_\perp/M_S$ where μ_0 is the magnetization in-plane, M_S is the saturation magnetization, and $K_\perp$ is the anisotropy term which keeps the magnetization in-plane. In practice, M_{eff} is extracted by plotting the observed B_0 against the applied frequency ω as in Fig. 3.4c. Solving for the magnetization near the resonant field B_0 in the reference frame where the y-axis is parallel to the external field and the z-axis is normal to the sample surface, we can find the components of the precessing magnetization:

$$m_x(t) = m_x e^{-i\omega t} \quad \text{with} \quad m_x = \frac{-\omega_2\tau_z + i\omega\tau_x}{-(B-B_0)\gamma\omega^+ + i\omega\alpha\omega^+} \tag{A.2}$$

$$m_z(t) = m_z e^{-i\omega t} \quad \text{with} \quad m_z = \frac{\omega_1\tau_x + i\omega\tau_z}{-(B-B_0)\gamma\omega^+ + i\omega\alpha\omega^+} \tag{A.3}$$

where $\omega_2 = \gamma B + \mu_0 M_{\mathrm{eff}}$, $\omega_1 = \gamma B$, $\omega^+ = \omega_1 + \omega_2$, $\tau_x = (\boldsymbol{\tau}_{\mathrm{FL}} + \boldsymbol{\tau}_{\mathrm{DL}} + \boldsymbol{\tau}_{\mathrm{Oe}}) \cdot \hat{\mathbf{x}} = -\tau^0_{\mathrm{DL}}\cos\phi$, and similarly, $\tau_z = (\tau^0_{\mathrm{Oe}} - \tau^0_{\mathrm{FL}})\cos\phi$, and ϕ is the angle between the external magnetic field and the direction of current flow. The torques from the Oersted field and the spin-polarized current are opposite in sign assuming a positive SOT efficiency due to the growth order: LSMO is underneath the BPBO. The torques can be written in terms of the charge current density J_e in the BPBO and spin torque efficiencies ξ_{FL}, and $\xi_{\mathrm{DL}} = \theta_{\mathrm{SOT}}$:

$$\tau^0_{\mathrm{DL}} = \xi_{\mathrm{DL}}\frac{\mu_B J_e}{eM_s t_{\mathrm{FM}}}, \qquad \tau^0_{\mathrm{FL}} = \xi_{\mathrm{FL}}\frac{\mu_B J_e}{eM_s t_{\mathrm{FM}}}, \quad \text{and} \quad \tau^0_{\mathrm{Oe}} = \frac{\mu_0\gamma J_e t_{\mathrm{NM}}}{2} \tag{A.4}$$

where μ_B is the Bohr magneton, e is the elementary charge, and t_{FM} and t_{SOC} are the thicknesses of the ferromagnetic LSMO layer and non-magnetic BPBO layer respectively. The precessing magnetization and the anisotropic and spin Hall magnetoresistance effects (MR), anomalous Hall effect (AHE), and planar Hall effect (PHE), combined with the alternating

current, give us the following mixing voltages V_{XX}^{mix} and V_{XY}^{mix} which are measured from the bias tee and the hall contact pads respectively.

$$V_{XX}^{\text{mix}} = -R_{\text{MR}} \sin(2\phi) I_{\text{rf}} \tfrac{1}{2} \,\text{Re}[m_x] \tag{A.5}$$

$$V_{XY}^{\text{mix}} = R_{\text{PHE}} \cos(2\phi) I_{\text{rf}} \tfrac{1}{2} \,\text{Re}[m_x] - R_{\text{AHE}} I_{\text{rf}} \tfrac{1}{2} \,\text{Re}[m_z] \tag{A.6}$$

where $R_{\text{MR}} = R_{\text{AMR}} + R_{\text{SMR}}$, R_{PHE}, and R_{AHE} are the coefficients for anisotropic and spin Hall magnetoresistances, planar Hall effect, and anomalous Hall effect respectively. The real parts of the magnetization components contain the symmetric and antisymmetric Lorentzian shapes $S(B)$ and $A(B)$ around the resonant field B_0:

$$\text{Re}[m_x] = \frac{\cos\phi}{\omega^+ \alpha} \left[\tau_{\text{DL}}^0 S(B) + \left(\tau_{\text{FL}}^0 - \tau_{\text{Oe}}^0 \right) \frac{\omega_2}{\omega} A(B) \right] \tag{A.7}$$

$$\text{Re}[m_z] = \frac{\cos\phi}{\omega^+ \alpha} \left[\tau_{\text{DL}}^0 \frac{\omega_1}{\omega} A(B) - \left(\tau_{\text{FL}}^0 - \tau_{\text{Oe}}^0 \right) A(B) \right] \tag{A.8}$$

$$S(B) = \frac{\Delta^2}{(B-B_0)^2 + \Delta^2}, \quad A(B) = \frac{\Delta(B-B_0)}{(B-B_0)^2 + \Delta^2}, \quad \text{and} \quad \Delta = \alpha\omega/\gamma. \tag{A.9}$$

The linearity of $\Delta(\omega)$ can be seen in Fig. 3.4d. If we incorporate the effects of artifacts, we find that the effects of spin pumping and any thermal gradient will be proportional to the amplitude of the precession of the magnetization [46], and near the resonant field will take the form

$$\mathbf{E}_{\text{art}} = E_{\text{art}}^0 S(B) \cos^2\phi \, \hat{\mathbf{x}} \tag{A.10}$$

Through geometrical considerations of SP and ISHE, SSE and ISHE, and NE, it can be shown that the longitudinal voltages add the following terms to the longitudinal and transverse mixing voltages:

$$V_{XX}^{\text{mix/art}} = V_{XX}^{\text{mix}} + \sin(2\phi)\cos\phi S(B) E_{\text{art}}^0 \tfrac{L}{2} \tag{A.11}$$

$$V_{XY}^{\text{mix/art}} = V_{XY}^{\text{mix}} + (\cos(2\phi)\cos\phi + \cos\phi) S(B) E_{\text{art}}^0 \tfrac{W}{2} \tag{A.12}$$

where L and W are the length and width of the sample bar in the ST-FMR device. By separating the symmetric and antisymmetric Lorentzian fits at different field angles, we arrive at the following dependence on ϕ of the longitudinal symmetric and antisymmetric fit amplitudes from $V_{XY}^{\text{mix/art}} = V_S^{XY} + V_A^{XY}$:

$$V_S^{XX}(\phi) = S_{XX}^{\text{MR/art}} \sin(2\phi)\cos\phi, \qquad V_A^{XX}(\phi) = A_{XX}^{\text{MR}} \sin(2\phi)\cos\phi \tag{A.13}$$

$$V_S^{XY}(\phi) = S_{XY}^{\text{PHE/art}} \cos(2\phi)\cos\phi + S_{XY}^{\text{PHE/art}} \cos\phi \tag{A.14}$$

$$V_A^{XY}(\phi) = A_{XY}^{\text{PHE}} \cos(2\phi)\cos\phi + S_{XY}^{\text{AHE}} \cos\phi \tag{A.15}$$

The experimental measurements of $V_{XX}^{\text{mix/art}}$ and $V_{XY}^{\text{mix/art}}$ from longitudinal and transverse ST-FMR experiments, and curve-fitting of the traces, as shown in Fig. 3.4b, allow us to measure the 6 amplitudes above. These can depend on MR, PHE, AHE, and the artifact

field. We can then define the dimensionless ratio η:

$$\eta = \left(\tau_{\mathrm{DL}}^{0}\left(\tau_{\mathrm{FL}}^{0} - \tau_{\mathrm{Oe}}^{0}\right)\right)\sqrt{\omega_1/\omega_2} \tag{A.16}$$

And by realizing that η can be written in three different ways;

$$\eta = \frac{S_{XX}^{\mathrm{MR/art}} - E_{\mathrm{art}}^{0}\frac{L}{2}}{A_{XX}^{\mathrm{MR}}} = \frac{S_{XY}^{\mathrm{PHE/art}} - E_{\mathrm{art}}\frac{W}{2}}{A_{XY}^{\mathrm{PHE}}} = \frac{A_{XY}^{\mathrm{AHE}}}{S_{XY}^{\mathrm{AHE/art}} - E_{\mathrm{art}}^{0}\frac{W}{2}}\,, \tag{A.17}$$

we can use this redundancy to calculate the longitudinal artifact voltage in our samples $E_{\mathrm{art}}^{0}\frac{L}{2}$. With the transverse ST-FMR experiments performed, we find that $E_{\mathrm{art}}^{0}\frac{L}{2} \approx 0.3\,\mu\mathrm{V}$, whereas we find $S_{XX}^{\mathrm{MR/art}} \approx 6\,\mu\mathrm{V}$. Therefore we conclude that in experiments with no transverse ST-FMR, we can approximate $\eta = S_{XX}^{\mathrm{MR/art}}/A_{XX}^{\mathrm{MR}}$ and know that the systematic uncertainty from artifacts is only around 5%. Using the above equations, we see that η can be used to calculate the SOT efficiency:

$$\theta_{\mathrm{SOT}} = \eta\left(\xi_{\mathrm{FL}} - \frac{eM_S\mu_0\gamma t_{\mathrm{FM}}t_{\mathrm{NM}}}{2\mu_B}\right)\sqrt{1 + \frac{\mu_0 M_{\mathrm{eff}}}{B_0}} \tag{A.18}$$

Furthermore, by measuring η over a range of the product $t_{\mathrm{FM}}t_{\mathrm{NM}}$, and assuming that the spin-orbit torque efficiency is roughly constant in that range, we can calculate ξ_{FL} and find $\xi_{\mathrm{FL}} \approx 0.06 \pm 0.04$ as in Fig. 3.6a, leading us to conclude that the field-like torques generated by the spin-current are small in comparison to the damping-like torques, which we find to be $\theta_{\mathrm{SOT}} \approx 1.7 \pm 0.3$.

B First principles calculations

First-principles density functional theory calculations with fully relativistic ultrasoft pseudopotentials [166] were performed by Guatam Gurung and Evgeny Y. Tsymbal with QUantum ESPRESSO[167]. The exchange and correlation effects were treated with the generalized gradient approximation (GGA)[168]. The plane-wave cut-off energy of 52 Ry and a $16 \times 16 \times 16$ k-point mesh in the irreducible Brillouin zone were used in the calculations. The lattice parameter obtained by fitting Murnaghan equation of state is $a = 4.36$Å[169]. Spin-orbit coupling was included in all electronic structure calculations until mentioned otherwise. We note that using GGA, rather than a hybrid functional such as HSE is justified due to $BaPb_{1-x}Bi_xO_3$ being metallic for the range of Bi concentrations considered. While it is known that hybrid functionals, such as HSE, can correct the underestimated LDA or GGA band gaps of some insulators and semiconductors (in particular, the HSE correctly predicts the insulating nature of $BaBiO_3$),[25, 170] they have little effect on, or perform worse than, LDA or GGA for metallic systems (see, for example, ref. [171, 172]). We therefore use GGA in our calculations.

Tight-binding Hamiltonians are constructed using PAOFLOW[173] code based on the projection of the pseudoatomic orbitals (PAO)[174, 175] from the non-self-consistent calculations with a $16 \times 16 \times 16$ k-point mesh. The spin Hall conductivities were calculated using

the tight-binding Hamiltonians with a $48 \times 48 \times 48$ k-point mesh by the adaptive broadening method to get the converged values. The spin Hall conductivity is given by

$$\sigma_{ij}^{k} = \frac{e^2}{\hbar} \int \frac{d^3\mathbf{k}}{(2\pi)^3} \sum_n f_{n\mathbf{k}} \Omega_{n,ij}^{k}(\mathbf{k}) \tag{B.1}$$

$$\text{with} \qquad \Omega_{n,ij}^{k}(\mathbf{k}) = -2\,\mathrm{Im}\left[\sum_{n \neq n'} \frac{\langle n\mathbf{k}|\, J_i^k\, |n'\mathbf{k}\rangle \langle n'\mathbf{k}|\, v_j\, |n\mathbf{k}\rangle}{\left(E_{n\mathbf{k}} - E_{n'\mathbf{k}}\right)^2}\right] \tag{B.2}$$

where $f_{n\mathbf{k}}$ is the Fermi-Dirac distribution for the nth band, $J_i^k = \frac{1}{2}\{v_i, s_k\}$ is the spin current operator with spin operator s_k, $v_j = \frac{1}{\hbar}\frac{\partial H}{\partial k_j}$ is the velocity operator, and $i, j, k = x, y, z$. $\Omega_{n,ij}^{k}(\mathbf{k})$ is referred to as the spin Berry curvature in analogy to the ordinary Berry curvature.

We first consider the cubic structure for $BaPbO_3$ with lattice constant 4.36 Å. Fig. B.1a shows the orbital projected band structure for all the elements. We see that a pocket of

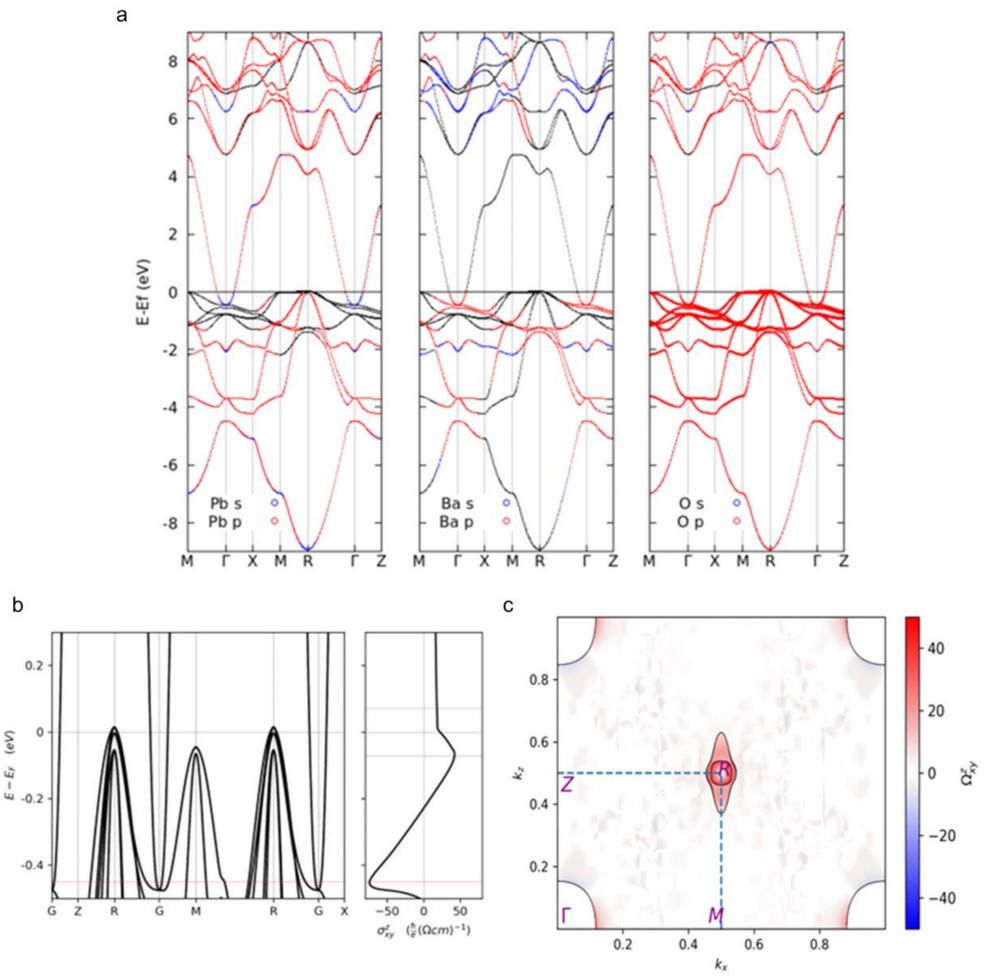

Figure B.1: **Results from first-principles calculations. a)** Orbital projected band structure of the cubic $BaPbO_3$ for Ba, Pb, and O. **b)** Variation of spin Hall conductivity σ_{xy}^z around the Fermi energy. **c)** Variation of spin Berry curvature at the Fermi energy in the [110] plane of the Brillouin zone.

unoccupied oxygen p bands appears at the R point of the Brillouin zone, which is consistent with the results of Li et al.[30] As a result, the oxygen p orbital has the largest contribution to the bands around the Fermi level. By symmetry, only conventional spin Hall conductivity (SHC) components (σ^z_{xy}) are finite in the cubic $BaPbO_3$. The calculated value is $\sigma^z_{xy} = 25\frac{\hbar}{e}(\Omega\text{cm})^{-1}$ at the Fermi energy. Fig B.1b shows the variation of the SHC near the Fermi level. The wide band above the Fermi level leads to slowly varying SHC. The major contribution at the Fermi energy comes from the R point as seen from the distribution of the spin Berry curvature Ω^z_{xy} in the [110] plane of the Brillouin zone (Fig. B.1c). This is due to the small splitting of the bands near the R point driven by spin-orbit coupling. Taking into account effects of possible octahedral rotations in the $BaPbO_3$ does not change the SHC significantly compared to the cubic phase. Finally, using the virtual crystal approximation for the substitutional doping of Pb by Bi, we find the variation of the SHC with respect to the energy level remains similar and the addition of Bi simply raises the Fermi energy, which is consistent with the results of Mattheiss et al.[27] and Li et al[30]. The calculated value is $\sigma^z_{xy} = 17\frac{\hbar}{e}(\Omega\text{cm})^{-1}$ at the Fermi energy for $BaPb_{0.75}Bi_0.27O_3$. In this case, the SHC is largely controlled by the free-electron bands around the Γ point, rather than the electronic states at the R point.

C Micromagnetic Simulations

Micromagnetic simulations were performed by Zhi Yao. We used MagneX, a GPU-enabled micromagnetic simulation code package, to phenomenologically explore the directionality of magnon transport in the spin cycloid. The time-domain Landau-Lifshitz-Gilbert equation is solved, incorporating exchange coupling, DMI coupling, anisotropy coupling, and demagnetization coupling. A set of abstract ferromagnetic properties is utilized to phenomenologically

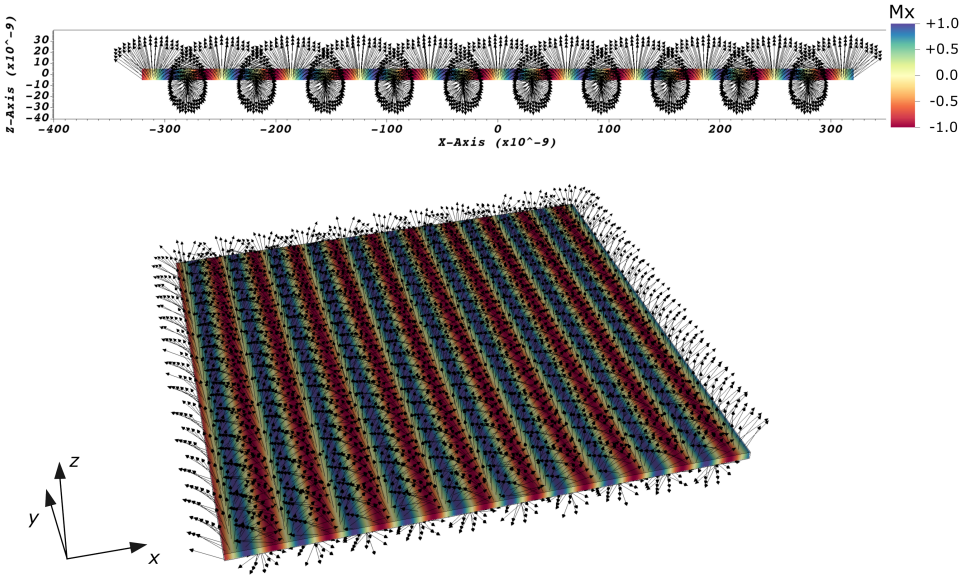

Figure C.1: **Initialized magnetization ground state.** The simulated initial cycloid, with a period of 62nm. Colored values show the magnitude of **M** projected along **x**. Black arrows show the local **M** vector.

represent the antiferromagnetic material. The magnetization is pinned by an external applied magnetic field that mimics the cycloid texture, as shown in Figure C.1.

The sample size is set to be $640 \times 640 \times 10$nm, with a $512 \times 512 \times 16$ mesh resulting in grid sizes of $\Delta x = \Delta y = 1.25$ nm, and $\Delta z = 0.625$ nm. The period of the cycloid used is 62nm. The Gilbert damping constant is set to be 0.0005, the exchange coupling constant is 3.0×10^{-12}J/m, and the DMI coupling constant is 1.0935×10^{-3} J/m^2. The anisotropic hard axis is set to the [111] direction, while the anisotropy constant is swept in the range of 1.0×10^4 to 2.0×10^6 J/m^3. The magnitude of the magnetization is normalized to be one.

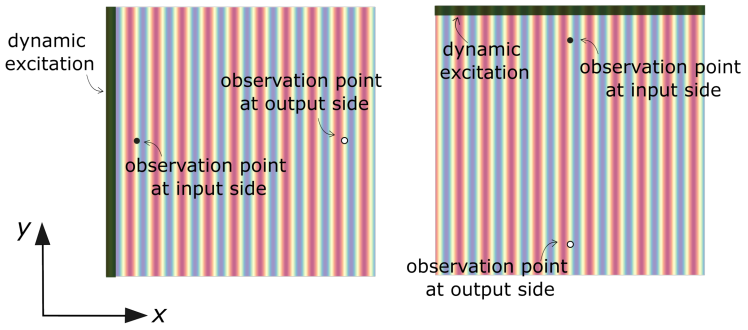

Figure C.2: **Modeling Setup.** The left figure illustrates the measurement of magnon transport along the cycloid direction ($\mathbf{q} \parallel \mathbf{k}$), while the right figure depicts magnon transport along the uniform direction of the cycloid ($\mathbf{q} \perp \mathbf{k}$).

Starting from $t = 0$, an additional time-dynamic external magnetic field is added on top of the existing pinning bias field. As shown in Figure C.2, on one side of the sample, a modified Gaussian pulse in the effective magnetic field is applied in both the x and y direction, mimicking injected spins from the top SOC electrode. The pulse has the form

$$B(t) \propto e^{-(t-t_0)^2/2T_0^2} \cos(2\pi f_0 t) \quad \text{where} \quad f_0 = 700 \text{ GHz}. \tag{C.1}$$

T_0 is chosen such that the excitation bandwidth is approximately 300 GHz. We create an input observation port near the location of the applied excitation, and an output port that is on the opposite side of the input port (Fig. C.2), and by measuring the magnetization components at the output and input ports, we can compute the spin wave transmission efficiency from the input to the output.

Figure C.4a,b shows the raw magnetization components at the input and output ports for both transport directions. The spots were selected where the ground-state magnetization is oriented in the out-of-plane direction, enabling a straightforward analysis of the magnon excitation. These simulated time-varying magnetization components are then converted into the frequency domain through the Fourier transform (fig. C.4). To calculate the solid angles of the oscillating magnetization, we express the spectral magnetization

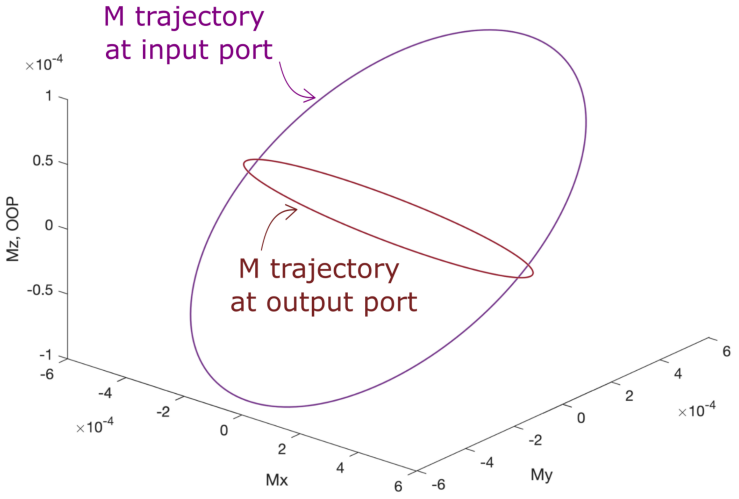

Figure C.3: **Magnetization trajectory at 700 GHz.** Input and output ports are along **x**, the **k** direction of the cycloid.

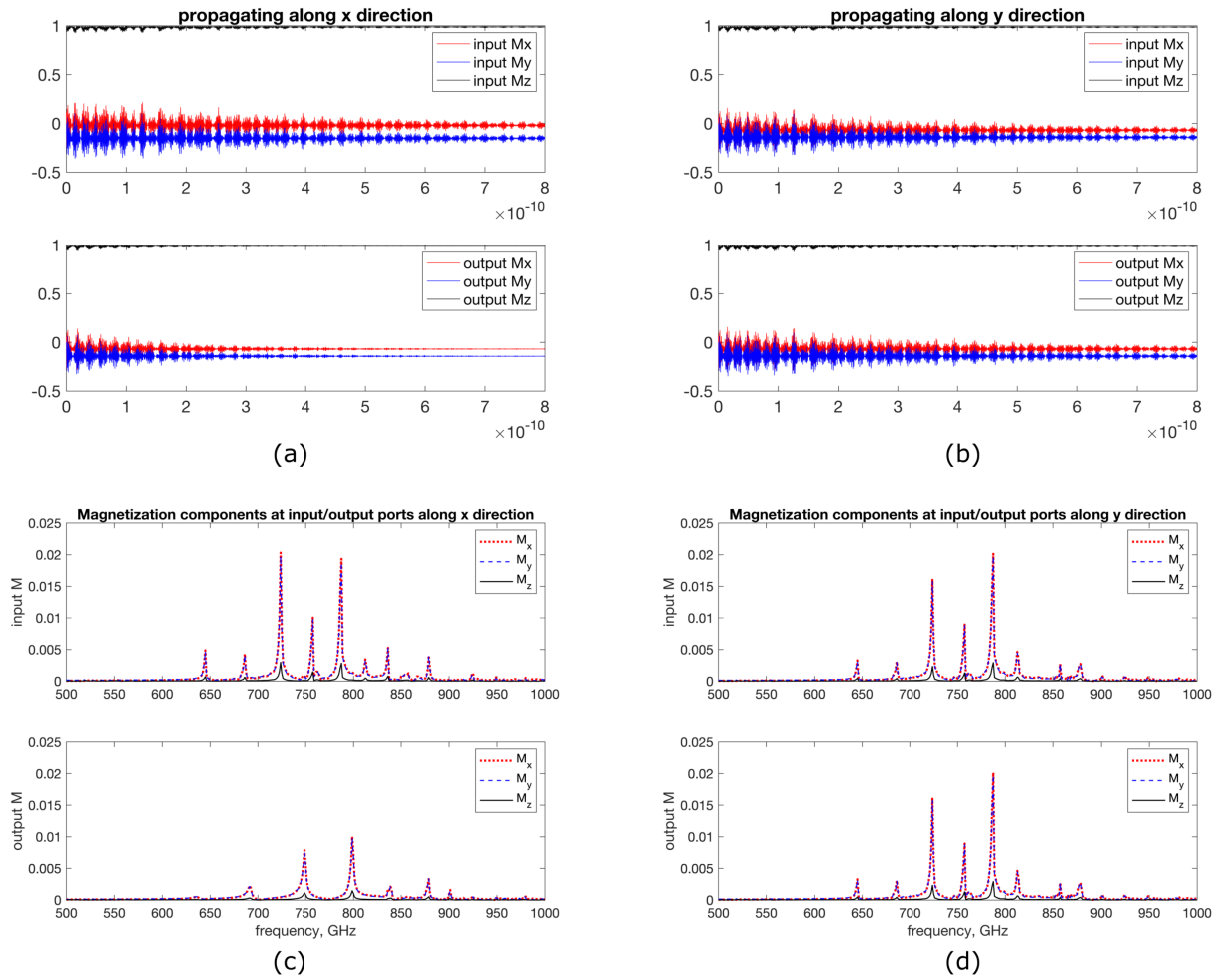

Figure C.4: **Time-domain and frequency-domain magnetization components at the input and output ports for both transport directions**.

components at each frequency point in the from

$$m = |M(f_0)| \cos(2\pi f_0 t + \angle M(f_0)). \tag{C.2}$$

This time-harmonic form provides an M trajectory at each frequency point, with a cone area corresponding to the solid angle of the M trajectory. For instance, Figure C.3 illustrates the magnetization trajectory at 700 GHz for input and output ports along the cycloid $\mathbf{k}$ direction. Considering the small solid angle of magnetization, we simplify the calculation of the 3D cone area to a planar cross-sectional area $S(f)$ by integrating over all sectors forming the trajectory. The cone angles at each frequency are then determined by $\Omega(f) = S(f)/|M(f=0)|^2$ as illustrated in Fig. C.5.

Subsequently, we calculate the magnon energy by integrating over its entire spectrum:

$$E = \sum_f \Omega(f) \times f. \tag{C.3}$$

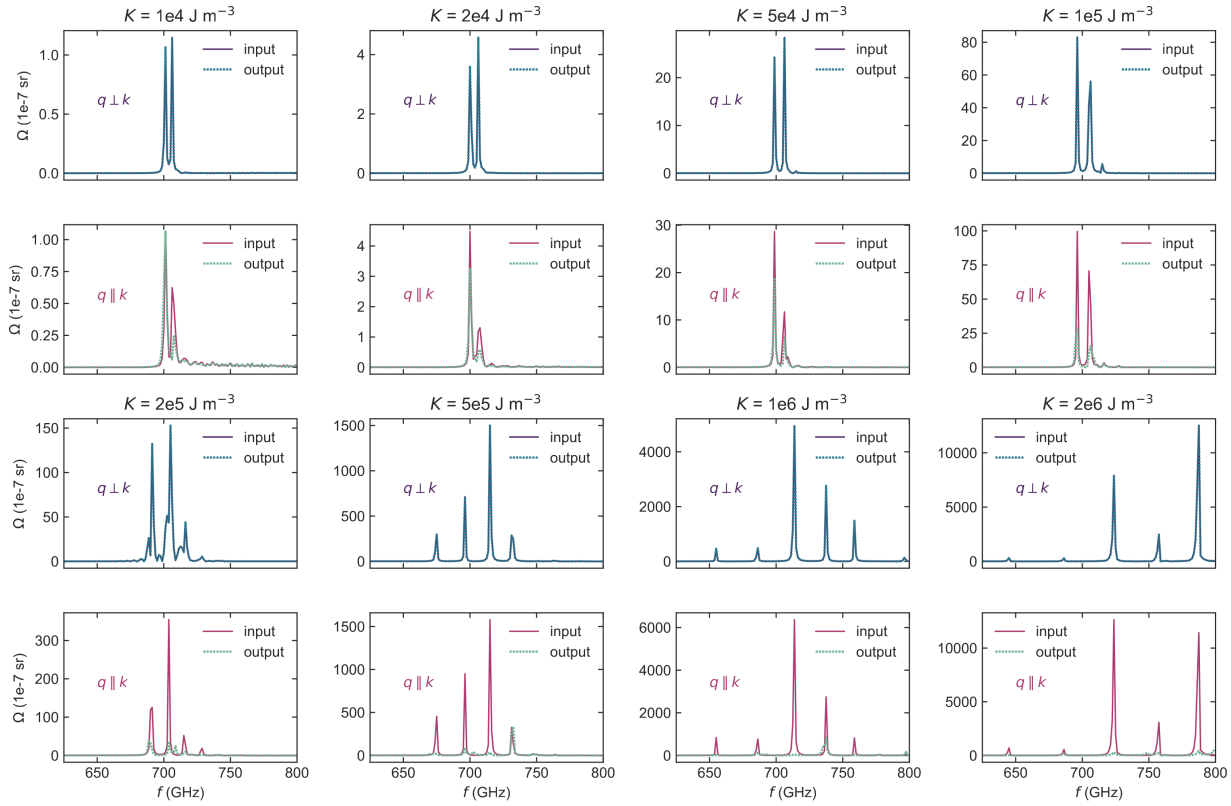

Figure C.5: **Spectral dependence of magnetocrystalline anisotropy.** Resonant spectra of excited spin waves extracted from phase field simulations in both the $\mathbf{q} \perp \mathbf{k}$ and $\mathbf{q} \parallel \mathbf{k}$ cases, used to calculate the efficiency scaling in Fig. 5.7c. Frequency dependent cone angles, Ω, are calculated as the Fourier transforms of the time dependent magnetization precession. Anisotropy (K) values are intentionally chosen both above and below the expected range.

Finally, the transport efficiencies for both along-x and along-y scenarios are determined by computing the power efficiency $E_{\text{output}}/E_{\text{input}}$, leading to the plot in Fig. 5.7c above.

D Analytical Solution for Magnon Bands in the Spin Cycloid

Our theory for $BiFeO_3$ is based on the following continuum Hamiltonian [135] and the corresponding Lagrangian, whose densities are given by

$$\mathcal{H} = \mathcal{A}(\nabla \mathbf{n})^2 - \alpha \mathbf{P} \cdot [\mathbf{n}(\nabla \mathbf{n}) + \mathbf{n} \times (\nabla \times \mathbf{n})] - 2\beta M_0 \mathbf{P} \cdot (\mathbf{m} \times \mathbf{n}) - K_u n_c^2 + \lambda \mathbf{m}^2 \quad \text{(D.1)}$$

$$\text{and} \qquad \mathcal{L} = s\mathbf{m} \cdot (\mathbf{n} \times \dot{\mathbf{n}}) - \mathcal{H}. \quad \text{(D.2)}$$

Here, the magnetic state is described by the Néel order parameter $\mathbf{n}(\mathbf{r}, t)$, whose length is unity, and the net magnetization $\mathbf{m}(\mathbf{r}, t)$, which is perpendicular to $\mathbf{n}(\mathbf{r}, t)$. The coefficients in the continuum Hamiltonian are related to the parameters in the microscopic spin

Hamiltonian as follows:

$$\lambda = \frac{6S^2}{V}(-3\mathcal{J} + 6\mathcal{J}') \tag{D.3}$$

$$\mathcal{A} = \frac{6S^2}{V} a_{hex}^2 \left(\frac{3\mathcal{J} - 4\mathcal{J}'}{4}\right) \tag{D.4}$$

$$\alpha = \frac{6S^2}{V}\frac{1}{P_s} a_{hex}^2 \mathcal{D}_u \tag{D.5}$$

$$\beta = \frac{6S^2}{V}\frac{1}{M_0 P_s}\mathcal{D}_c \tag{D.6}$$

$$\text{and} \qquad K_u = \frac{6S^2}{V}\mathcal{K} \tag{D.7}$$

where $\mathcal{J} = 4.38$ meV, $\mathcal{J}' = 0.15$ meV, $\mathcal{D}_u = 0.11$ meV, $\mathcal{D}_c = 0.05$ meV, $\mathcal{K} = 3$ μeV, $S = \sqrt{\frac{5}{2}(\frac{5}{2}+1)}$, $a_{hex} = 5.58 \times 10^{-8}$ cm, and $V = 375.9 \times 10^{-24}$ cm^3 [135]. The microscopic spin Hamiltonian can be found in Ref. [135]. It is convenient to use the spherical angles $\theta(\mathbf{r}, t)$ and $\phi(\mathbf{r}, t)$ to represent $\mathbf{n}$, and $m_\theta(\mathbf{r}, t)$ and $m_\phi(\mathbf{r}, t)$ to represent $\mathbf{m}$, where

$$\mathbf{n} = \sin\theta\cos\phi\hat{\mathbf{x}} + \sin\theta\sin\phi\hat{\mathbf{y}} + \cos\theta\hat{\mathbf{z}} \tag{D.8}$$

$$\mathbf{m} = (m_\theta\cos\theta\cos\phi - m_\phi\sin\phi)\hat{\mathbf{x}} + (m_\phi\cos\phi + m_\theta\cos\theta\sin\phi)\hat{\mathbf{y}} - m_\theta\sin\theta\hat{\mathbf{z}}. \tag{D.9}$$

In terms of these variables, the Euler-Lagrange equations of motion are given by the following:

$$\begin{aligned} -sm\partial_t\phi\,\cos\theta - s\partial_t m_\phi + 2A(\nabla^2\theta) + 2\alpha P_z\sin^2\theta\,(\sin\phi\,(\partial_x\phi) - \cos\phi\,(\partial_y\phi)) \\ - \sin 2\theta\,(A(\nabla\phi)^2 + K_u) - 2\beta M_0 P_z m_\phi\cos\theta = 0 \end{aligned} \tag{D.10}$$

$$s\partial_t(m_\theta\sin\theta) + 2A\nabla\cdot(\sin^2\theta\,(\nabla\phi)) - 2\alpha P_z\sin^2\theta\,(\sin\phi\,(\partial_x\theta) - \cos\phi\,(\partial_y\theta)) = 0 \tag{D.11}$$

$$-s\partial_t\sin\theta - \frac{m_\theta}{\chi} = 0 \tag{D.12}$$

$$s\partial_t\theta - \frac{m_\phi}{\chi} - 2\beta M_0 P_z\sin\theta = 0 \tag{D.13}$$

The ground state configuration $\mathbf{n}_0(\mathbf{r})$ and $\mathbf{m}_0(\mathbf{r})$ can be obtained by solving the Euler-Lagrange equations with no time dependence. The resulting ground state of $BiFeO_3$ has an anharmonic spin cycloid structure as well known [135–137]. Here, we focus on the cases where $\beta = 0$, as often done due to its smallness[135]. The explicit expression for a ground state is given by

$$\phi = \text{const.}, \qquad \theta = \text{am}\left(\sqrt{\frac{C}{A}}x, \frac{K_u}{C}\right) - \frac{\pi}{2} \tag{D.14}$$

with vanishing m, where $\text{am}(u, m)$ is the Jacobi amplitude function and C is the integral constant determined by minimizing the free energy of the aforementioned solution with respect to C [135]. Here, the spin-cycloid direction is chosen to be the x-axis without loss of generality.

By solving the time-dependent Euler-Lagrange equation for the small fluctuations, $\delta\mathbf{n} =$

$\mathbf{n}-\mathbf{n}_0$ and $\delta\mathbf{m} = \mathbf{m}-\mathbf{m}_0$, on top of the ground state up ot linear order in the fluctuations $\delta\mathbf{m}$ and $\delta\mathbf{n}$, we can obtain two spin-wave modes: an in-plane mode with spin fluctuations within the spin-cycloid plane and an out-of-plane mode whose spin fluctuations are perpendicular to the spin-cycloid plane. The corresponding equations of motion for $\delta\theta$, $\delta\phi$, δm_θ, and δm_ϕ are given by

$$-s\partial_t\delta m_\phi + 2A(\nabla^2\delta\theta) + 2\alpha P_z(\sin^2\theta_g)(\sin\phi_g\,(\partial_x\delta\phi) - \cos\phi_g\,(\partial_y\delta\phi)) - 2K_u\delta\theta\cos 2\theta_g = 0 \tag{D.15}$$

$$s\partial_t(\delta m_\theta\sin\theta_g) + 2A\nabla\cdot(\sin^2\theta_g(\nabla(\delta\phi))) - 2\alpha P_z\sin^2\theta_g\,(\sin\phi_g(\partial_x\delta\theta) + \delta\phi\cos\phi_g\,(\partial_x\theta_g) - \cos\phi_g\,(\partial_y\delta\theta) + \delta\phi\sin\phi_g\,(\partial_y\theta_g)) = 0 \tag{D.16}$$

$$-s\delta\dot{\phi}\sin\theta_g - \frac{\delta m_\theta}{\chi} = 0 \tag{D.17}$$

$$\delta\dot{\theta} - \frac{\delta m_\phi}{s\chi} = 0 \tag{D.18}$$

The translational symmetry along the z-axis allows us to use the plane-wave ansatz

$$\delta\theta(x,z,t) = \delta\theta(x;k_z,\omega)e^{ik_z z - i\omega t} \quad \text{and} \quad \delta\eta(x,z,t) = \delta\eta(x;k_z,\omega)e^{ik_z z - i\omega t} \tag{D.19}$$

with $\delta\eta = \sin\theta_g\,\delta\phi$. With these solutions, the above four equations can be combined into the following two equations for $\delta\theta(x;k_z,\omega)$ and $\delta\eta(x;k_z,\omega)$:

$$[(s^2\omega^2\chi - 2Ak_z^2) + 2A\partial_x^2 - 2K_u\cos 2\theta_g]\delta\theta = 0 \tag{D.20}$$

$$[(s^2\omega^2\chi - 2Ak_z^2) + 2A\partial_x^2 - 4K_u\cos^2(\theta_g) + 2C - 2\alpha P_z(\partial_x\theta_g)]\delta\eta = 0 \tag{D.21}$$

By solving these equations numerically, we obtained the band structures of in-plane magnons and out-of-plane magnons as shown in Figure 5.7d of the main text. It is apparent that the band structure for the two modes is anisotropic. We note that the anisotropy is the most visible in the lowest bands, which makes sense since low-energy magnons are expected to be more affected by the spin-cycloid structure than high-energy magnons and therefore exhibit anisotropic behavior more strongly.

E Optical Second Harmonic Generation (SHG) for in-plane Polarization Mapping

Optical second harmonic generation (SHG) was performed by Piush Behera to determine the response of BLFO polarization to an applied electric field. SHG involves the process of doubling the frequency of an incident light wave. The emission of SHG in a crystal is contingent upon its point group symmetry, making SHG responsive to any deviation from point symmetry in the material. As the development of ferroic order is closely associated with a reduction in crystal point-group symmetry, SHG serves as an effective means to investigate such ordered states in ferroelectric materials. The macroscopic description of the

source term for SHG is described through the polarizability tensor [176, 177]:

$$P_i^{2\omega} = \epsilon_0 \chi_{ijk} E_j^{\omega} E_k^{\omega} \tag{E.1}$$

where $\mathbf{E}^{\omega}$ is the incident electric field (laser light) at frequency ω, $\mathbf{P}^{2\omega}$ is the induced polarization in the nonlinear medium at frequency 2ω, which act as a source of an emitted, frequency-doubled, light wave with intensity $I_{SHG} \propto |P_i^{2\omega}|$. χ is the third-rank nonlinear susceptibility tensor, parameterizing the non-linear light-matter interaction. The form of the χ_{ijk} tensor is dictated by the specific crystal point group symmetry. The nonlinear polarization at 2ω radiates back electric field according to Maxwell's equation:

$$\nabla^2 \mathbf{E}^{2\omega} - \epsilon_0 \mu \frac{\partial^2 \mathbf{E}^{2\omega}}{\partial t^2} = \mu \frac{\partial^2 \mathbf{P}^{2\omega}}{\partial t^2} \tag{E.2}$$

with corresponding intensity

$$I^{2\omega} = \frac{1}{2} \epsilon_0 \nu (\mathbf{E}^{2\omega})^2. \tag{E.3}$$

Experimentally, one can access the specific χ_{ijk} components by carefully selecting incident linear light polarization, which we parameterize by azimuthal angle φ, where $\varphi = 0$ aligns with $[100]_{pc}$. Fig. E.1 illustrates a basic SHG setup being used in transmission mode, as it is in this work. A laser (wavelength 900nm) is used to excite the second harmonic response which is detected by the photodiode detector. The incident probe beam is linearly polarized by a Glan-Taylor prism. The polarization of the probe beam is then set to any angle by a rotatable half-wave plate. A low-pass filter is used to remove an second harmonic light generated in the polarization optics before the sample. The fundamental beam and higher-order harmonics are blocked by a band-pass filter before the photodiode. Since the second harmonic light is spectrally distinct from the probe light, monitoring the SHG frequency separately from the probe beam frequency simplifies the process, making it a relatively background-free characterization technique.

In the context of ferroelectrics, the breaking of inversion symmetry is facilitated by a polar distortion, resulting in non-zero χ_{ijk} components. To comprehensively char-

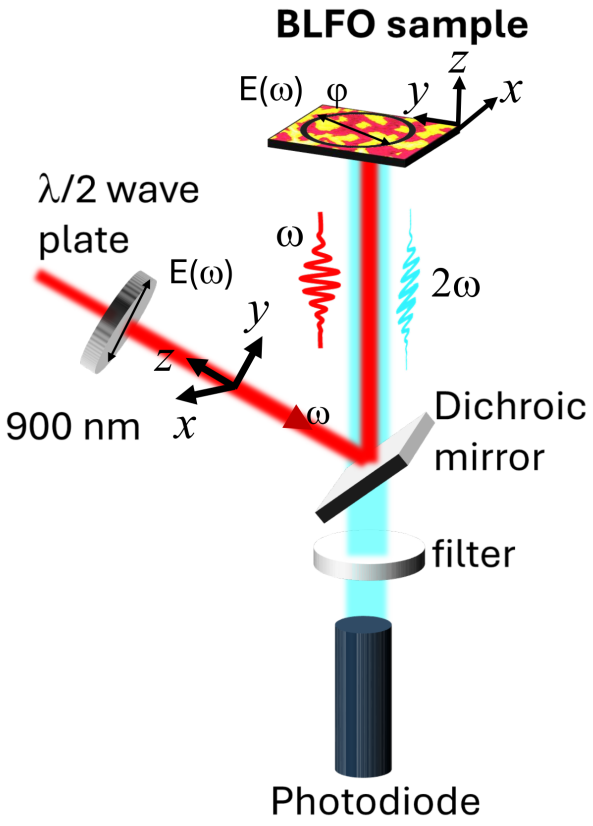

Figure E.1: **Typical optical second harmonic generation measurement setup**. Light at the fundamental frequency ω is absorbed and light at twice the fundamental frequency 2ω is emitted and detected.

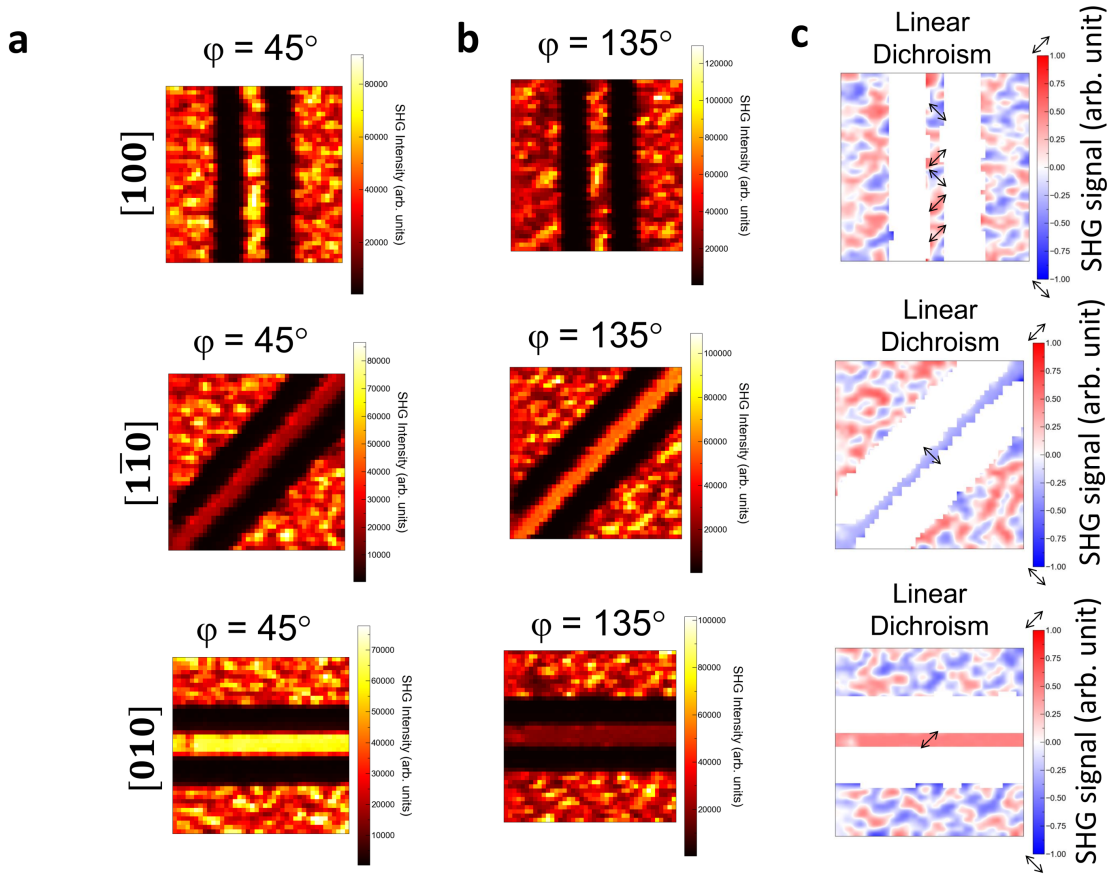

Figure E.2: **SHG dichroism**. Polarization maps recorded at **a)** $\varphi = 45°$ and **b)** $\varphi = 135°$ in three device orientations. **c)** The dichroic maps, labeled by color scales marked with direction of polarization, indicate the local ferroelectric polarization direction (modulo 180°) in a given location.

acterize this polar distortion along a specific crystallographic direction and distinguish between various tensor components, one can employ polarizer measurements. In these measurements, the polarizer angle φ is systematically rotated. For a uniformly-poled region, the SHG intensity achieves a maximum and minimum at specific φ values with a 90° difference, indicating parallel alignment of the in-plane ferroelectric polarization with the polarization of light in the maximum, and perpendicular alignment in the minimum. The dichroism from these two perpendicularly polarized measurements can give us the in-plane polarization direction as shown in Fig. E.2 (modulo 180°, but the direction of E-field poling removes any ambiguity there).

F Determining $\Psi^{\hat{e}}$ for multiferroic samples

The ferroelectric and magnetic states as a function of poling field were determined using piezoforce microscopy (PFM), optical second harmonic generation (SHG), and nitrogen-vacancy (NV) imaging. For sample I, which is 50nm of BFO on TSO (110) substrates, the PFM (shown in Fig F.1a,b) shows characteristic large superdomains with net polarization

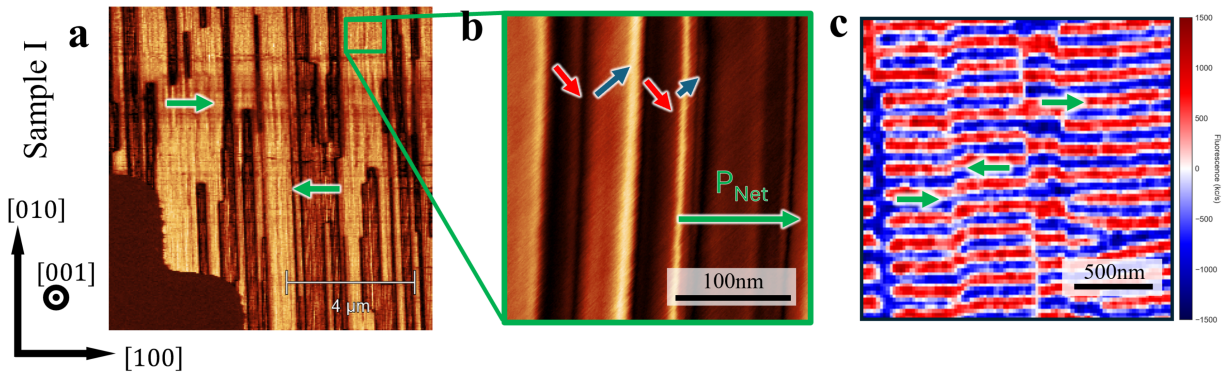

Figure F.1: **Ferroelectric and Magnetic state of sample I. a),b)** PFM and **c)** NV microscopy of sample I allows us to determine the spin cycloid propagation direction $\mathbf{x}'$ and the polarization direction $\mathbf{z}'$ in the magnetic state $\Psi^{\hat{\mathbf{e}}}$ for $\hat{\mathbf{e}} = \pm\hat{\mathbf{x}}$.

parallel to $\pm\hat{\mathbf{x}}$. However, a closer look at the superdomains shows very fine domains, the angle between polarization vectors in adjacent domains here is 109°. In the superdomain with net polarization along [100] ($[\bar{1}00]$), the ferroelectric polarization points along [111] or $[1\bar{1}\bar{1}]$ ($[\bar{1}1\bar{1}]$ or $[\bar{1}\bar{1}1]$), giving rise to a spin cycloid propagation direction along $[01\bar{1}]$ ($[0\bar{1}1]$) [155]. The boundary between these two spin cycloids appears in the NV-magnetometry (Fig. F.1c) as an antiphase boundary due to the opposite out of plane component of the spin cycloid propagation direction in the two superdomains. When an electric field is applied along $\pm\hat{\mathbf{x}}$,

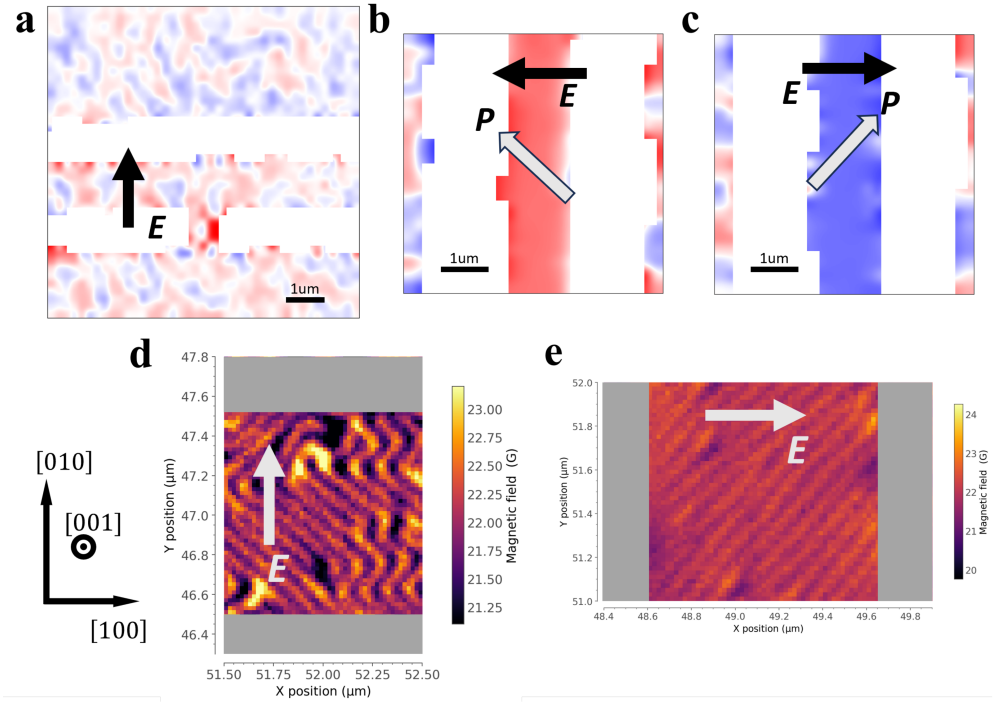

Figure F.2: **Ferroelectric and Magnetic state of samples II and III. a)-c)** SHG and **d)-e)** NV microscopy of samples II and III allows us to determine the spin cycloid propagation direction $\mathbf{x}'$ and the polarization direction $\mathbf{z}'$ in the magnetic state $\Psi^{\hat{\mathbf{e}}}$ for $\hat{\mathbf{e}} = \pm\hat{\mathbf{x}}$ in samples II and III.

the superdomain with antiparallel polarization to the applied field is annealed out.

For samples II and III, we use primarily SHG (see Appendix E) to determine the polarization directions (Fig. F.2a-c). The SHG map shows blue (red) when the in-plane component of polarization is along the [110] ($[\bar{1}10]$) axis. After poling via electric field, we can determine the exact in-plane direction of the polarization. No contrast in the out-of-plane PFM is observed in these samples (see previous chapter), and from prior BLFO studies [71], we know that the polarization is rotated along a [112] direction. The spin cycloid propagation is perpendicular to the polarization, and in the plane, along the axis [110] or $[\bar{1}10]$ depending on the polarization. In sample II (Fig. F.2a,d), both domains exist even when an electric field is applied, and the spin cycloid in each [112] ($[\bar{1}12]$) domain has a propagation axis along $[\bar{1}10]$ ([110]). In sample III, a single domain forms upon electric field poling, and similarly, a single cycloid domain exists (Fig. F.2b,c,e).

G Identity for $\mathbf{\Omega_b}$

Here we show that if $\mathbf{\Omega_b}$ is invariant under some operation $\mathcal{O}$ for 3 independent $\mathbf{b}$, then $\mathbf{\Omega_b}$ is invariant under $\mathcal{O}$ for any vector $\mathbf{b}$. Suppose for $i = 1, 2$, $\mathcal{O}(\mathbf{\Omega_{b_i}}) = \mathbf{\Omega_{b_i}}$. Recall,

$$\mathbf{\Omega_b} = (\mathbf{b} \cdot \mathbf{x}')\mathbf{y}' \tag{G.1}$$

For any constant a it follows that

$$\mathbf{\Omega_{b_1+ab_2}} = ((\mathbf{b}_1 + a\mathbf{b}_2) \cdot \mathbf{x}')\mathbf{y}' = (\mathbf{b}_1 \cdot \mathbf{x}')\mathbf{y}' + a(\mathbf{b}_2 \cdot \mathbf{x}')\mathbf{y}' = \mathbf{\Omega_{b_1}} + a\mathbf{\Omega_{b_2}} \tag{G.2}$$

Since symmetry operations are linear, it follows that

$$\mathcal{O}(\mathbf{\Omega_{b_1+ab_2}}) = \mathcal{O}(\mathbf{\Omega_{b_1}} + a\mathcal{O}(\mathbf{\Omega_{b_2}}) = \mathbf{\Omega_{b_1}} + a\mathbf{\Omega_{b_2}} = \mathbf{\Omega_{b_1+ab_2}} \tag{G.3}$$

Therefore, if $\mathbf{\Omega_b}$ is invariant under $\mathcal{O}$ for vectors $\mathbf{b}_i$, for any linear combination $\mathbf{b}'$ of the $\mathbf{b}_i$, $\mathbf{\Omega_{b'}}$ is invariant under $\mathcal{O}$. So, to show that $\mathbf{\Omega_b}$ is invariant under $\mathcal{O}$ for any vector $\mathbf{b}$, it suffices to show that $\mathbf{\Omega_{b_i}}$ is invariant under $\mathcal{O}$ for three independent basis vectors $\mathbf{b}_i$.

H The action of $\mathcal{T}$ on the spin cycloid

We consider the case of BFO under the time reversal operation $\mathcal{T}$. The magnetic Hamiltonian given by Fishman *et al.* [164] describes the energy of any given configuration of spin $\mathbf{S}_i$:

$$\begin{aligned} E = &- J_1 \sum_{\langle i,j \rangle} \mathbf{S}_i \cdot \mathbf{S}_j - J_2 \sum_{\langle i,j \rangle'} \mathbf{S}_i \cdot \mathbf{S}_j - K \sum_i S_{iz'}^2 \\ &- D_1 \sum_{\mathbf{R}_j = \mathbf{R}_i + a'\mathbf{x}'} \mathbf{y}' \cdot (\mathbf{S}_i \times \mathbf{S}_j) - D_2 \sum_{\mathbf{R}_j = \mathbf{R}_i + a\mathbf{x}, a\mathbf{y}, a\mathbf{z}} (-1)^{R_{iz'}/c} \mathbf{z}' \cdot (\mathbf{S}_i \times \mathbf{S}_j) \end{aligned} \tag{H.1}$$

Here, the exchange constants J_1 and J_2 and the pairs of spins $\langle i, j \rangle$ and $\langle i, j \rangle'$ are for nearest neighbor spins and second nearest neighbor spins respectively. K is the anisotropy constant.

The primed basis vectors $\mathbf{x}'$, $\mathbf{y}'$, and $\mathbf{z}'$ are rotate from the unprimed basis vectors so that $\mathbf{z}'$ lies along the direction of the polarization, $\mathbf{x}'$ lies along the propagation vector of the spin cycloid, and $\mathbf{y}' = \mathbf{z}' \times \mathbf{x}'$, as shown in Fig. 7.2c. The ground state of the magnetic Hamiltonian is the spin cycloid and spin-density wave with a period ~ 70 nm and no net magnetization [123, 126, 127, 164], and is also given by Fishman [164]:

$$S_{x'}(\mathbf{R}) = (-1)^{R_{z'}/c} \cos\tau \sqrt{S^2 - S_{z'}(\mathbf{R})^2} \times \mathrm{sgn}[\sin(kR_{x'})] \tag{H.2}$$

$$S_{y'}(\mathbf{R}) = \sin\tau \sqrt{S^2 - S_{z'}(\mathbf{R})^2} \times \mathrm{sgn}[\sin(kR_{x'})] \tag{H.3}$$

$$S_{z'}(\mathbf{R}) = (-1)^{R_{z'}/c} S \sum_{n=1,3\ldots}^{\infty} C_n \cos(nkR_{x'}) \tag{H.4}$$

where the odd-order coefficients C_n satisfy $\sum_{n=1,3\ldots}^{\infty} C_n = 1$ and give the anharmonicity of the cycloid, τ is a variational parameter, and $k\hat{\mathbf{x}}'$ is the spin cycloid propagation vector. The action of time reversal $\mathcal{T}$ on the spins $\mathbf{S}(\mathbf{R})$ is to negate each spin:

$$\mathcal{T}(\mathbf{S}(\mathbf{R})) = -\mathbf{S}(\mathbf{R}) \tag{H.5}$$

Consider the action of a translation by $\hat{\mathbf{x}}'\pi/k$. We show that $\mathbf{S}(\mathbf{R}') = -\mathbf{S}(\mathbf{R})$ where $\mathbf{R}' = \mathbf{R} + \hat{\mathbf{x}}'\pi/k$.

$$S_{z'}(\mathbf{R}') = (-1)^{R_{z'}/c} S \sum_{n=1,3\ldots}^{\infty} C_n \cos(nkR_{x'} + \pi) = -S_{z'}(\mathbf{R}) \tag{H.6}$$

$$S_{x'}(\mathbf{R}') = (-1)^{R_{z'}/c} \cos\tau \sqrt{S^2 - S_{z'}(\mathbf{R}')^2} \times \mathrm{sgn}[\sin(kR_{x'} + \pi)] = -S_{x'}(\mathbf{R}) \tag{H.7}$$

$$S_{y'}(\mathbf{R}') = \sin\tau \sqrt{S^2 - S_{z'}(\mathbf{R}')^2} \times \mathrm{sgn}[\sin(kR_{x'} + \pi)] = -S_{y'}(\mathbf{R}) \tag{H.8}$$

This shows that the action of time reversal $\mathcal{T}$ is equivalent to a translation. Thus, since the magnon dynamics as observed by the detector wire are effectively invariant by such a translation, the magnon dynamics are effectively invariant under $\mathcal{T}$.

We note that we are able to justify the effective translational invariance of the magnon dynamics as observed by the detector wire by appealing to the size of the detector wire. The detector wire has a width of 1.3μm and a length of 120μm, and has rough edges due to imperfections in the fabrication process. The macroscopic size of the detector contains many multiples of the spin cycloid, and the randomness of the edges averages out over the length of the wire to make a translation inconsequential in the magnon signal. This is also observed in the lack of significant variation in magnon signals from device to device, where the position of the detector wires with respect to the spin cycloid texture is not controlled for.

I Extension of the phenomenological model to magnon injection via the spin-Hall effect

When a spin current $\mathbf{I}_s^i$ (where the vector component denotes the spin polarization) is injected into the magnetic insulator, magnons in mode μ with spin $\langle \mathbf{S} \rangle_\mu$ are created with proportionality to $\mathbf{I}_s^i \cdot \langle \mathbf{S} \rangle_\mu$, and absorbed if the dot product is negative. This creates a concentration gradient in the magnon population across the device, and the resulting diffusion of magnons leads to a spin accumulation at the interface of the detector wire and the magnetic insulator. Let the wires be along $\hat{\mathbf{y}}$ and the film normal along $\hat{\mathbf{z}}$, so magnons diffuse along $\pm\hat{\mathbf{x}}$. To denote the location of the detector wire with respect to the source wire, we use $\hat{\mathbf{q}}' = \pm\hat{\mathbf{x}}$, identical to $\hat{\mathbf{q}}$ in the V_{SSE} studies. Furthermore, the injected spin current polarization is $\mathbf{I}_s^i = I_s^i \hat{\mathbf{x}}$. The resulting spin current into the detector wire $\mathbf{I}_s^d$ then has the form

$$\mathbf{I}_s^d \sim \sum_\mu I_s^i \langle S_x \rangle_\mu \langle \mathbf{S} \rangle_\mu \eta_\mu^{\hat{\mathbf{e}}}(\mathrm{sgn}[I_s^i \langle S_x \rangle_\mu] \hat{\mathbf{x}}). \tag{I.1}$$

Here we have the state of the multiferroic represented by $\hat{\mathbf{e}}$. There are two factors of the spin of the magnon $\langle \mathbf{S} \rangle_\mu$ because of the creation and absorption processes that happen at the source and detector. The voltage measured across the detector wire V_{SHE} is then proportional to $\mathbf{I}_s^d \cdot \hat{\mathbf{x}}$, and is measured referencing the first harmonic of a lock-in, which time averages

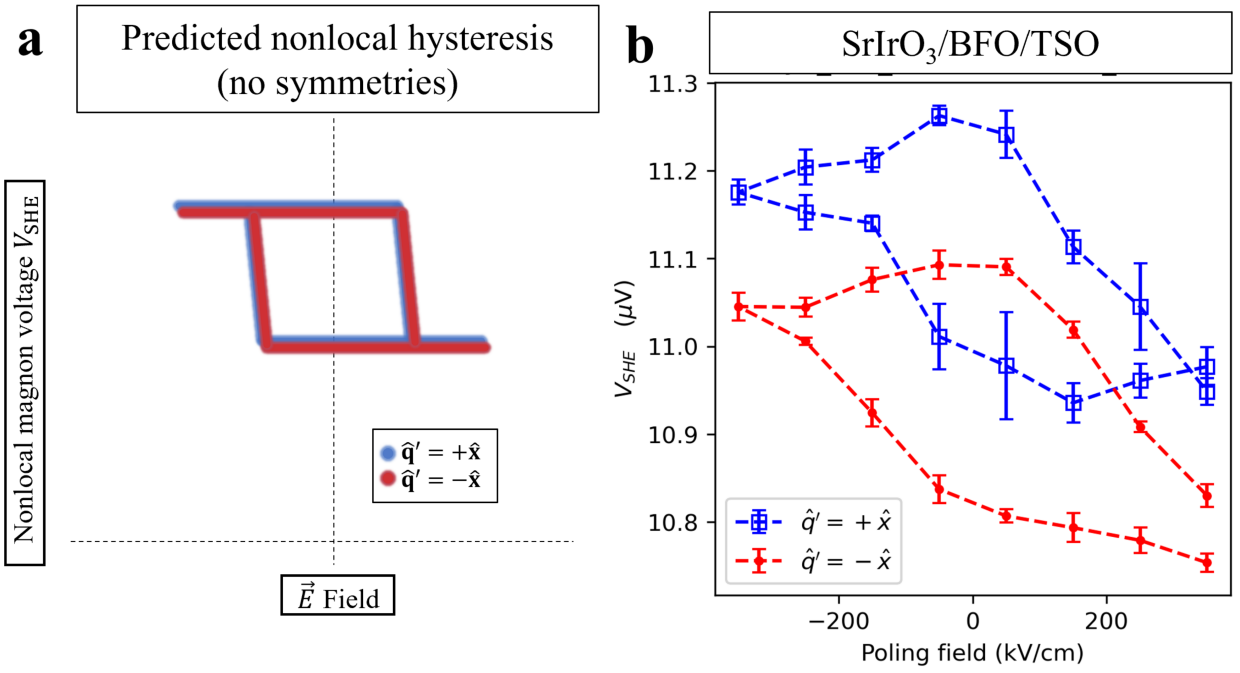

Figure I.1: **Spin-Hall effect magnon voltage. a)** Predicted hysteresis with no m_{yz}, m_{xz}, or m_{xy} symmetry constraints. $\mathcal{T}$ symmetry constraints are included. **b)** V_{SHE} hysteresis measured using $SrIrO_3$ source and detector on BFO with magnetic texture identical to sample I, with no symmetries besides effective $\mathcal{T}$ invariance. The distorted shape of the hysteresis is likely due to systematic issues in the quality of the $SrIrO_3$ electrodes such as resistive heating. The differing offsets are likely from systematic differences between the circuits for $\hat{\mathbf{q}}' = +\hat{\mathbf{x}}$ and $\hat{\mathbf{q}}' = -\hat{\mathbf{x}}$.

the product of the signal and the alternating source current. In such an alternating current, $I_s^i > 0$ for half the cycle, and $I_s^i < 0$ for the other half of the cycle, so the measured voltage is proportional to

$$V_{\text{SHE}} \sim \sum_\mu \langle S_x \rangle_\mu^2 \eta_\mu^{\hat{\mathbf{e}}}(+\hat{\mathbf{x}}) + \sum_\mu \langle S_x \rangle_\mu^2 \eta_\mu^{\hat{\mathbf{e}}}(-\hat{\mathbf{x}}). \tag{I.2}$$

Another way to think about this is to consider one magnon mode μ_1 with spin $\langle S_x \rangle_{\mu_1} = \hbar$. Magnons in this mode will be created and diffuse in $+\hat{\mathbf{x}}$ when $I_s^i > 0$, invoking $\eta_{\mu_1}^{\hat{\mathbf{e}}}(+\hat{\mathbf{x}})$. However, magnons in this mode will also be annihilated at the source and diffuse in $-\hat{\mathbf{x}}$ when $I_s^i < 0$, invoking $\eta_{\mu_1}^{\hat{\mathbf{e}}}(-\hat{\mathbf{x}})$. So, the signal V_{SHE} is a sum of both of those events.

We now suppose that we can choose the state between $\hat{\mathbf{e}} = \pm\hat{\mathbf{x}}$ by applying an electric field between the source and detector wires, and make a hysteresis measurement to measure $V_{\text{SHE}}^{+\hat{\mathbf{x}}} - V_{\text{SHE}}^{-\hat{\mathbf{x}}}$. The difference ΔV_{SHE} is then

$$\Delta V_{\text{SHE}} \sim \sum_\mu \left[\langle S_x \rangle_\mu^2 \eta_\mu^{+\hat{\mathbf{x}}}(+\hat{\mathbf{x}}) + \langle S_x \rangle_\mu^2 \eta_\mu^{+\hat{\mathbf{x}}}(-\hat{\mathbf{x}}) - \langle S_x \rangle_\mu^2 \eta_\mu^{-\hat{\mathbf{x}}}(+\hat{\mathbf{x}}) - \langle S_x \rangle_\mu^2 \eta_\mu^{-\hat{\mathbf{x}}}(-\hat{\mathbf{x}}) \right]. \tag{I.3}$$

Notice, that if we now switch the identity of the source and detector wire, changing $\hat{\mathbf{q}}'$ from $+\hat{\mathbf{x}}$ to $-\hat{\mathbf{x}}$ which effectively sends $\eta_\mu^{\hat{\mathbf{e}}}(\hat{\mathbf{q}}) \to \eta_\mu^{\hat{\mathbf{e}}}(-\hat{\mathbf{q}})$, the expression remains unchanged and we expect to recover a hysteresis with the same polarity and the same differential. We use $SrIrO_3$ electrodes to measure the first harmonic hysteresis, and our preliminary results reflect the model results (Fig. I.1).